Titre: Title:	Assessment of Flow Unsteadiness in Turbocharger Compressor
Auteur: Author:	Toni Chakour
Date:	2019
Type:	Mémoire ou thèse / Dissertation or Thesis
Référence: Citation:	Chakour, T. (2019). Assessment of Flow Unsteadiness in Turbocharger Compressor [Mémoire de maîtrise, Polytechnique Montréal]. PolyPublie. https://publications.polymtl.ca/4025/

URL de PolyPublie: PolyPublie URL:	https://publications.polymtl.ca/4025/
Directeurs de recherche: Advisors:	Huu Duc Vo
Programme: Program:	Génie mécanique

POLYTECHNIQUE MONTRÉAL

affiliée à l'Université de Montréal

Assessment of Flow Unsteadiness in Turbocharger Compressor

TONI CHAKOUR

Département de génie mécanique

Mémoire présenté en vue de l'obtention du diplôme de *Maîtrise ès sciences appliquées*

Génie mécanique

Août 2019

POLYTECHNIQUE MONTRÉAL

affiliée à l'Université de Montréal

Ce mémoire intitulé :

Assessment of Flow Unsteadiness in Turbocharger Compressor

présenté par **Toni CHAKOUR**

en vue de l'obtention du diplôme de *Maîtrise ès sciences appliquées*

a été dûment accepté par le jury d'examen constitué de :

Marcelo REGGIO, président

Huu Duc VO, membre et directeur de recherche

Étienne ROBERT, membre

DEDICATION

To my family

and especially to my father,

who introduced me to engineering at a young age

ACKNOWLEDGEMENTS

I would first like to thank Professor Huu Duc Vo for his continuous and unconditional support throughout the project completion over the last two years. His great availability and his numerous advices have helped me to complete this research project and overcome any difficulties during its completion.

I also wish to thank Dr. Bobby Sirakov and Mr. Zdenek Neterda, my contacts at Garrett Motion, with who I had the great pleasure of working during these two years. I thank them for the confidence they have shown in me. Despite their busy schedules, they were constantly available to me, whether to answer my questions or by holding regular meetings, sometimes even very early in their local time.

I would like to acknowledge the quality contribution of the mechanical engineering department technical team, brilliantly led by Mr. Alain Robidoux. He and his team helped me to solve several technical problems, even with very short notice. Without their involvement, I would never have been able to carry out so many numerical simulations.

It is important to note that the resources made available to us by Compute Canada and Compute Québec have also been very useful to me. I would therefore like to thank the helpers who have ensured the smooth running of the computational clusters over the past two years.

I was also fortunate to work with quality colleagues who were able to answer my questions if necessary: many thanks to Farzad Ashrafi, Javad Hosseini and Eddy Petro for their technical support. Also, thank you to Mahsa Ebrahimi and Lina Liu, colleagues with who I had the opportunity to go to the Global Power and Propulsion Society conference in Montréal. Special mention to my karateka friends with who I was able to unwind after the days of hard work.

Last but not least, I would like to thank my family for their moral support and patience during the last two years. My parents' commitment helped me to achieve my goals and to thrive while working in a field that I am passionate about.

RÉSUMÉ

Le turbocompresseur est un dispositif ajouté aux moteurs à combustion interne utilisé pour améliorer leur ratio poids-puissance. Il extrait l'énergie des gaz d'échappement du moteur pour pré-comprimer l'air d'admission grâce à un compresseur centrifuge et une volute. Une meilleure prédiction et compréhension des phénomènes aérodynamiques complexes associés avec la géométrie asymétrique du compresseur peut mener à la conception de turbocompresseurs plus efficaces.

Un test d'un rouet à aubes avec deux carters de compresseurs ayant des diffuseurs différents et des géométries de volutes variées, effectué dans des conditions à proximité du pompage (là où les instationnarités de l'écoulement sont attendues), a permis de trouver une différence significative en termes de rendement adiabatique du compresseur qui ne peut être décelé par des simulations préliminaires de dynamiques des fluides numérique (CFD) en régime permanent. L'objectif du présent projet est d'évaluer les capacités des simulations CFD instationnaires à détecter et à quantifier la différence en rendement adiabatique, puis d'identifier la nature et les sources des phénomènes instationnaires qui n'ont pas été saisies lors des précédentes simulations en régime permanent.

Les simulations CFD ont été effectuées en utilisant le logiciel ANSYS CFX pour les deux modèles de carters de compresseur, en régimes permanent et transitoire, à différents débits massiques pour lesquelles des données expérimentales sont disponibles. Différentes valeurs de pas de temps et de conditions limites ont aussi été appliquées aux simulations en régime transitoire. Bien que les simulations instationnaires détectent un comportement oscillatoire de l'écoulement et améliorent la prédiction de la valeur absolue du rendement adiabatique, elles n'ont pu permettre l'amélioration nette de la prédiction de l'écart d'efficacité remarqué entre les deux compresseurs telle que remarquée expérimentalement. Un petit pas de temps et une condition limite avec une sortie contrôlée par un papillon des gaz permettent une meilleure prédiction du rendement adiabatique et de la fréquence des oscillations.

Une analyse des champs d'écoulement indique que le décrochage rotatif dans le diffuseur est à l'origine même des oscillations perçues dans l'écoulement dans les simulations et le rendement adiabatique. Toutefois, son effet mène uniquement à une augmentation de l'amplitude

d’oscillation s’il peut induire un déversement intermittent dans la sortie de la volute à partir du diffuseur. Un modèle et un critère basés sur un seuil de vitesse radiale à la sortie du diffuseur sont proposés pour expliquer l’absence observée et contre-intuitive d’amplitude élevée dans le rendement dans un des cas simulés.

ABSTRACT

The turbocharger is a practical device for improving the power-to-weight ratio of piston engines. It extracts power from hot engine exhaust to pre-compress the intake air with a centrifugal compressor and volute. A better prediction and understanding of the complex aerodynamics associated with this asymmetric compressor can lead to turbochargers that are more efficient.

Rig test of an impeller with two compressor housings with different diffuser and volute geometry near surge (where flow unsteadiness is expected) found a significant difference in compressor adiabatic efficiency that cannot fully be captured by preliminary steady-state computational fluid dynamics (CFD) simulations (used for design). The objective of the current project is to evaluate the ability of unsteady CFD simulations to capture this measure difference in adiabatic efficiency and to identify the nature and source of the flow unsteadiness not captured by steady-state CFD simulations.

CFD simulations were carried out using ANSYS CFX for the full-annulus of the two compressors in both steady and unsteady modes at different mass flow values for which with the measured efficiencies are available. Different time step sizes and exit boundary conditions were also applied to the unsteady simulations. While the unsteady simulations capture significant flow oscillations and improve the prediction of the adiabatic efficiency, they did not provide a significant improvement in the prediction of the efficiency discrepancy between the two compressors. A small time step and a throttle exit boundary condition allow for better capture of efficiency and frequencies of oscillations.

An analysis of the unsteady flow field indicates that rotating stall in the diffuser is at the source of the flow oscillations seen in the adiabatic efficiency. However, its effect only leads high amplitude of oscillation in adiabatic efficiency if it can induce intermittent flow spillage from the diffuser exit directly into the volute exit. A model and criterion based on a threshold radial velocity at the diffuser exit is proposed that can explain the counter-intuitive absence of high-amplitude oscillation in efficiency seen in one of the simulated cases.

TABLE OF CONTENTS

LIST OF TABLES

LIST OF FIGURES

LIST OF SYMBOLS AND ABBREVIATIONS

A: Cross-sectional area

a: Speed of sound

B: Greitzer B parameter

cp: Heat capacity at constant pressure

f: Frequency

K_t: Throttle constant

L: Length

L_c: Compressor length

m: Mass flow

M: Mach number

N : Number of time steps per blade passing

P: Pressure

PR : Pressure ratio

RPM : Revolution per minute

S_c: Compressor annular area

Sr: Acoustic Strouhal number

T: Temperature

U: Mean circumferential rotor velocity

v: Velocity

V: Volume

CFD : Computational Fluid Dynamics

RANS: Reynolds Averaged Navier-Stokes

SST: Shear Stress Transport turbulence model

γ: Heat capacity ratio

η: Isentropic Efficiency

Ω, ω : Rotational speed

ρ: Density

Subscripts:

H: Helmholtz

m: Meridional

in: Inlet

out : Outlet

P: Plenum

T: Total

TT : Total-to-total

S: Static

0: Stagnation properties

1: Domain inlet

2: Inlet duct – impeller interface

3: Impeller – diffuser interface

4: Diffuser – volute interface

5 : Volute – Outlet duct interface

6 : Domain outlet

LIST OF APPENDICES

CHAPTER 1 INTRODUCTION

1.1 Background

Turbochargers are devices used to increase the power density (power-to-weight ratio) of internal combustion (piston) engines. They are used in cars, trucks and aircrafts, but also in heavy machinery like ships, submarines and trains. As illustrated in Figure 1.1, a turbocharger consists of a compressor and a turbine linked together via a shaft. The turbine extracts the thermal energy contained in the high-pressure hot exhaust gas of the engine to drive the compressor, which pre-compresses the ambient air fed into the engine.

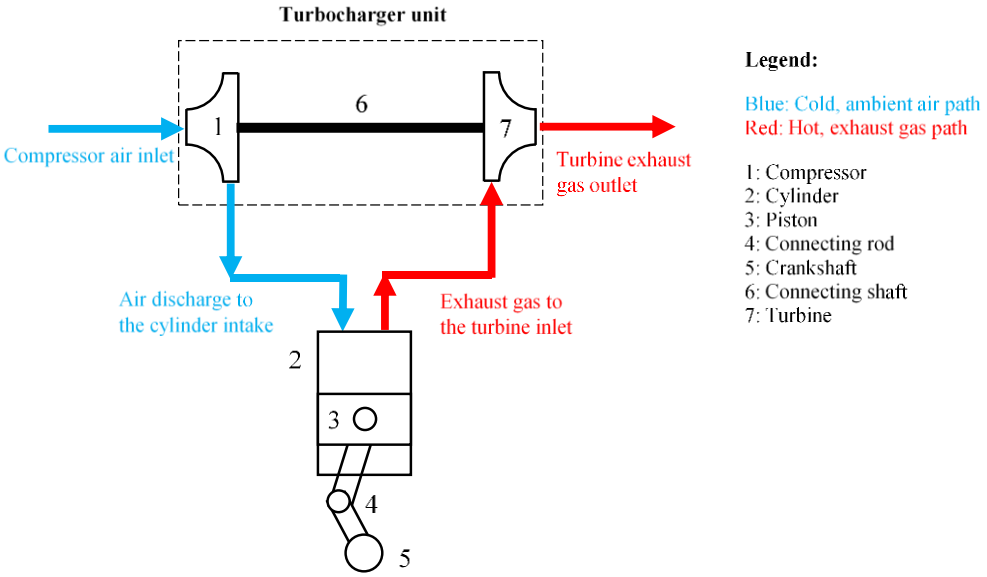

Figure 1.1 Schematic of a turbocharged engine

By compressing the air to the intake manifold, the air mass in the cylinder is increased and proportionally the fuel content, and by extension the power produced. As a result, turbocharged engines can be smaller and thus, lighter, while being able to produce the same output power, i.e. the power-to-weight ratio is higher. Moreover, the engine's efficiency can also be increased because of the energy extraction from the exhaust gases by the turbine, which would otherwise be completely lost to the atmosphere.

1.2 Turbocharger compressor

The compressor performance has a major effect of that of the turbocharger. Figure 1.2 shows a generic performance map for a compressor, which shows the variation of pressure ratio and adiabatic efficiency with *corrected mass flow* for different *corrected speed* (the mass flow and rotational speed are *corrected* to standard atmospheric pressure and temperature). The line corresponding to a particular corrected speed is called *speedline*. At a constant speed, a reduction in the mass flow typically causes an increase in pressure ratio, while the adiabatic efficiency increases up to a local maximum value and then decreases. The point of maximum efficiency usually corresponds to the design point of the compressor, which occurs at the design corrected speed and design corrected mass flow. The line running through this point as the compressor changes speed is the *running line*. The left extremity of each speedline marks the onset of *rotating stall*, which is an aerodynamic instability whereby the inlet flow axisymmetry breaks down into cells of flow non-uniformity rotating a fraction of the rotor/impeller speed. This point is often referred to as the *stall point*. In many cases, the stall point triggers a second instability called *surge*, which is an axisymmetric oscillation of the flow across the entire compressor. If this occurs, it is referred to as the *surge point*. The line linking the surge points from different speedlines on the compressor map is called the *surge line*. The further left is the surge line from the running line, the higher is the operability of the compressor.

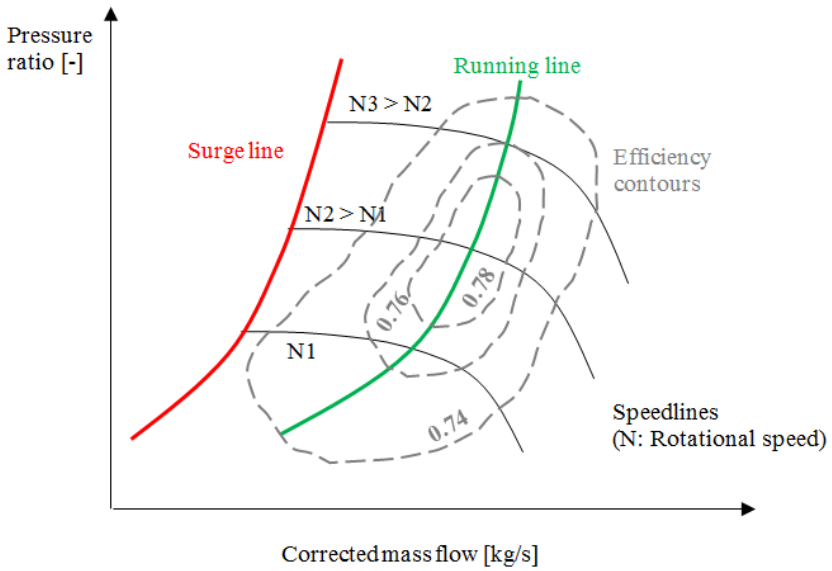

Figure 1.2 Generic compressor map

There are two main types of compressors, namely axial and radial (centrifugal) compressors, as illustrated in Figure 1.3. Each compression stage is composed of a rotating component followed by a stationary component, called *rotor* and *stator*, respectively, for an axial stage and *impeller* and *diffuser*, respectively, for a centrifugal stage. In an axial compressor, the flow through the compressor stays are a more or less constant radius, whereas the flow in a centrifugal compressor increases significantly in radius through the impeller. This results in a much higher pressure ratio per stage, but much more complicated flow with higher aerodynamic losses (lower adiabatic efficiency).

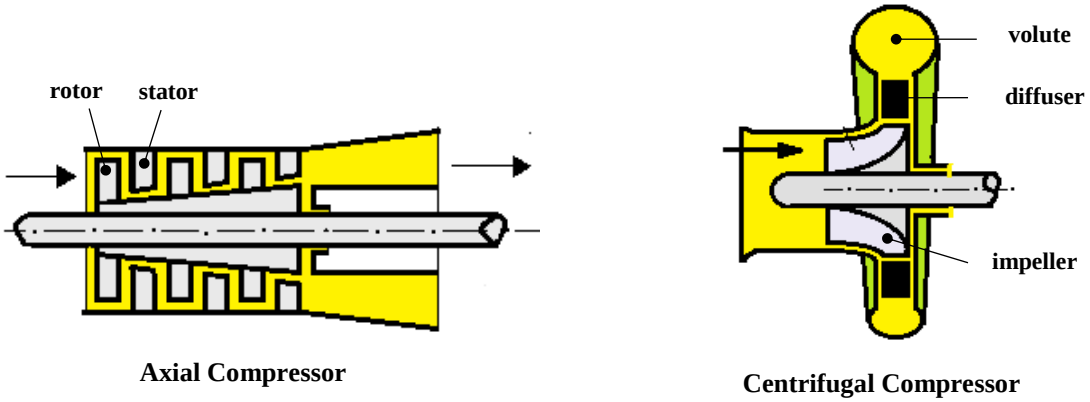

Figure 1.3 Type of compressors[1]

Axial compressors are more common in aircraft gas turbine engines due to their lower frontal area (less drag) and higher maximum adiabatic efficiency, which is taken full advantage of by this application as the aircraft engine spends most of its time at the design point (cruise condition).

On the other hand, turbochargers use almost exclusively radial compressors. The first reason is simplicity since the much larger stage pressure ratio allows for a single compressor stage. The second reason is that the operating requirement of a turbocharger is completely different than that of an aircraft gas turbine engine in that a car piston engine does not maintain a constant rotating speed such that the turbocharger compressor operation varies wildly in both speed and mass flow.

---

[1] Reference: https://upload.wikimedia.org/wikipedia/commons/a/a0/Axial-flow_compressor.png and https://upload.wikimedia.org/wikipedia/commons/a/a1/Centrifugal_compressor.png

As such, operability and adiabatic efficiency at different speeds are important, which is more inline with the characteristics of the centrifugal compressor. Indeed, centrifugal compressors can operate in rotating stall without surge (i.e. surge point is different and at a lower mass flow than the stall point), making their operability higher than for axial compressors, where the stall and surge points are usually the same.

Figure 1.4 illustrates the working principle behind a centrifugal compressor. The axial intake air (V_1) follows the direction of the blades of the impeller turning at a rotational speed (Ω) to exit the impeller at the relative velocity of V_{rel2} in the rotating frame of reference. In the process, the flow acquires a tangential velocity of ($\Omega \cdot r$) due to the impeller rotation, resulting in a much higher absolute velocity V_2. In other words, the work input to the impeller accelerates the flow ($V_2 > V_1$) and increased it kinetic energy. A diffuser is then used to reduce the circumferential velocity component and in doing so decelerates the flow, converting its kinetic energy into pressure rise (diffusion). The high flow turning (the change of the flow angle within a component), in the diffuser has a large impact on the aerodynamic losses and increases the tendency for flow reversal in the compressor as well.

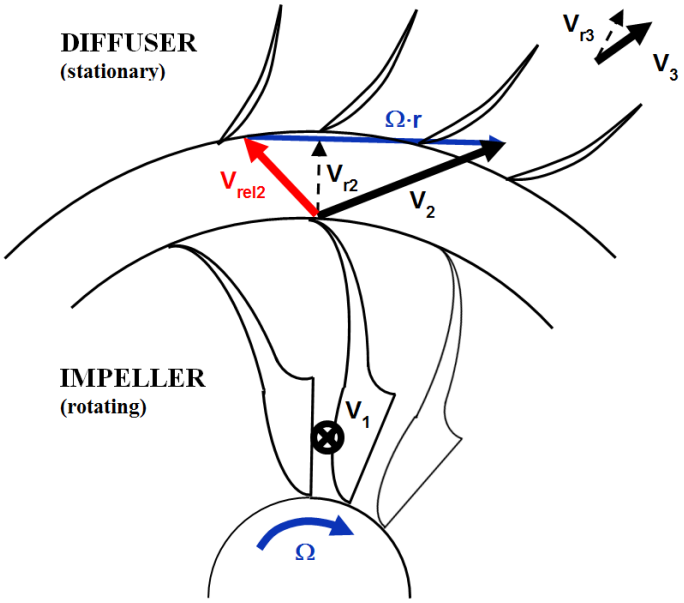

Figure 1.4 Working principle of a centrifugal (radial) compressor

The diffusion process can be done with blades (also known as *vaned diffuser*, as shown in Figure 1.4) to remove the circumferential velocity component within a short radial distance or simply by

letting the circumferential velocity and the radial velocity (V_r) radius decrease with increasing radius due, respectively, to conservation of angular momentum and increased normal flow area. The diffuser using the latter strategy is referred to as a *vaneless diffuser* and is the type used in most turbochargers due to its simplicity, even though it is less efficient than vaned diffusers due to the larger radial extent leading to higher viscous losses from the greater wetted surface. Nevertheless, vaneless diffusers are more widely used in turbochargers for their simplicity (lower cost) as well as their wider operating range.

Moreover, as illustrated in Figure 1.5, the centrifugal compressor used in turbochargers also includes a scroll-shaped *volute* used to collect the flow after its discharge from the diffuser. The volute has to be shaped with a progressive profile so the air can be collected smoothly, with the aim of attaining flow uniformity at the interface between the diffuser and the volute. However, its non-axisymmetric shape causes undesirable and harmful aerodynamic phenomena in the compressor. Due to the complexity of the flow in centrifugal compressors as well as the need to simulate the full annulus (360 degrees) to capture the asymmetric effects caused by the volute, the research into centrifugal compressors, particularly in terms of the effect of the volute shape on the compressor efficiency, has been very limited.

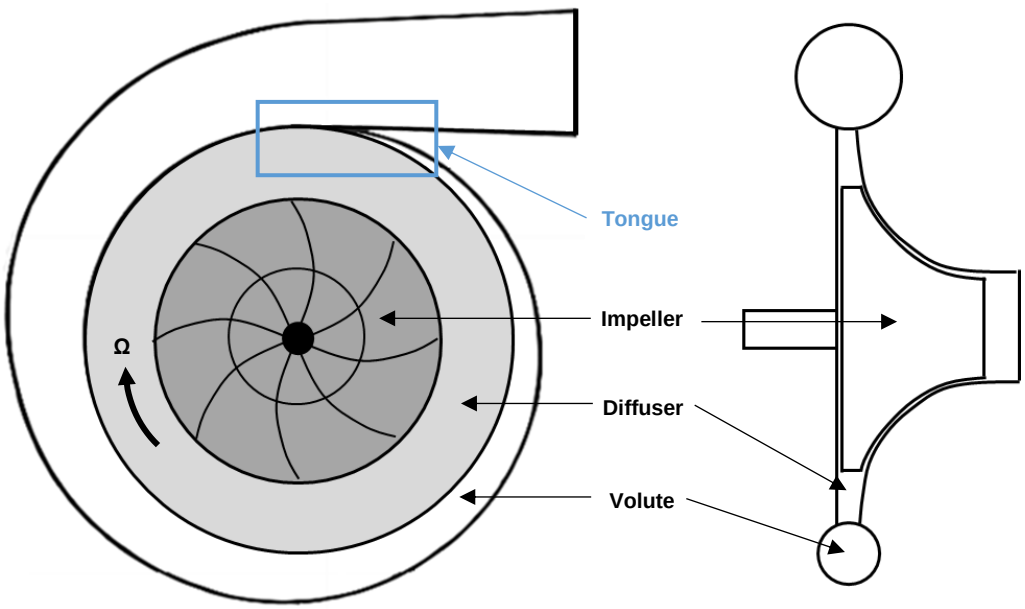

Figure 1.5 Schematic of a turbocharger compressor

Figure 1.6 shows the cross-section of a typical turbocharger with the centrifugal compressor and its components as well as the radial inflow turbine. The stationary assembly around the impeller that includes the volute, diffuser and impeller shroud is referred to as the *compressor housing*.

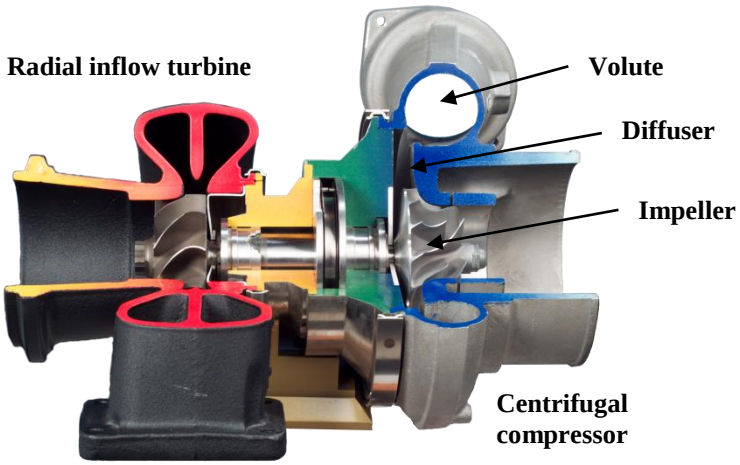

Figure 1.6 Turbocharger assembly cross-section[2]

1.3 Problematic

Experiments performed at Garrett Motion on a turbocharger compressor test rig for a small centrifugal impeller with two different compressor housings have shown a significant difference of 3% in adiabatic efficiency near their respective surge points for the same corrected speed. However, preliminary steady computational fluid dynamics (CFD) simulations with a sophisticated commercial code (ANSYS CFX) only captured about half of this difference. The failure to capture the full efficiency difference may be related to unsteadiness present in the flow field due to the proximity of the operating points in question to surge. Thus, there is a need to assess whether unsteady CFD simulations can better capture the observed difference in adiabatic efficiency near surge between the two housings and, if so, determine the adequate computational setup so that the simulation tool can be better used in the future for design purposes. In addition, it would also be of interest to identify the flow unsteadiness that may be at the source of the

[2] Reference: https://upload.wikimedia.org/wikipedia/commons/6/6e/Turbocharger_transparent_background.png

discrepancy in adiabatic efficiency between the steady CFD predictions and experimental observations to see how they can be considered in future designs.

1.4 Research Objectives

Based on the problematic outlined in section 1.3, the objectives of the current project are as follow:

1) Determine the utility of unsteady CFD simulations and the associated computational setup to capture the measured difference in adiabatic efficiency between the two turbocharger compressor housings near surge.
2) Investigate and describe key unsteady phenomena. These flow structures affect not only the aerodynamic performance but also the generated noise and the structural integrity of the compressor.

1.5 Thesis Outline

Following this introductory chapter, Chapter 2 will present a literature review on the design features and the relevant aerodynamic phenomena that affect the turbocharger compressor efficiency, as well as simulation methodologies used to simulate centrifugal compressors with a volute. Chapter 3 will present the methodology used to attain the objectives, including details on the two compressor housings and the computational setups. Subsequently, Chapter 4 will present the results for the first objective, namely, the CFD predictions associated with different computational setups compared to the test data. Chapter 5 will show the results from the analysis of flow unsteadiness. Finally, Chapter 6 will summarize the main conclusions from the current study.

CHAPTER 2 LITERATURE REVIEW

The chapter presents a literature review of the unsteady aerodynamic phenomena occurring inside turbocharger compressors and the housing design features that affect the compressor's performance in unsteady conditions. Finally, a short summary is provided on the CFD modelling used by other researchers to capture unsteady phenomena in a turbocharger compressor.

2.1 Aerodynamic Instabilities

Rotating stall and surge are the two aerodynamic instabilities that can induce highly unsteady flow in compressors operating at mass flows below their design point.

In the 1950's, Emmons et al. [1] proposed an explanation for the source of rotating stall. They suggest that the reduction in mass flow results in higher incidence angle on the blades results in a local rotor/impeller blade stalling (from boundary layer separation), causing a local blockage that decreases the incidence on one of the two neighboring blades while increasing the incidence of the other causing the stall cell to move circumferentially with respect to the rotor/impeller. The point at which rotating stall occurs can be affected by flow asymmetry caused by different factors such as the volute asymmetry [2].

The circumferential flow non-uniformity resulting from rotating stall induces velocity and pressure profile fluctuations in the impeller, as was found by Sorokes et al. [3] when investigating experimentally the effect of flow field non-uniformity in a turbocharger compressor.

Emmons et al. [1] also studied surge in a typical centrifugal compressor and classified the phenomenon into two different types, namely mild and deep surge, depending of the behaviour of the mass flow. Mild surge is characterized by an high amplitude oscillation of the mass flow rate through the compression system, but devoid of flow reversal (i.e no negative mass flow rate). On the other hand, deep surge involve intermittent flow reversal (negative mass flow rate).

Frigne et al. [4] conducted an experimental investigation of rotating stall in centrifugal compressors. The classified this phenomenon into three classes:

- Rotating stall caused by the interaction between high and low velocity regions in the vaneless diffuser;

- Sudden rotating stall due to the interaction between impeller and diffuser flows;
- Progressive impeller rotating stall caused by flow detachment at the impeller tip clearance.

Dehner et al. [5] [6] and others such as Liu et al. [7] studied the phenomena of rotating stall and surge in typical turbocharger compressor systems and used the Helmholtz frequency (f_H), as calculated with equation (2.1) to characterize the flow oscillations associated with mild surge in the compressor, where *a* represents the speed of sound, A_c is the equivalent cross-sectional area of the compressor inlet, *Vp* is the plenum volume and *Lc* is the equivalent duct length.

$$f_H = \frac{a}{2\pi}\sqrt{\frac{A_c}{V_P L_C}} \tag{2.1}$$

Fink et al. [8] verified the Helmholtz frequency equation on different centrifugal compressor stages operating in both mild and deep surge. Figure 2.1 illustrates their finding for cases with mild and deep surge. The dominant frequency when the compressor experiences mild surge is approximately equal to the Helmholtz frequency. On the other hand, the deep surge cycle, from instability onset to recovery, has a frequency that is an order of magnitude lower than the Helmholtz frequency.

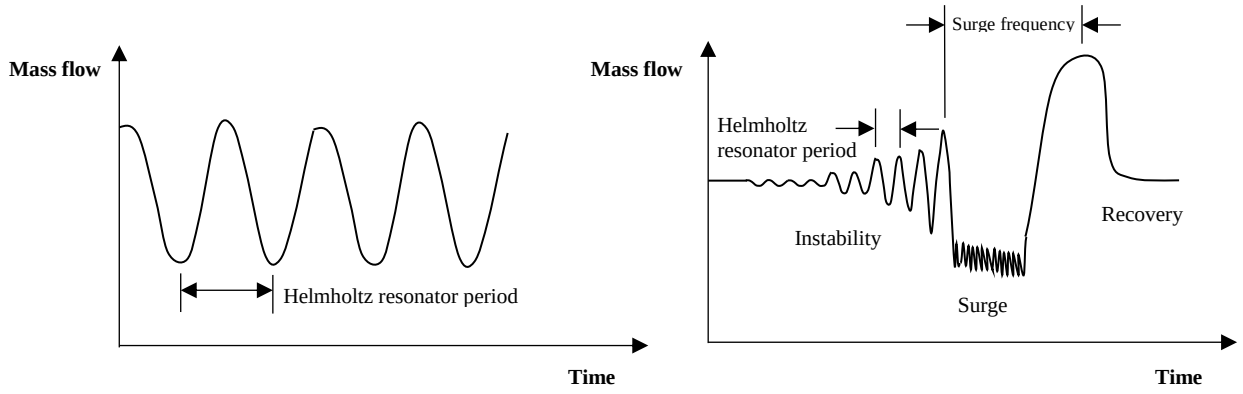

Figure 2.1 Evolution of mass flow for cases with mild (left) and deep surge (right)

According to Fink [8], a one or two percent reduction in throttle area suffices to provoke deep surge from a mild surge state. Zheng et al. [9] furthered investigated the link between mild and deep surge. They found that their occurrence in succession depends on the operating mass flow

and impeller rotational speed. Following the occurrence of mild surge at the Helmholtz frequency, a reduction in mass flow makes the mild surge temporarily vanish until the mass flow reaches a point where deep surge suddenly occurs.

2.2 Volute Flow Characteristics

2.2.1 Vortex Structure in the Volute

The non-axisymmetric nature of the volute shape induces flow phenomena not seen in widely studied axisymmetric compressors such as those used in aero-engines. The studies by Van den Braembussche et al. [10] and Ayder et al. [11] were the first to elucidate the three-dimensional flow in a volute.

Van den Braembussche et al. [10] used a conical channel to model a typical overhung turbocharger volute. A parallel wall was added upstream of the conical channel to represent the diffuser. They experimentally discovered how the flow moves in the volute. At the closest point to the tongue, the fluid enters at the smallest radius and fills the volute center. Then, the flow downstream of the tongue enters the volute at a bigger radius in a swirling manner by rotating around the initial upstream flow, concentrated in the center of the passage.

Ayder et al. [11] noted the same phenomenon when they experimented with a true volute shape. They also observed that this swirling flow in the center section of the volute causes important velocity gradients and shear stresses. As such, the higher the mass flow through the compressor, the higher are the losses in the volute due to high shear.

Gu et al. [12] and Khalfallah et al. [13] obtained similar streamlines patterns when they studied the flow inside a compressor subject to pressure distortion from the volute. At the design point, they found that streamlines from the diffuser hub go to the center of the volute to form what they called the *forced vortex*. On the other hand, the slower flow near the diffuser shroud goes on to rotates around the forced vortex, forming what they called a *free vortex*. Near surge conditions, the pattern changes due to a pressure distortion in the volute.

Kim et al. [14] studied the effect of the size modification of the diffuser and volute inlet by testing different sizes of diffuser outlet. Their test consisted in monitoring the flow in the diffuser

and volute to understand the effects of the diffuser enlargement at its outlet. They monitored the radial velocity out of the diffuser, claiming it to be the principal source of losses in the volute. They reasoned that a high radial velocity induces high swirl in the volute, resulting in high losses and lower the static pressure recovery. An increase in the diffuser exit height or diffuser length reduces radial velocity and increase static pressure. Yu et al. [15] showed a correlation between this design characteristic, such as the shape of the volute cross-section and its radial position, and the swirl at the volute inlet. Indeed, a longer diffuser lowers the radial velocity at its outlet for the same mass flow and rotation speed. As a result, the swirling in the volute is reduced and the flow exiting the diffuser hits the tongue at a lower velocity. However, a longer diffuser also results in higher viscous losses from a larger wetted area.

In parallel, an excessive increase of the diffuser exit height can result in flow separation in the diffuser. Yu et al. [15] also used the pressure recovery coefficient and loss coefficient to quantify the housings' performance relative to the change in diffuser exit height and found that increasing the height up to a certain point does benefit the pressure recovery and alleviates losses.

2.2.2 Pressure Distortion in the Volute

Hagelstein et al. [16] conducted an experiment to understand the circumferential static pressure distortion in a centrifugal compressor with a volute. By definition, the volute cross-sectional area increases in order to favor a constant mass flow from its inlet to the outlet and, at the same time, allow for a circumferentially uniform pressure distribution. Whereas this may be effective at design conditions, the volute behaves more as a diffuser a near surge to slow the entering flow. The resulting static pressure increase in the circumferential direction causes a distortion in the volute. According to Hagelstein et al. [17], depending on the shape of the volute, the diffusing effect can die out at about a circumferential position of $\theta = 200°$ relative to the tongue. This occurrence is an indication of flow separation in the volute, which leads to more perturbation. Shaaban et al. [18] proved this occurrence experimentally in a Honeywell-Garrett turbocharger compressor. They measured the static pressure distribution in the diffuser during its operation along the surge line. Their results show a sudden static pressure drop at a peripheral angle of about 180°, which concurs with the observations of Hagelstein et al. [17].

Moreover, a supplementary distortion is produced at the tongue because of the flow discontinuity that occurs at this location in the housing. Gu and Engeda [12] noticed this phenomenon in their simulations while studying the pressure distribution in a section of the volute and found the severe pressure perturbation occurring at the tongue region at low mass flow. Furthermore, this pressure distortion propagates upstream to affect the performance of the impeller [12]. In the long run, this phenomenon produces a cyclic throttling of the impeller flow as some blade passages are more affected by the pressure distortion than others [16].

2.2.3 Tongue Blockage

Flow distortion happening in the volute is a subject that has long been studied for both centrifugal compressors and pumps. In centrifugal pumps, the absence of a diffuser separating the wheel from the tongue makes the effect of the tongue more pronounced. Chu et al. [19] studied the flow field in a centrifugal pump and discovered that the pressure field varies strongly in the domain, both in the circumferential and radial directions because of the interaction between the jet-wake flows from the wheel and the tongue.

The tongue is also crucial for the return of the flow in the discharge duct. Depending of its shape and its size, the tongue can lead to flow perturbation downstream and upstream of its location, as verified by Dilin et al. [20] who compared two volutes with different tongues. One of the two volutes has a more rounded and smaller tongue in order to provide more flow recirculation in this location. Their results show that the tongue cutback helps decrease the size of flow separation in the region. On the other hand, at higher compressor mass flow, the flow does not get inside the volute to be diffused but instead exits directly through the outlet duct, which harms the compressor efficiency. Furthermore, preventing flow separation at the tongue helps to reduce upstream flow distortion in the diffuser and the impeller, especially near surge conditions.

Pan et al. [21] worked on understanding the effect of the enlargement of the flow passage near the tongue region. Their investigation consisted in analyzing different tongue shapes without altering the area ratio of the volute between the inlet and outlet. The results from their CFD analysis demonstrate that an enlargement of the flow passage near the tongue improves the uniformity of the pressure distribution around the volute and reduces flow distortion at every

operating condition, but more specifically near surge. Moreover, they found that the diffuser is a bigger beneficiary than the volute of the improvement of the flow near the tongue.

The tongue geometry can also cause considerable unsteadiness downstream of its location. Indeed, Wei et al. [22] studied the noise bands produced by their model of a centrifugal compressor in unsteady conditions and noticed an unknown frequency when they made a spectral analysis of the pressure fluctuation signal from their compressor outlet duct. By plotting the velocity distribution in the housing, the authors noted the presence of an obstruction region in the outlet duct that was generated, in fact, by a vortex-shedding phenomenon originating at the volute tongue. Its size fluctuated at the previously unknown detected frequency from their FFT analysis. Furthermore, after changing the geometry by rounding the tongue shape, they succeeded in attenuating this oscillating flow in the outlet duct.

The effect of the tongue shape on oscillatory flow generation in the outlet duct has been mentioned and it was seen that cutting the tongue radius was beneficial for the stability of the flow. On the other hand, Xu et al. [23] enunciated that the volute design consists in a compromise between a better performance range and better peak efficiency. A rounder tongue allows for better performance range while a sharp tongue is more sensitive to the flow angle of attack and improves efficiency for a very specific mass flow.

2.3 Flow Reversal in the Diffuser

Gu et al. [24] confirm, by their investigation, that the diffuser is a critical component when the mass flow is below that of the design point. From their CFD simulations, they calculated that the losses due to the vaneless diffuser increase by more than three percentage points when the flow rate was reduced by 25% below the design value. One of the explanations for such an increase in losses is the importance of the radial velocity distortion in the spanwise direction. Khalfallah et al. [13] studied the phenomenon while analyzing the interactions between the impeller and the vaneless diffuser in a turbocharger compressor. They noticed flow migration from the diffuser hub to the shroud and confirmed that the low-velocity secondary flow undergoes convection effects.

When investigating for the instability mechanisms in turbocharger compressors, Zheng et al. [25] also corroborated the presence of interaction between two different types of flow at the impeller/diffuser interface. According to them, the perturbation causing rotating stall originates from the interaction between the tip clearance flows and the region of high pressure and backflow in the diffuser due the non-uniform pressure field in the volute. Their research proved that this interaction contributes to the diffuser flow reversal whose effect reaches the impeller trailing edge and triggers stall of the impeller.

2.4 Impeller Secondary Flow

Vortices are produced by the secondary flow in the impeller. The main flow structures in an impeller blade passage are the core flow (high meridional velocity) and secondary flow (low meridional velocity). The secondary flow is composed of migrating blade/hub boundary layer flow and tip leakage flow. The tip leakage flow is the flow across small gap between impeller blade tip and the shroud and is driven by the difference in pressure across the gap. This flow is the main secondary flow in the impeller.

The meridional curvature of the impeller hub and shroud plays a crucial role in the generation of secondary flow [2]. The flow naturally migrates from the hub to the shroud due to the higher curvature in the shroud region, including separated, low-momentum flow, especially near stall conditions. This migration also interferes with the tip leakage flow, which occurs at the shroud, as shown on Figure 2.2.

Bousquet et al. [26] studied the impeller flow structures near stall. They found that a reduction in mass flow intensifies the secondary flow and increases the meridional velocity deficit. This generates two distinct flow regions: the core (normal) flow and a low-momentum flow region near the shroud.

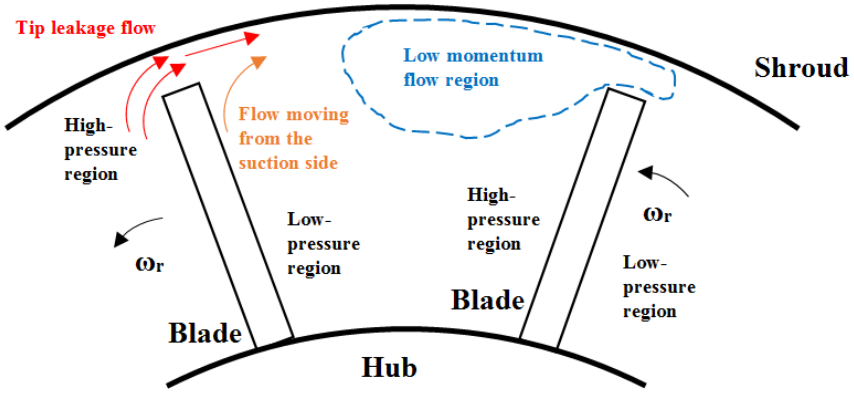

Figure 2.2 Secondary flow in a centrifugal compressor

Vortices are generated at the unstable interface between these flow regions and are transported downstream of the impeller, into the compressor housing. According to Bousquet et al. [27], the standard jet-wake structure usually observed at the trailing edge of the centrifugal compressor blades at the design mass flow is therefore affected by the interaction between the tip leakage flow and the migration of the low-momentum flow when approaching the stall point. The authors observed the development of vortices at a certain time period that is different to the blade passing frequency and that appears due to the Kelvin-Helmholtz instability.

2.5 Plenum and Exit Duct Size

During testing of a centrifugal compressor, Amann et al. [28] found that the plenum volume has a direct effect on the Helmholtz frequency at which the compressor will resonate. By reducing the plenum volume, they determined that the surge frequencies also changed, but not that associated with the rotating stall.

Galindo et al. [29] studied the effect of the change in length of a downstream exit duct on the surge of the compressor. They confirmed, both numerically and experimentally, that the detected frequency of the pressure pulsations in the outlet duct is dependent to the length of the duct and the opening size of the valve at the exit.

2.6 CFD Simulations Settings

Many authors have carried out CFD simulations centrifugal compressors with a volute, both in steady-state and unsteady modes. Table 2.1 summarizes the numerical settings of a representative sample of such works. Theses settings encompasses the choice of interface, boundary conditions, turbulence model, mesh type and mesh size.

In terms of the interface used in unsteady simulations, a *transient rotor-stator* interface (technically known as sliding plane interface) is used between the rotating impeller subdomain and adjacent stationary subdomains such as the diffuser. It allows for interpolating the flow properties from one grid to another across the interface. As such, circumferential flow non-uniformities are transferred across the interface. However, the circumferential extent of the domain on each side of the interface must be the same. Given the asymmetry of the housing, this means that a full impeller must be simulated. In the case of steady-state simulations, there are two possible interfaces: *mixing plane* and *frozen rotor*. The mixing plane interface (also named "stage interface") circumferentially averages the flow properties from the upstream subdomain. As such, it assumes that all passages of the impeller experience the same flow as single impeller passage [30]. The frozen rotor interface assumes phase lock two adjacent domain even though one rotates while the other is stationary.

As for the mesh, the entire domain is usually represented with a structured mesh except for the volute. Instead, the volute is meshed with an unstructured mesh because of the shape complexity [31]. Most of the work, which model the entire (full-annulus) compressor, have a total mesh size in the millions of elements.

Regarding the boundary conditions, the simulations in the literature all specify total pressure, total temperature and flow angle at the domain inlet. The exit boundary condition is either of constant mass flow or of static pressure.

Table 2.1 Summary of CFD simulations carried out for computation of flow field in a turbocharger compressor

	Guo's model [32]	**Jeon's model** [33]	**Sun's model** [31]	**Zheng's model** [25]
Software used	ANSYS CFX	ANSYS CFX	ANSYS CFX	ANSYS CFX
Geometry	Entire geometry of compressor (impeller, vaneless diffuser, volute)	Entire geometry of compressor (impeller, vaneless diffuser, volute, outlet)	Entire geometry of compressor (impeller, vaneless diffuser, volute)	Entire geometry of compressor (inlet duct, impeller, vaneless diffuser, volute)
Steady or unsteady model	Steady and unsteady	Steady and unsteady	Steady and unsteady	Steady and unsteady
Interface choice	Mixing plane (steady) Transient rotor/stator (unsteady) Timestep: 1.13e-5 s	Frozen rotor (steady) Transient rotor/stator (unsteady)	Frozen rotor (steady) Transient rotor/stator (unsteady)	Mixing plane (steady) Transient rotor/stator (unsteady)
Grid size in elements number	Impeller, structured (total): 1.6M Volute, unstructured: 800k	Impeller and diffuser, structured: 4.9M Volute, unstructured: 1.2M	Total: 5M Used TurboGrid for the impeller mesh	Inlet duct, structured: 248k Impeller, structured with TurboGrid: 350k per passage Diffuser, structured: 616k Volute, unstructured, 2.67M
Boundary conditions	Walls: non-slip Inlet: total pressure, total temperature, inlet flow angle Outlet: constant mass flow in steady state, plenum b.c. in unsteady	Walls: non-slip and adiabatic, smooth surface Inlet: Total pressure, total temperature, inlet flow angle Outlet: constant static pressure	Inlet: total pressure, total temperature, inlet flow angle Outlet: constant mass flow in steady state and transient near surge	N/D
Turbulence model	k-ε	k-ε	k-ε	SST
Near-wall model	Scalable wall function	Scalable wall function	Scalable wall function	Scalable wall function

In terms of turbulence models, while many authors uses the more traditional k-ε turbulence model, Zheng et al. [25] uses the more sophisticated SST turbulence model. This option is a hybrid between the k-ω and k-ε turbulence models in which the former is used in the inner region of the boundary layer and the latter in the principal streamline regions. This allows taking advantage of both models' coverage of the flow while limiting resource usage. Because of this polyvalence from the SST model, it is well suited for flows in centrifugal compressors. The wall boundary is usually defined as being no-slip with *scalable wall function* option.

Last but not least, Fatsis et al. [34] looked into the criterion to determine whether an unsteady simulation is necessary. They investigated numerically the effect of volute-induced static pressure distortions on the off-design efficiency of a centrifugal compressor and they perceived that the amplitude of flow perturbations propagating from the volute to upstream subdomains is influenced by the acoustic Strouhal number (*Sr*) in the compressor and is defined by equation (2.2), where f, L and a are respectively the number of rotations per second, the length of the blade passage and the speed of sound.

$$Sr = \frac{fL}{a} \tag{2.2}$$

According to Fatsis, the obtained Strouhal number is a good indication on whether a certain compressor operating mode can be simulated in steady state or in unsteady mode. In the case if Sr > 0.1, transient simulation is required. Because of the very high rotation velocity of the compressor to analyze as part of this research project, this implies a high value of f, which causes the Strouhal number to be very high. Therefore, flow distortions in such a compressor are expected to be severe and impactful on the stable operating range of the device. [35]

CHAPTER 3 METHODOLOGY

This chapter presents the methodology used to assess and compare the performance and flow field of two different turbocharger compressor housings. Given the objectives, a purely computational approach was taken to allow for assessing the capabilities of unsteady CFD simulations as well as investigation of the flow field. This chapter starts with a description of the compressor geometries under study, followed by an overview of the approach to address the two objectives, and a description of the computational setup and post-processing procedure.

3.1 Compressor Geometries

The turbocharger compressor under study, provided by Garrett Motion, is composed of an impeller placed inside a housing that incorporates a vaneless diffuser and a volute, sandwiched between inlet and exit ducts, as illustrated in Figure 3.1. Figure 3.2 depicts the overall test rig setup, from which the analyzed experimental data was obtained, as described by Garrett Motion.

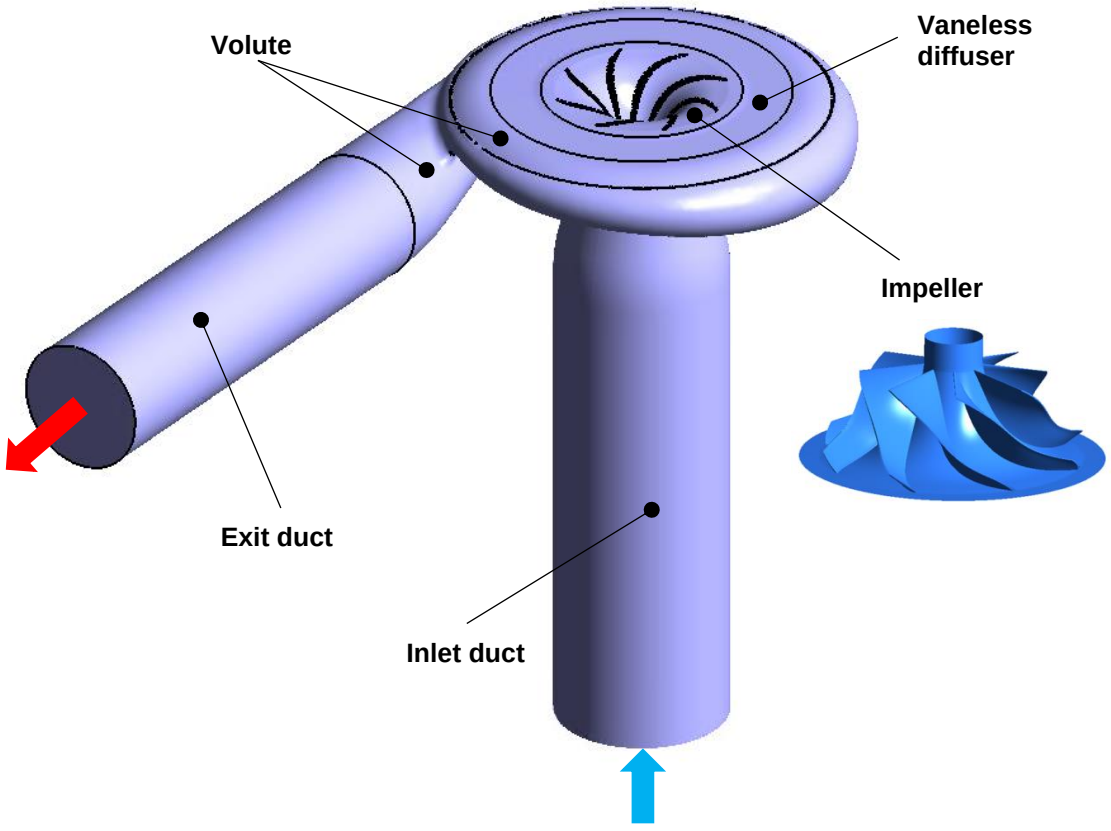

Figure 3.1 Compressor geometry

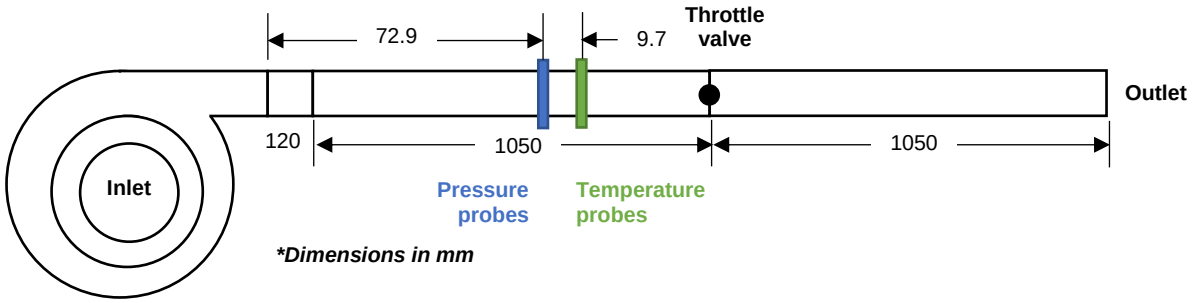

Figure 3.2 Schematization of gas stand setting of the turbocharger compressor

The impeller has a diameter of 46 mm with eight main blades and no splitter blades. Its design speed is a 220 000 RPM rotational velocity. The tip clearance varies between 0.32 mm at the impeller leading edge to 0.21 mm at the impeller trailing edge. Two housings of different shape and size, referred to as the E-housing and the H-housing, are used with the same impeller. Their geometries and characteristics are comparatively shown in Figure 3.3. The first noticeable difference in the housing is the diameter and width of the vaneless diffuser, with that in the H-housing being wider but shorter in radial extent. The second difference is in the volute geometry. Relative to the H-housing, the centerline of the volute exit for the-housing features a larger axial shift along with a divergent exit to increase exit area. This larger axial shift results in a larger bump at the intersection between the circular part and exit axial part of the volute. This intersection is often referred to as the *tongue*. The values of design mass flow for the compressor are 130.22 and 128.42 g/s for the E-housing and H-housing, respectively.

The inlet duct is simply a constant length duct with a convergent section just upstream of the compressor, as illustrated in Figure 3.4. Its length corresponds to 3.5 times the impeller inlet diameter, as provided by Garrett Motion. The hole in the middle of the duct exit accounts for the spinner.

The actual outlet duct in the test rig is shown in Figure 3.5. It consists of a conical divergent adapter that starts at the diameter of the volute exit and ends at the diameter of a 48.8 mm diameter long duct. However, at the suggestion of Garrett Motion, many simulations used a simplified model of the outlet duct as a constant area 130 mm long duct at the exit diameter of the volute.

E-Housing

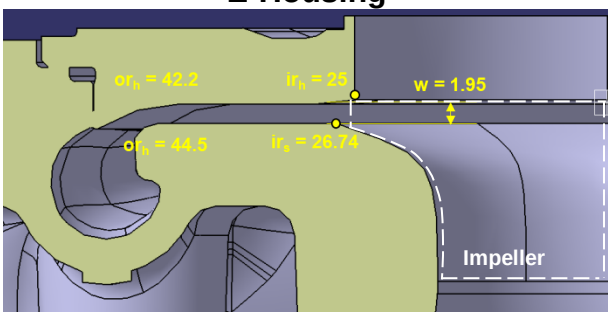

Dimensions in mm
Impeller shape not to scale
Inlet area: 351.03 mm^2
Outlet area: 516.98 mm^2
Hub diffuser ratio: 1.688
Shroud diffuser ratio: 1.664

H-Housing

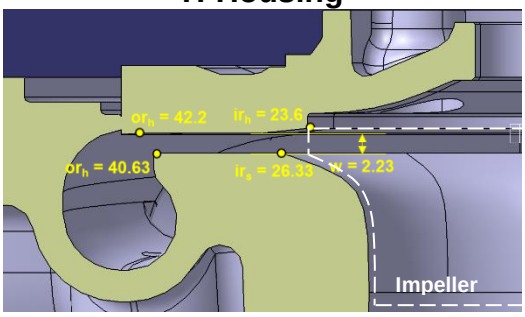

Dimensions in mm
Impeller shape not to scale
Inlet area: 401.43 mm^2
Outlet area: 569.29 mm^2
Hub diffuser ratio: 1.788
Shroud diffuser ratio: 1.543

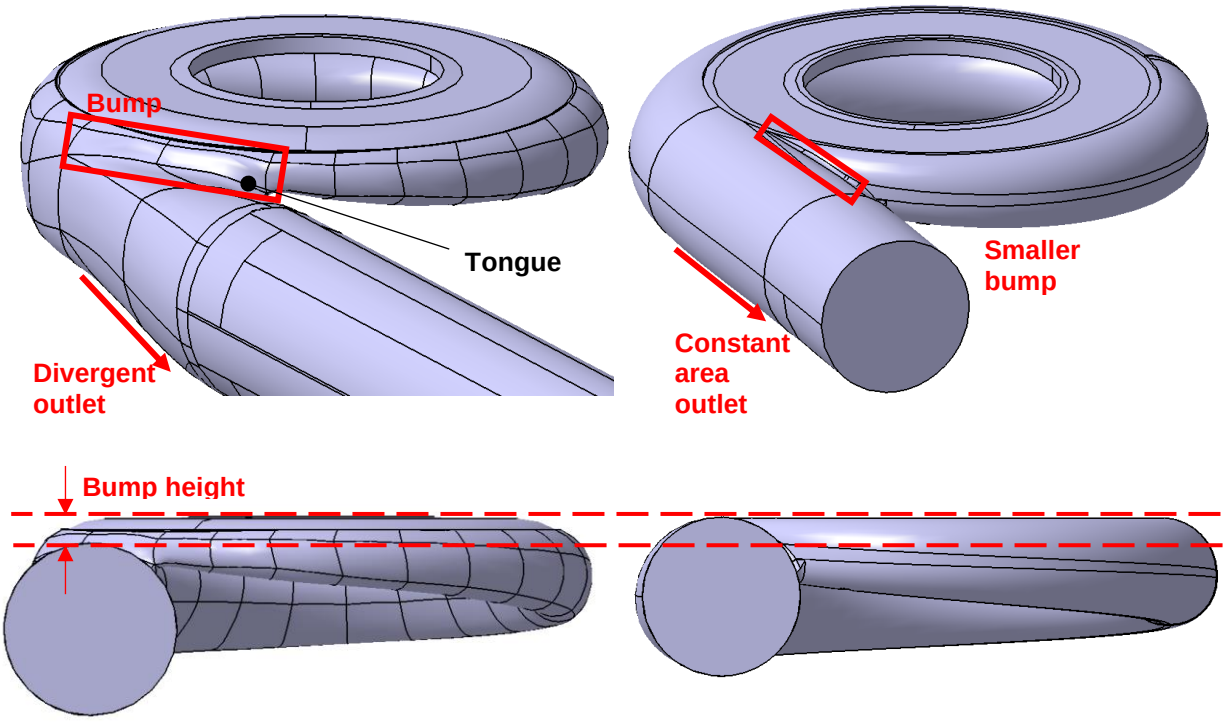

Figure 3.3 Comparison of housing geometries

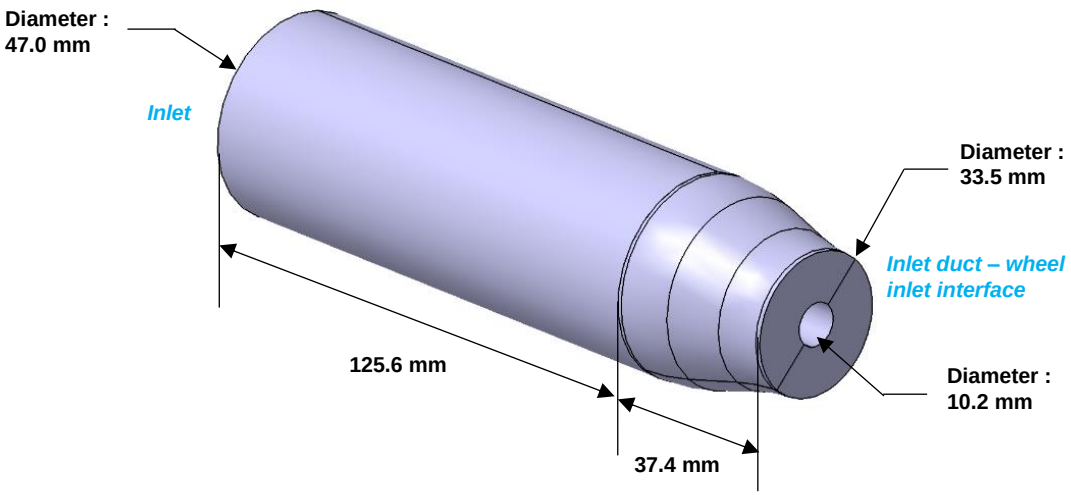

Figure 3.4 Inlet duct

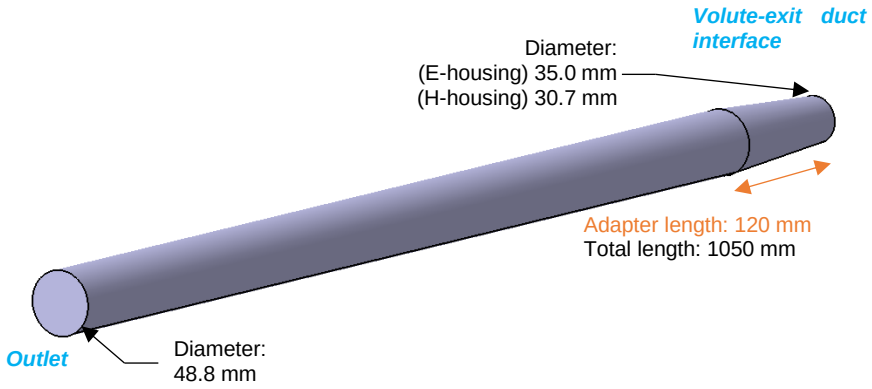

Figure 3.5 Outlet duct geometry

3.2 Overall Methodology

3.2.1 Usefulness of Unsteady Simulations

To address the first objective, which is to determine the capability of unsteady CFD simulations to capture the measured difference in adiabatic efficiency between the two housings, the adiabatic efficiency obtained from steady simulations and those from unsteady simulations are compared for the two housings. According to the Strouhal number corresponding to the studied case, there will be important unsteadiness and flow distortions in the compressor, which justifies the use of unsteady simulations [35]. The unsteady simulations involve variations in the numerical setup to

best model the test rig conditions. The simulated configurations for each of the two housings are based on two main numerical models, which are shown in Figure 3.6.

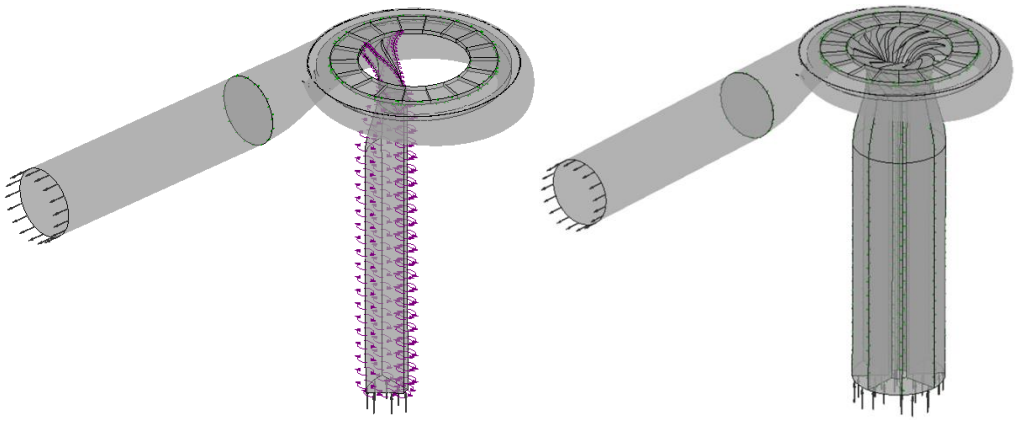

a) Single passage model (SP) b) Full-wheel model (FW)

Figure 3.6 Simulation configurations

The first model is the *single passage* (SP) model, which relies on the assumption of flow periodicity between the impeller blades passages and is often used in industry to save time and computational resources. As illustrated in Figure 3.6 a, the single passage model consists of simulating only one impeller blade passage, along with the same circumferential extent (in this case, $1/8^{th}$ of the circumference) in the inlet duct. A periodic condition applied to the lateral boundaries. On the other hand, the asymmetric housing compels the diffuser and volute to be modeled in full and a mixing plane interface is applied between the impeller and adjacent non-rotating subdomains (intake and diffuser), whereby only a spanwise profile of circumferential-averaged of flow properties are transferred across the interface. The flow unsteadiness brought about by the transfer of impeller blade wakes into the diffuser or by the breakdown in flow periodicity near surge due the presence of rotating instabilities or rotating stall (which are, respectively of low and high amplitude rotation perturbations) is not captured. As such, this model is strictly used for steady-state simulations and as a reference to standard industrial practice. The inlet boundary conditions consist of axial flow with specified uniform total pressure and total temperatures while the exit condition consists of a specified mass flow rate.

The second model is the *full-wheel* (FW) model, which models both the impeller and intake in full (360 degrees or full annulus) as shown in Figure 3.6 b. While this model is destined for

unsteady simulations, it is first used in steady-state mode with the same mixing plane interfaces and inlet and exit boundary conditions as the SP model. The steady-state full-wheel simulations serve two purposes. First, their results are compared with unsteady simulations to isolate the effect of unsteadiness from "parasitic" effect inherent in the transfer between the SP and FW model. Second, they serve as the initial guess for the unsteady simulations to reduce computational time.

In the unsteady mode, the FW model uses a sliding plane interface between the rotating impeller subdomain and adjacent stationary domains, allowing for circumferential variations in the flow properties to between transferred across the interface. To determine the numerical setup that best captures the measured difference in efficiency between the two housings, the configurations for unsteady CFD simulations are varied according to two parameters, namely the time step size and the nature of the exit boundary condition.

Time Step Size

The time step size is an important parameter in unsteady simulations. While smaller time step would improve accuracy and stability, it greatly increases simulation time, which is an important consideration in the present case where a full-annulus unsteady simulation is pursed. The time step expressed in this study through the number of time steps (N) per (impeller) blade passing. Simulations are carried out for N = 5, 10, 20 and 45 to see the effect of this parameter on the oscillation frequency and amplitude and time-averaged value of adiabatic efficiency in order to determine which value reflect best the experimental observations.

Exit Boundary Condition

Two types of exit boundary condition could be applied to unsteady simulations. The first is a specified mass flow rate, as applied in the steady-state simulations. The second is a throttle boundary condition that better replicates that in a real compressor test rig where the mass flow is determined by a valve placed downstream of the compressor outlet duct, as is the case here (see Figure 3.2). As illustrated in Figure 3.7, the throttle boundary condition essentially consists of a static pressure at the outlet of the computational domain that varies as a function of the local mass flow. This function is determined by the analytical model of a plenum-valve combination downstream. The plenum is modelled as a volume of compressible ideal gas and the valve as a quadratic pressure loss function of mass flow. The throttle boundary condition has been modelled

and implemented in the CFD code ANSYS CFX by Dumas [36] for the purpose of simulating surge in multi-stage compressors without requiring heavy computational resources. The details of the throttle boundary condition can be found in in Appendix A (section A.1).

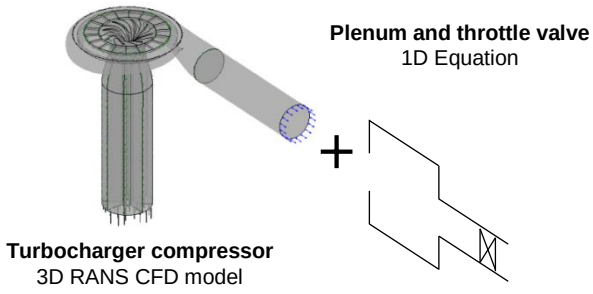

Figure 3.7 Throttle boundary condition

As illustrated in Figure 3.8, the throttle boundary condition has been applied in four different ways to the FW model, based on outlet duct length and plenum volume to try to best reflect the behaviour of the test setup described in Figure 3.2. The first two configurations use the proposed 130-mm long outlet duct model proposed by Garrett Motion, coupling it with a negligible plenum volume (Figure 3.8 a) or with plenum volume the size of the downstream duct to the throttle valve positon, as shown in Figure 3.2 to model any compressibility effect of the air in this duct (Figure 3.8 b). The next configuration incorporates the upstream half of the outlet duct up to the throttle valve into the computational domain to consider both the inertial and compressibility effect of the air in the duct section (Figure 3.8 c). Figure 3.8 d depicts a model with an excessively large plenum, which includes the volume of the pipe downstream of the throttle valve, likely to induce surge. While less reflective of the behaviour of the real setup, this configuration was essentially used to verify whether the throttle boundary condition could capture surge. The configuration in Figure 3.8 a is the standard configuration for unsteady simulations with throttle exit boundary condition for both housings, while those in Figures 3.8 b, c and d are only simulated for the E-housing near surge as a preliminary study of the effect of exit duct modelling. The configurations described above are simulated for each housing at the design speed (220 kRPM) and near-surge mass flow (78 g/s for E-housing and 72 g/s for H-housing) as well as at a common mass flow of 90 g/s for which test data for adiabatic efficiency were provided by Garrett Motion. The time-averaged adiabatic efficiency from the simulations are compared with the test data to see how accurately the unsteady simulations capture measure

adiabatic efficiency and its difference between the two housings the near-surge and 90 g/s conditions. This comparison will determine the usefulness of the unsteady simulations and the numerical setup required to best capture the experimental behaviour.

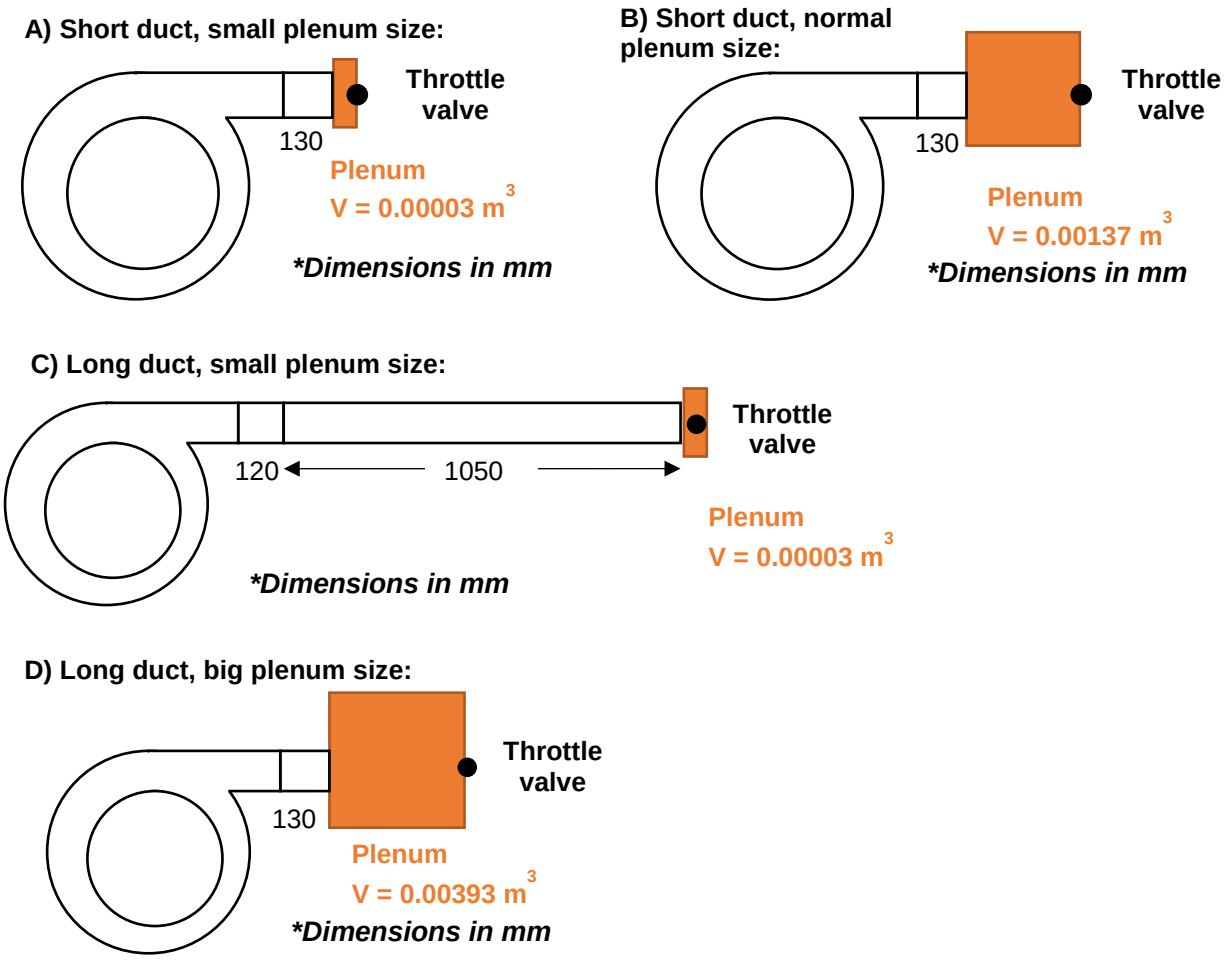

Figure 3.8 Unsteady FW configurations using the throttle boundary condition

Due to the large amount of CFD configurations and simulations, the nomenclature shown in Figure 3.10 is used to identify each simulation.

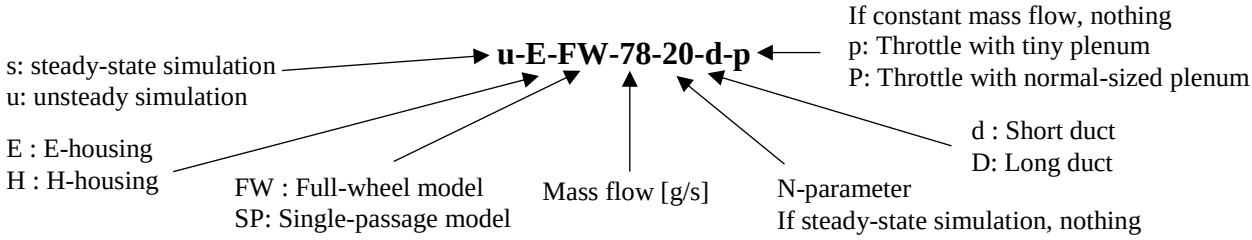

Figure 3.9 Nomenclature for identification of CFD simulations

3.2.2 Assessment of Unsteadiness

To address the second objective, which consists in an assessment of the unsteady flow structures, the unsteady simulations that best reflects the observed test data are selected for flow field analysis.

The first step consists of quantifying, for each housing, the unsteadiness though the identification of the dominating (largest amplitude) oscillation frequency of the adiabatic efficiency and locating the likely location of unsteadiness associated with this frequency. This is done through the placement of virtual probes at strategic locations in the flow field, namely at the impeller exit, diffuser exit, near the tongue and in the outlet duct (where the exit total pressure and temperature used for the efficiency calculation are taken). A Fast Fourier Transform (FFT) is performed on the pressure signal from these probes and on the time variation of the adiabatic efficiency to determine the dominating frequencies in terms of amplitude. The probe(s) whose dominating frequency matches that of the efficiency variation indicates the location(s) most likely at the source of the efficiency oscillation.

The next step is to investigate at the flow structures at these target location through contours of velocity and Mach number along with flow vectors at different time instants to determine the source of the unsteadiness in adiabatic efficiency.

3.3 Computational Setup

3.3.1 CFD Code

As recommended by Garrett Motion, ANSYS CFX was the chosen CFD code for the current study. It is a sophisticated commercial finite-volume Reynolds Averaged Navier-Stokes (RANS) CFD code that is extensively used in both industry and academia for turbomachinery simulations. While most of the project was carried out on a government computational cluster with ANSYS CFX Version 16.1, this version was no longer available following a change in this cluster near the end of the project. As such, the later simulations were carried out with ANSYS 18.1. A study was performed to ensure that the change is version did not fundamentally change the results (see Appendix B). The Shear Stress Transport (SST) turbulence model is chosen in all simulations as it has been shown to better capture the behaviour and separation of the boundary layer [25].

3.3.2 Computational Domains

The computational domain for each of the two models (single-passage and full-wheel) are composed of five subdomains, namely the *inlet duct*, *impeller*, *diffuser*, *volute* and *outlet duct*. Figure 3.10 and Figure 3.11 show the computational domains for the single-passage and full-wheel models, respectively, of the E-housing along with the interfaces and boundary conditions used. The domains for the H-housing are similar and have the same characteristics. They are shown in Appendix C. It is noted that the spinner, which is the impeller inlet cone, is not incorporated. Instead, it is modelled as cylindrical hub in the inlet duct subdomain with a free-slip boundary condition to avoid generating a boundary layer.

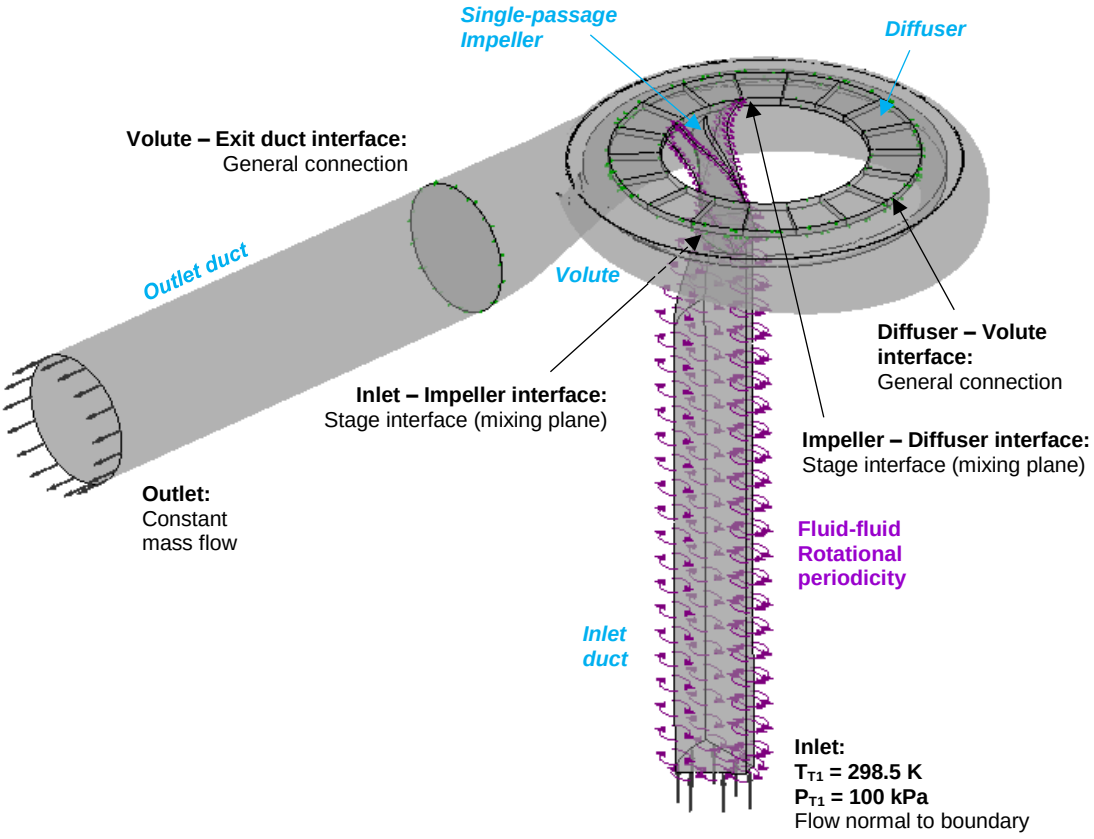

Figure 3.10 Computational domain for single-blade passage model

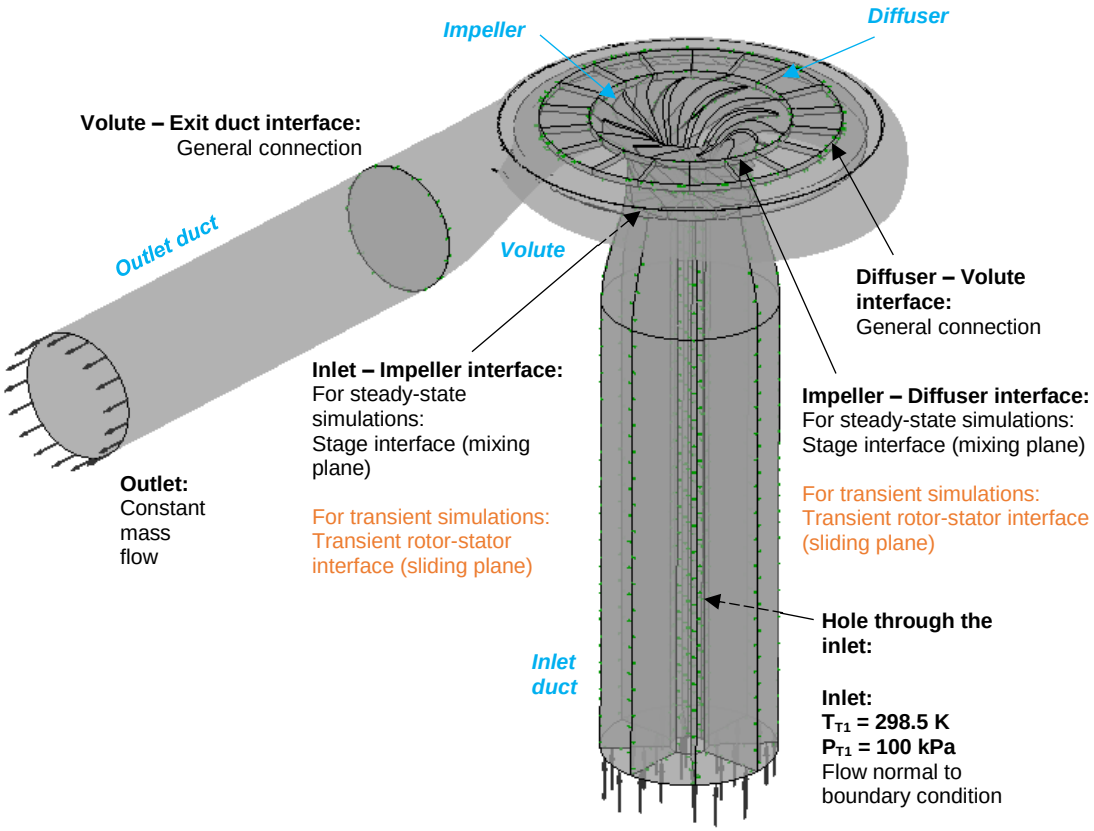

Figure 3.11 Full-wheel model and boundary conditions

Adjacent stationary subdomains (diffuser-volute, volute-outlet duct) are connected through a *general connection* interface through which the flow properties are simply interpolated from the mesh of one subdomain to that of the adjacent subdomain. On the other hand, the interface between a rotating subdomain (impeller) and a stationary domain (diffuser or inlet duct) is either a mixing plane (*stage*) interface for steady-state simulations or a sliding plane (*rotor-stator*) interface for unsteady simulations.

In terms of boundary conditions, all solid surfaces use a no-slip, smooth and adiabatic wall boundary condition in order to allow the development of the boundary layer. The automatic wall function option in CFX is activated at the surfaces to allow for a switch of the turbulence function from strictly no-slip (zero velocity) boundary to wall function depending of the local y+ value. At the inlet, a constant total pressure of 100 kPa and a constant total temperature of 298 K have been set for both models. The lateral boundaries of the inlet duct and impeller subdomains in the SP model have a periodic boundary condition (*fluid-fluid rotational periodicity*). In

addition, as the impeller subdomain is rotating, the stationary shroud is modelled as a counter-rotating, no-slip wall. At the computational domain inlet, specified uniform values of total pressures and total temperatures (provide by Garrett Motion) are applied along with a flow directionality set normal to the surface (i.e. axial inlet flow). The exit boundary condition consists of either a specified mass flow rate of a throttle boundary condition, explained earlier.

3.3.3 Computational Mesh

The computational domain shown in Figure 3.10 and Figure 3.11 were initially mesh using ANSYS Turbogrid for the impeller subdomain and the ANSYS Workbench meshing module for the other subdomains. The mesh was done as per Garrett Motion's best practices. In the end, their mesh was used in order to ease the comparison with their internal simulation results. The mesh density of the provided mesh has been verified in regards to what was found in the literature, as seen in section 2.6. Figure 3.12 shows the mesh of the inlet duct subdomain. It is a structured mesh with exclusively hexahedral elements. The mesh density is increased near the outer boundary to capture the boundary layer. For better representation of the boundary layers on the walls, the mesh has been refined. The inlet duct mesh has 64,192 elements in the SP model and 513,536 elements in the in the FW model.

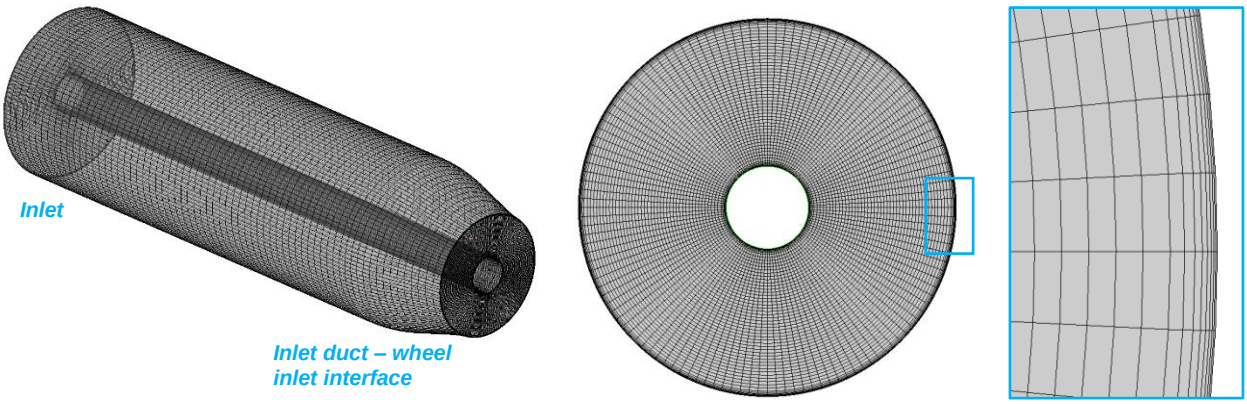

Figure 3.12 Inlet duct mesh

Figure 3.13 shows the mesh for the impeller subdomain. Mesh density is increased near the solid surface and in the tip clearance region to better capture effects of boundary layer and tip clearance flow, respectively. The tip clearance contains 10 elements in the spanwise direction. Each passage contains 514,291 elements, translating into 4,114,328 elements.

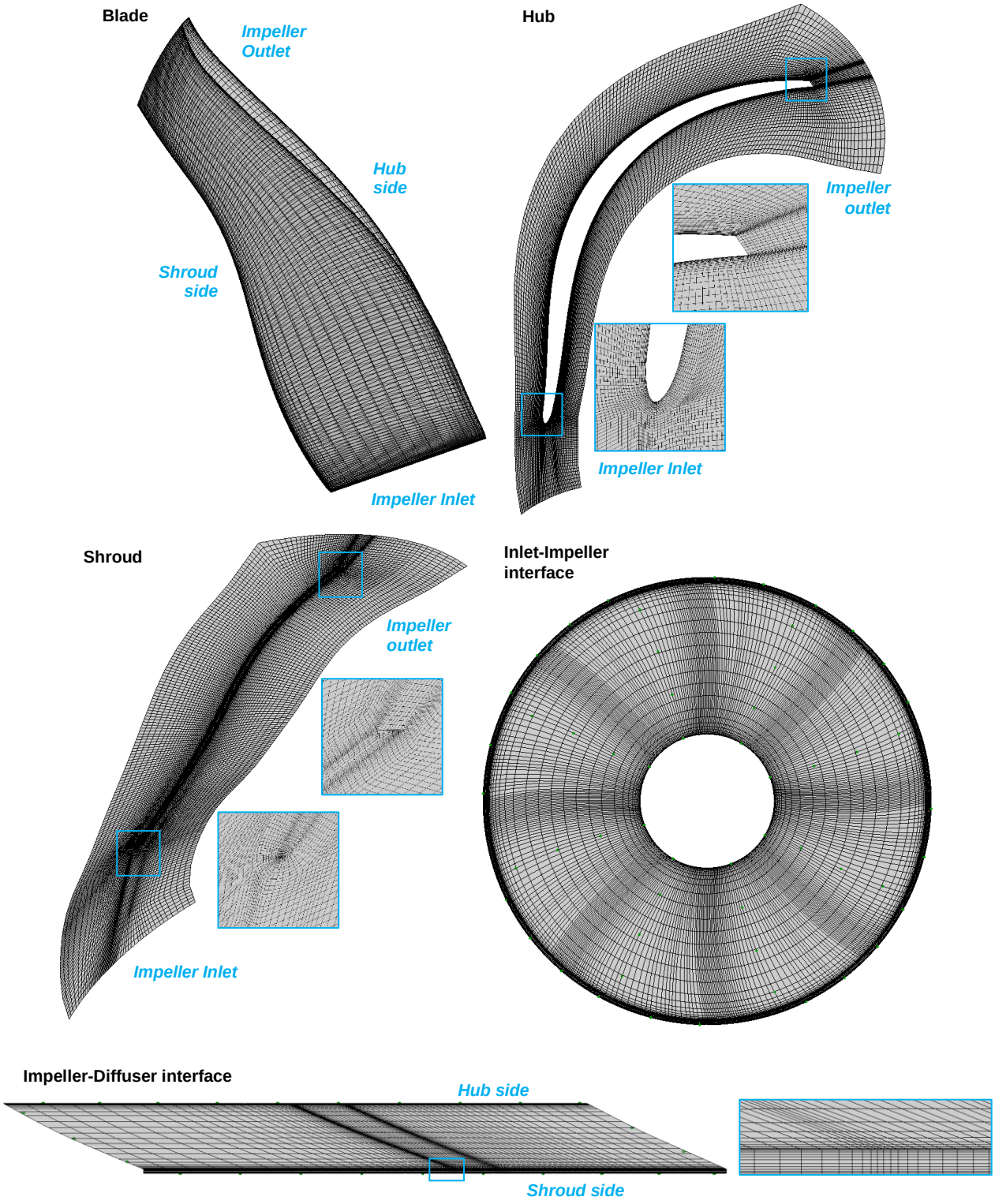

Figure 3.13 Impeller mesh

As for the housing, the diffuser and volute are meshed in distinct subdomains. The diffuser subdomain mesh, shown in Figure 3.14 for the E-housing, is a structured mesh composed of eight periodic sections given the axisymmetric nature of the vaneless diffuser. The mesh is very dense near the end walls to capture boundary layer evolution and its separation that can occur near surge. On the other hand, the asymmetric volute is meshed in a non-structured manner, which results in a combination of tetrahedral and wedge element cell geometries. The mesh is also denser at the solid surfaces and near the tongue in order to capture viscous flow effects in these regions that could be critical to the compressor performance. Moreover, the mesh has also been refined at the diffuser-volute interface in order to try to match the mesh density of the diffuser subdomain at this location to minimize any loss of information across this interface. It is also the case in the tongue region, where the flow may be critical due to this obstacle. Figure 3.15 and Figure 3.16show the mesh for the volute of the E-housing and H-housing, respectively.

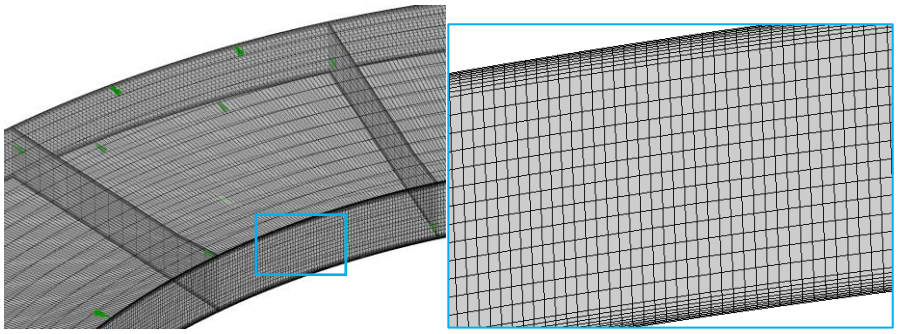

Figure 3.14 E-housing Diffuser mesh

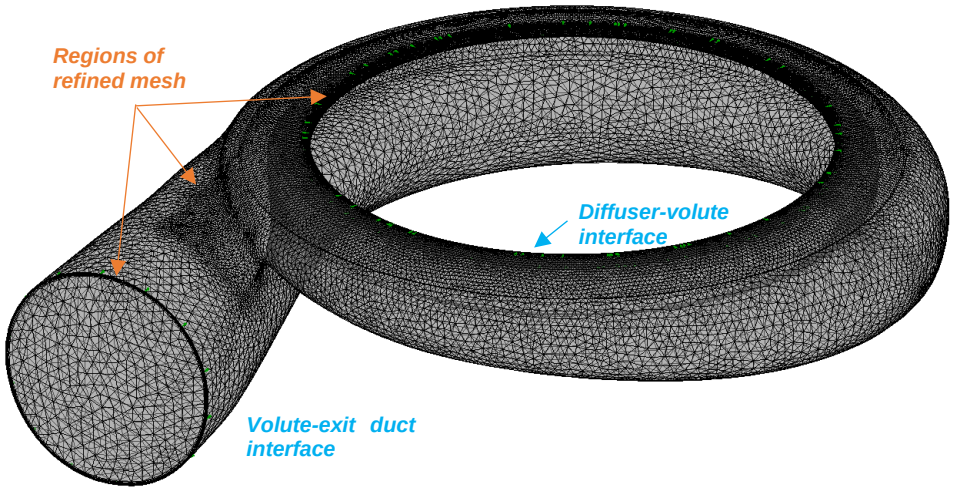

Figure 3.15 E-Housing mesh

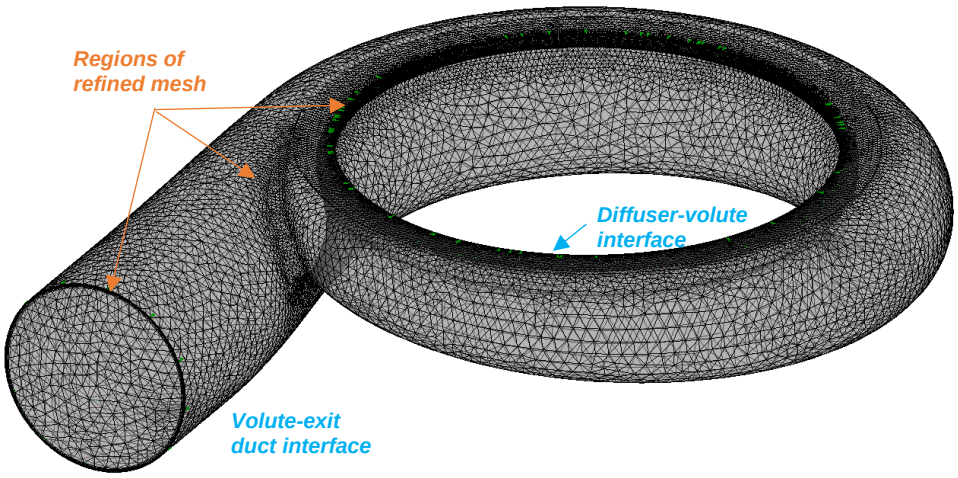

Figure 3.16 H-Housing mesh

For both housings, the mesh for the outlet duct is also non-structured and relatively coarse, except near the walls where high mesh density is kept capture boundary layer phenomena. Figure 3.17 shows the mesh for the E-housing outlet duct.

Table 3.1 gives the number of elements (total and breakdown among the subdomains) in the computational domains for the E-housing and H-housings with the 130-mm meshed outlet duct.

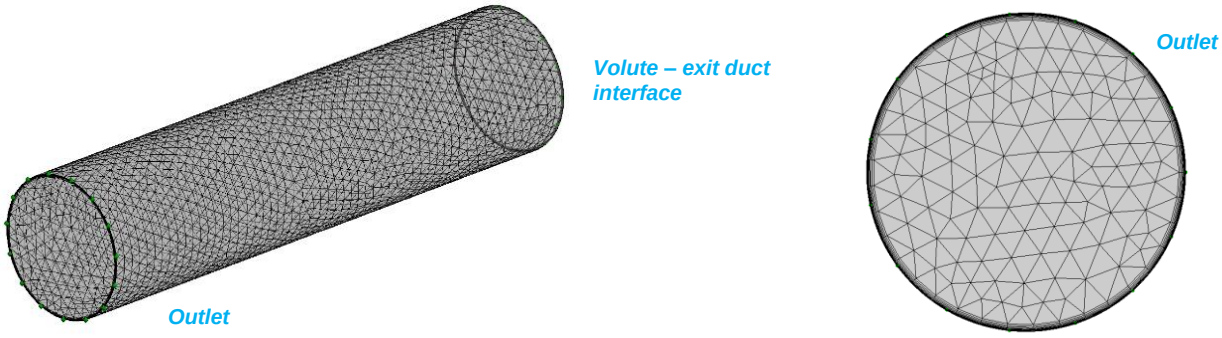

Figure 3.17 E-housing outlet duct mesh

Table 3.1 Number of elements in the E and H housings

Number of elements	E-Housing			H-Housing		
	Single-passage	**Full-wheel, short duct**	**Full-wheel, long duct**	**Single-passage**	**Full-wheel, short duct**	**Full-wheel, long duct**
Inlet (S)	64,192	513,536		64,192	513,536	
Wheel (S)	514,291	4,114,328		514,291	4,114,328	
Diffuser (S)	789,264			694,710		
Volute (NS)	875,650			725,675		
Outlet (NS)	96,814		894,112	84,758		884,798
Total	**2,340,211**	**6,389,592**	**7,186,890**	**2,083,626**	**6,133,007**	**6,933,047**

3.3.4 Simulation Procedure

For each housing, the simulation procedure consists first of simulating the single-passage model in steady-state mode at near-surge and 90 g/s to serve as a reference with regard to standard industrial practice. The full-wheel model is then simulated at the same mass flows to serve as the steady-state baseline from which subsequent unsteady simulations can be compared to be isolate the effects of unsteadiness.

Finally, using the full-wheel steady-state solution as an initial condition, the unsteady simulations are carried out. The unsteady simulations with the exit mass flow boundary conditions were simply carried out by putting the same exit mass flow rate value as those of the corresponding steady-state simulations. However, for the simulations with the throttle exit boundary condition, the value throttle constant (representing a valve opening area) corresponding to the desired exit mass flow value must be determined. This was done in an iterative process as described in Appendix A (Section A.2). In unsteady simulations, one can expect a time-varying converged solution in which a parameter, such as adiabatic efficiency, oscillates around an effectively constant mean value. In this case, an FFT is performed on the time history of the adiabatic efficiency in the time interval where the solution has converged to determine the time period over which to average the adiabatic efficiency and flow field. This time period corresponds to the lowest frequency, which in the present study often corresponds to the frequency with the highest amplitude. The unsteady simulation is then restarted and run over the an integral number of the specified time period with the option for time-averaging enabled as well as a request for CFX to

save instantaneous solutions at regular intervals covering a period in order to study the variation of the flow field.

3.4 Performance Parameters Calculation

3.4.1 Standard Parameter Calculation

The three main standard performance parameters are the mass flow, total pressure ratio and adiabatic efficiency, which are defined according to equations (3.1) and (3.2).

$$PR_{TT} = \frac{P_{T,out}}{P_{T,in}} \tag{3.1}$$

$$\eta_{TT} = \frac{T_{T,in}}{T_{T,out} - T_{T,in}} \left(\left(\frac{P_{T,out}}{P_{T,in}} \right)^{\frac{\gamma-1}{\gamma}} - 1 \right) \tag{3.2}$$

The inlet and outlet total pressure and total temperature are mass-flow averaged through the plane where the measures are taken. The planes where these properties and the mass flow are recorded from are indicated in Figure 3.18. In the case of oscillatory unsteady simulations, these properties are also time-averaged.

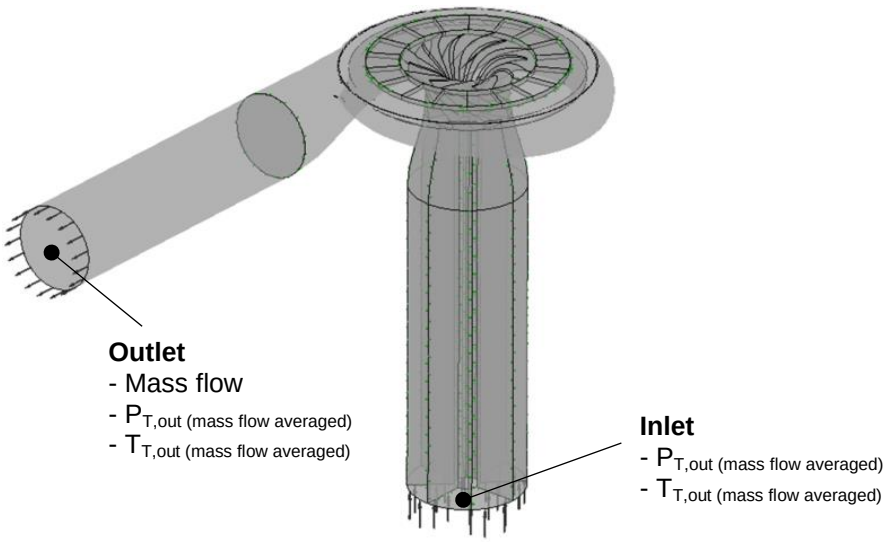

Figure 3.18 Location of planes where flow properties have been recorded

3.4.2 Alternative Adiabatic Efficiency Calculation

While the method for calculating adiabatic efficiency from CFD simulations shown in equation (3.2) is commonly used in industry and academia. It may not be the best method for a back-to-back comparison with test data. The reason is that a mass averaging of total pressure and temperature is not easily obtained experimentally. While this fact may not be an issue here for the inlet total pressure an temperatures that are expected to be relatively uniform, it can be a problem for the value of these parameters at the outlet of the compressor, where the flow can be highly non-uniform. The downstream pressure and temperature measurement locations for the compressor test rig at the source of the current project are shown on the outlet duct in blue and green planes in Figure 3.2. The exit pressure measurement consists of static pressure ports on the duct walls, which would be equivalent to either an area-average static pressure or a line-averaged static pressure along the end wall. The total temperature comes from the average of three probes protruding at different radial depth inside the duct at the same axial location, which would correspond to an area averaged total temperature. While not explicitly provided by Garrett Motion, Figure 3.19 shows the deduced method by which the total pressure can be estimated from these exit static pressure and total temperature measurements to obtain the measured adiabatic efficiency.

Step 1 – Calculate fluid density: $\rho_{out} = \frac{P_{s,out}}{R\,T_{S,out}}$

Suppose that** $T_S = T_T$ **for the first step

Step 2 – Calculate fluid velocity: $v_{out} = \frac{\dot{m}_{out}}{\rho_{out} A_{out}}$

Step 3 – Calculate the static temperature: $T_{S,out} = T_{T,out} - \frac{v_{out}^2}{2\,cp}$

Steps 1 to 3 are being repeated until a constant value of v has been reached.

Step 4 – Calculate the Mach number: $M_{out}^2 \cong \frac{v_{out}^2}{\gamma R T_{out}}$

Step 5 – Calculate the total pressure: $P_{T,out} = P_{s,out}\left(1 + \frac{\gamma-1}{2} M_{out}^2\right)^{\frac{\gamma}{\gamma-1}}$

Step 6 – Calculate the isentropic efficiency: $\eta_{TT} = \frac{T_{T,in}}{(T_{T,out} - T_{T,in})}\left(\left(\frac{P_{T,out}}{P_{T,in}}\right)^{\frac{\gamma-1}{\gamma}} - 1\right)$

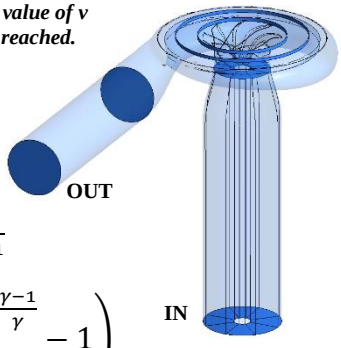

Figure 3.19 Deduced calculation method for adiabatic efficiency from test data

The procedure laid out in Figure 3.19 was also applied to CFD data using area-averaged or circumferentially line-averaged static pressure at the exit plane for $P_{S,out}$ and area-averaged total temperature at the exit plane for $T_{T,out}$ to calculate an alternative adiabatic efficiency value. This was done to determine whether the results compared better with measured adiabatic efficiency values and to quantify the effect on the efficiency value relative to the standard CFD mass-averaging method.

CHAPTER 4 RESULTS – CFD SETUP STUDY

This chapter presents and discusses the results from the CFD simulations to assess the capability of unsteady simulations to capture the full discrepancy in adiabatic efficiency between the housings as measured on a test stand and to determine the best setup for the unsteady simulations.

4.1 Steady-state simulations

Table 4.1 lists the adiabatic efficiency predicted through steady-state simulations using both the single-passage (SP) and full-wheel (FW) models, with the regular (d) as well as long outlet duct (D) configurations, for comparison with test data. The column labelled "Δ" lists the difference in efficiency between the E and H-housings. The last row also show the efficiency obtained through the alternative calculation method as described in section 3.4.2 for the full-wheel model with the long duct. While the results shown are at the near-surge points and 90 g/s mass flow conditions, steady-state simulations were also carried out at other mass flow values as well as with long outlet duct (similar to that in Figure 3.8 c) for further comparison with test data, as demonstrated in Appendix D (section D.1). Moreover, a convergence analysis was carried out with respect to the time-scale setting in steady-state mode to ensure that the value used was adequate (Appendix D, section D.2).

In terms of the absolute adiabatic efficiency, Table 4.1 indicates that while the SP and FW models give similar predictions in steady-state mode in all cases, for both housings, they both overestimate the adiabatic efficiency relative to the test values. This overestimation is slightly higher for the H-housing can reach 2.12 percentage points near surge and 3.11 points for a mass flow of 90 g/s. Finally, the alternative calculation method increases the absolute efficiency by 1.5 to 2 points, adding to the overestimation of the efficiency with respect to the measured values.

In terms of the difference in adiabatic efficiency between the E and H-housings, the results in Table 4.1 shows that, regardless of the model, the steady-state simulations can only capture between 2.4 and 2.6 percentage points out of the 3.5 points measured on the test stand near surge. At 90 g/s mass flow, the steady-state simulations only capture about a quarter of the measured two percentage points in efficiency difference between the housings. It remains to be seen whether this shortfall cap be captured by unsteady simulations.

Table 4.1 Efficiency prediction from steady-state simulations for E and H housings

	Near surge			**m = 90 g/s**		
	E – 78.09 g/s	**H – 72.42 g/s**	**Δ**	**E – 90 g/s**	**H – 90g/s**	**Δ**
η experimental data	65.50%	62.02%	**3.48%**	67.40%	65.40%	**2.00%**
η single blade model (s-SB-d)	66.75%	64.14%	**2.61%**	69.04%	68.51%	**0.53%**
η full wheel model (s-FW-d)	66.80%	64.40%	**2.40%**	69.21%	68.69%	**0.52%**

4.2 Unsteady Simulations

In order to determine if and which numerical setup unsteady simulations can best capture the full extent of the measured efficiency difference between the E and H-housings at near stall and 90 g/s mass flow, many unsteady simulations of the full-wheel model have been performed at these two conditions for both housings.

The first of these simulations covers how the variations of the two main parameters affect the setup, as laid out in section 3.2.1, namely:

- The time step (Δt) expressed in number of time step (N) per impeller blade passing
- The mass flow versus throttle exit boundary condition (with short outlet duct and negligible plenum volume, as illustrated in Figure 3.8 a)

Unsteady simulations for both housings and at both mass flow and throttle boundary conditions were carried out at N=5, 10 and 20, representing Δt= 6.818e-5, 3.409e-6 and 1.705e-6 second, respectively. Even for the N=5 simulations, it takes around two weeks on four Intel Xeon X5650 Westmere (2.67 GHz) processors, with 12 cores each, to obtain converged solution with three low-frequency oscillatory period. The whole list of running times for each simulation is shown in Appendix E. The simulation times becomes proportionally higher for higher values of N. A simulation was carried out at N=45 (Δt = 7.576e-7 second) for the E-housing with throttle exit boundary condition. However, it was not found to add much information from the equivalent N=20 simulation while requiring an excessively long simulation time, as detailed in Appendix F.

Thus, N=45 was not further pursued. Section 4.2.1 presents and discusses the results of these simulations with the short outlet duct.

Subsequently, unsteady simulations for the E-housing with variations in the outlet duct length and plenum volume as outlined in Figure 3.8 b, c and d were performed at near near-surge to investigate the effect of the outlet duct modelling on the unsteady simulation behaviour. The results from these simulations are discussed in section 4.2.2.

4.2.1 Effects of Time Step and Throttle

Near-Surge Conditions

Figure 4.1 and Figure 4.2 show the oscillatory convergence time history of the adiabatic efficiency for the E-housing near surge using the constant mass flow and throttle exit boundary conditions, respectively. For each curve, the point indicates the time from which the unsteady solution is considered to be converged and from which temporal averaging is done for the efficiency calculation. Figure 4.3 and Figure 4.4 show the equivalent data for the H-housing. A first glimpse of these results shows a clear disparity in unsteady behaviour between the two housings near surge. The E-housing simulations exhibit large amplitude oscillations in adiabatic efficiency (in the order of three percentage points), whereas the H-housing oscillations are one order of magnitude smaller.

As mentioned is section 3.4.1, the time-averaged efficiency value for each curve was obtained by first identifying the time period associated with the largest-amplitude frequency and then averaging the time history of the adiabatic efficiency over an integer number of periods starting from the point of convergence. Table 4.2 lists the values obtained using different numbers of periods for the E-housing data shown in Figure 4.1 and Figure 4.2. The results show that the values is relatively unaffected by the number of periods chosen. Although not shown, a comparison of the adiabatic efficiency obtained based on the above technique with the value obtained based on a time-averaged flow field (over the same period) show that both techniques yield virtually the same answer.

Table 4.3 lists the time-averaged adiabatic efficiency for the data shown in Figure 4.1 to Figure 4.4 along with the corresponding predictions from steady-state simulations and from the test data.

For the cases with a throttle exit boundary condition, in spite of fine-tuning the throttle constant, the time-averaged mass flow is usually slightly offset from the target value. Thus, the efficiency value as shown in Table 4.3 has been corrected to the target mass flow value using the procedure outlined in Appendix A (section A.3). As with Table 4.1, the column labelled "Δ" lists the difference in efficiency between the E and H-housings and the efficiency obtained through the alternative calculation method as described in section 3.4.2 is also shown.

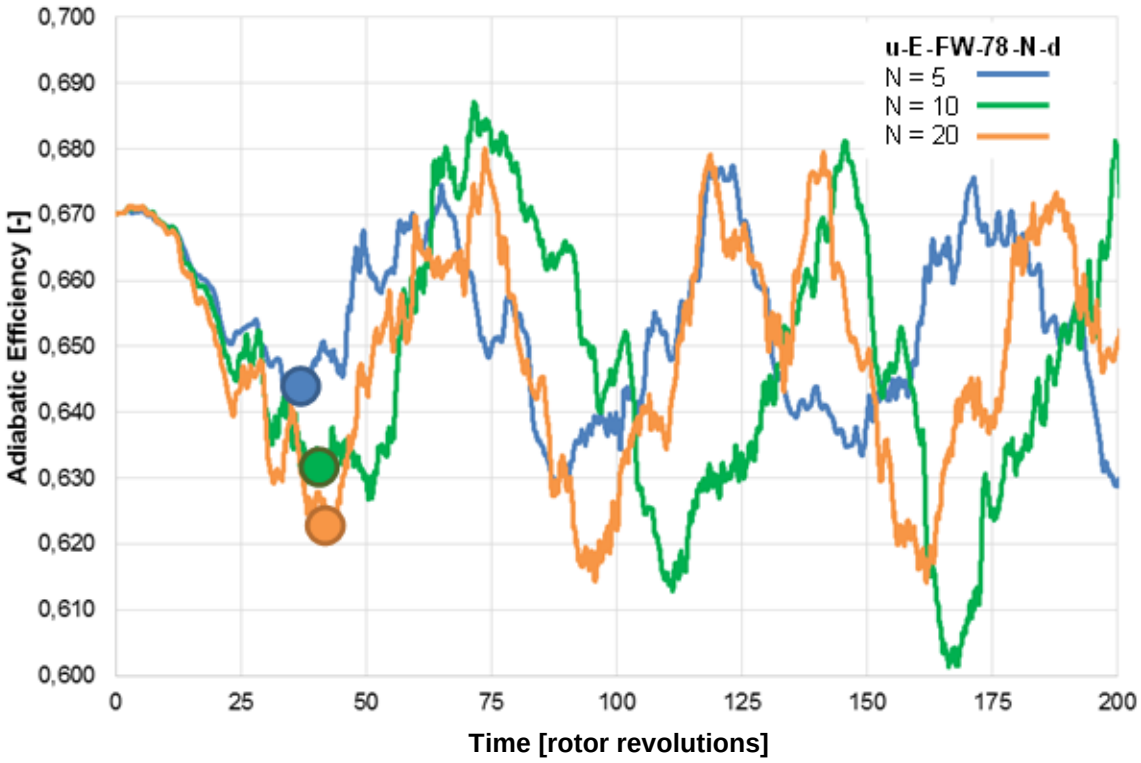

Figure 4.1 Unsteady convergence time history of adiabatic efficiency for **E-housing near surge** (78.09 g/s), short duct model with **exit mass flow b.c.** (u-E-FW-78-N-d)

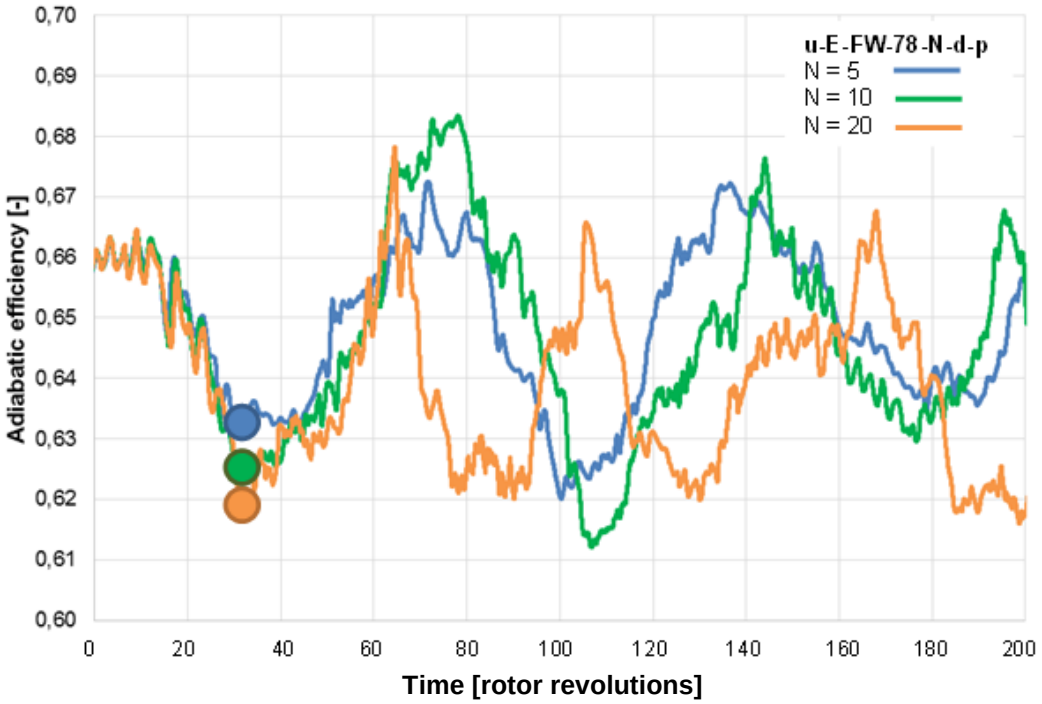

Figure 4.2 Unsteady convergence time history of adiabatic efficiency for **E-housing near surge** (78.09 g/s), short duct model with **throttle b.c.** (u-E-FW-78-N-d-p)

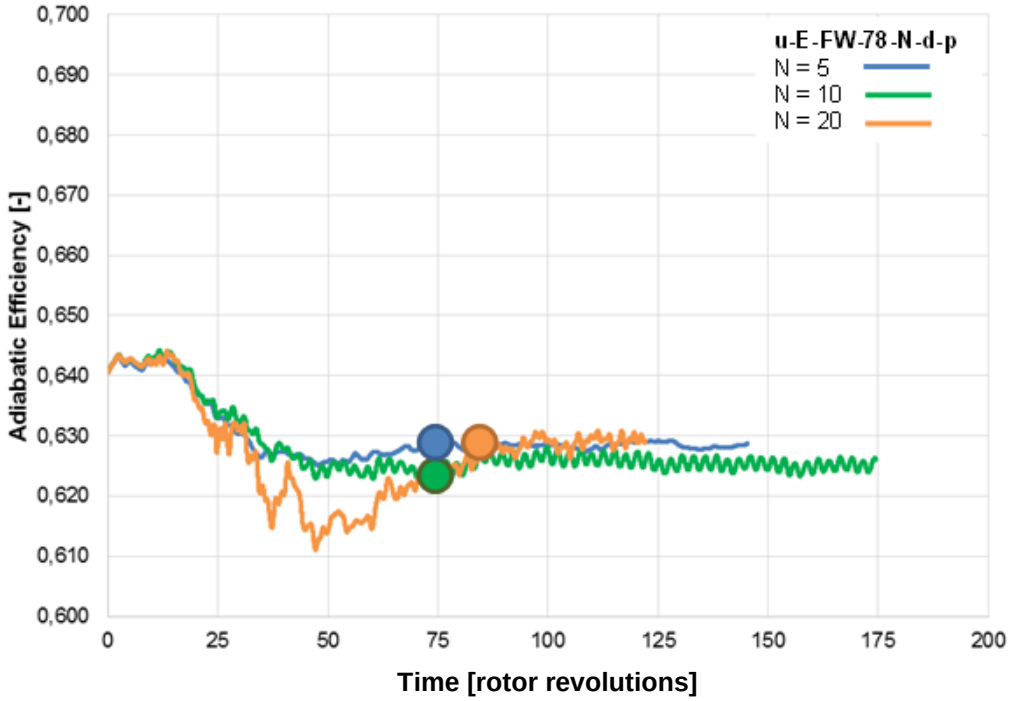

Figure 4.3 Unsteady convergence time history of adiabatic efficiency for **H-housing near surge** (72.42 g/s), short duct model with **exit mass flow b.c.** (u-H-FW-72-N-d)

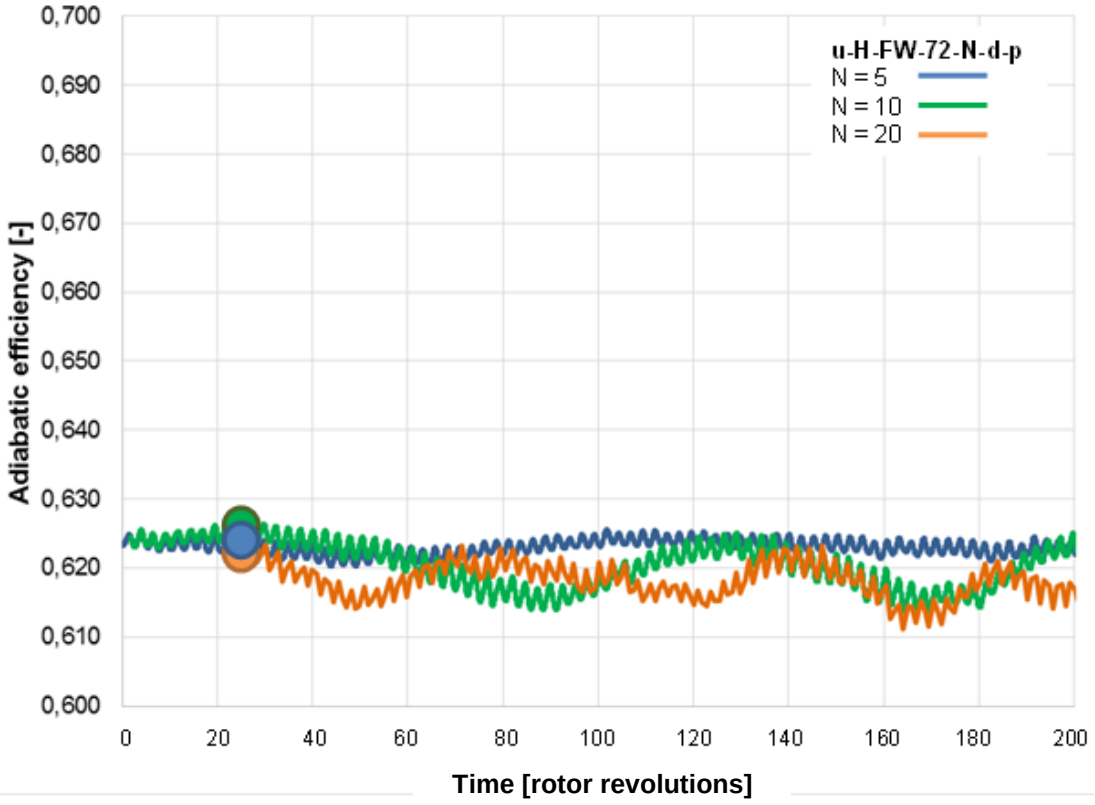

Figure 4.4 Unsteady convergence time history of adiabatic efficiency for **H-housing near surge** (72.42 g/s), short duct model with **throttle b.c.** (u-H-FW-72-N-d-p)

Table 4.2 Effect of the number of periods on time-averaged adiabatic efficiency (E-housing)

	E-Housing average η [%]						
	Constant m (u-H-FW-78-d)			**Throttle (u-E-FW-78-d-p)**			
	N=5	**N=10**	**N=20**	**N=5**	**N=10**	**N=20**	**N=45**
1 period	65.9	65.3	65.2	65.1	65.2	64.1	63.6
2 periods	65.5	65.1	65.1	64.9	64.8	64.0	N/D
3 periods	65.4	65.4	65.0	65.1	64.7	64.0	N/D
4 periods	N/D	N/D	N/D	65.1	64.8	63.9	N/D

Table 4.3 Efficiency calculation and comparison for both housings near surge

		Average η [%] – near surge		
		E – 78.09 g/s	**H – 72.42 g/s**	**Δ**
	η experimental data	65.50	62.02	**3.48**
Steady state	**η single blade model (s-SP-d)**	66.75	64.14	**2.61**
Steady state	**η full wheel model (s-FW-d)**	66.80	64.40	**2.40**
Unsteady	**η full wheel model, constant mass flow (u-FW-d)**	N=5: 65.4 N=10: 65.4 **N=20: 65.0**	N=5: 62.8 N=10: 62.6 **N=20: 62.8**	N=5: 2.6 N=10:2.8 **N=20: 2.2**
Unsteady	**η full wheel model, throttle b.c. (u-FW-d-p)**	N=5: 65.18 N=10: 64.86 **N=20: 64.03**	N=5: 62.50 N=10: 62.28 **N=20: 62.10**	N=5: 2.68 N=10: 2.58 **N=20: 1.93**
Unsteady	**η full wheel model, throttle b.c. (u-FW-d-p) (Alternative method)**	N=5: 66.85 **N=20: 65.91**	N=5: 64.27 **N=20: 64.02**	N=5: 2.58 **N=20: 1.89**

In terms of the influence of the time step parameter, an observation of the data in Figure 4.1 (constant mass flow exit boundary conditions) indicates that this parameter does have a small but noticeable effect on the results, namely in terms of the time period and amplitude of the oscillation. The effect is particularly more noticeable for the H-housing. In Figure 4.3, the N=5 simulation achieves almost flat convergence whereas those with N=10 and N=20 with both high frequency oscillations with a discernable low-amplitude frequency oscillation. As such, it can be inferred that a very low N value (N=5) fails to capture all of the unsteady phenomena. However, the effect of N on the time-averaged adiabatic efficiency is more mitigated. Table 4.3 indicates that this value varies very little with N, being less than 0.4 percentage point between N=5 and N=20 in the E-housing with a mass flow exit boundary condition.

The influence of the throttle boundary condition is mainly to slightly amplify the effect of the time step parameter. This is most apparent in the H-housing where a comparison of Figure 4.4 with Figure 4.3 show that the amplitude of the low-frequency oscillations in efficiency for the higher N values is higher with the throttle boundary conditions. Moreover, the throttle boundary condition also capture the high-frequency oscillations for the N=5 case, which was not the case for the mass flow boundary condition. In terms of the time-averaged efficiency, Table 4.3 indicates that its change with the time step parameter is also amplified with the throttle boundary conditions. For the E-housing, the change in time-averaged efficiency from N=5 to N=10 goes

from 0.4 points with mass low boundary condition to 1.15 points with the throttle boundary condition. Thus, simulations for the E-housing with the throttle boundary condition are used to determine the optimum time step setting. Figure 4.5 plots the variation of time-averaged adiabatic efficiency versus N for this configuration. The results indicate that the efficiency starts to asymptote at N=20 making this the recommended value for unsteady simulations.

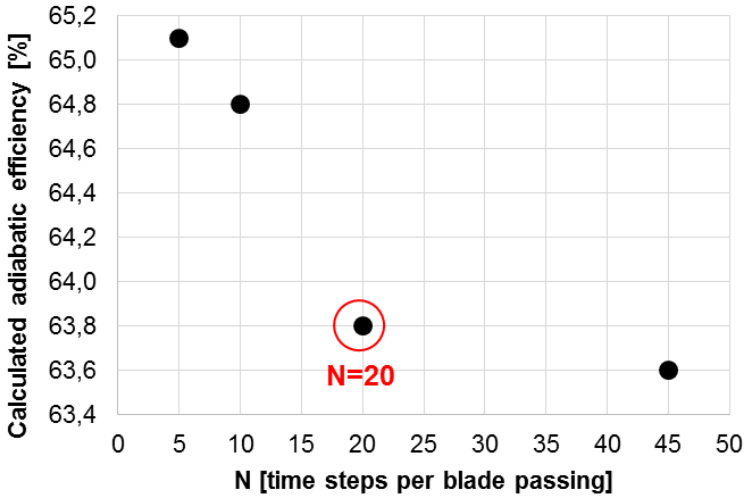

Figure 4.5 Time step study for the E-housing simulation with throttle b.c. (u-E-FW-78-N-d)

In terms of the comparison with test data, the results in Table 4.3 indicate that the unsteady simulations give a lower value of adiabatic efficiency than the steady-state simulations making the prediction much closer to the test values. In fact, for the E-housing, the unsteady simulations even underestimated the efficiency. As was the case for the steady-state simulations, the alternative calculation method increases the efficiency value by 1.5 to 2 percentage points. With regard to the difference in efficiency between the two housings, the unsteady simulations fail to close the gap between the steady-state predictions (about 2.5 points) and the test data (3.48 points), regardless of the time step value, exit boundary condition or even the use of the alternative method of efficiency calculation. (In fact, the relatively higher sensitivity of the efficiency to N for the E-housing even widens this gap for the higher N value.)

At 90 g/s Mass Flow

The equivalent data to Figure 4.1 to Figure 4.4 and Table 4.3 at a mass flow of 90 g/s are shown in Figure 4.6 to Figure 4.9 and Table 4.4. It is noted that the parametric study in terms of the N parameter was only carried out with the throttle boundary condition due to constraints in time and computational resources. The comparison of Figure 4.6 to Figure 4.9 with Figure 4.1 to Figure 4.4 leads to an immediate observation. In the case of the E-housing, the amplitude of the oscillations in efficiency at 90 g/s is reduced compared to the near-surge condition, as one would expect as the operating point moves away from the surge point (i.e more stable). On the other hand, the amplitude of the oscillations in efficiency has significantly increased for the H-housing to be on the same order of magnitude at that of the E-housing with the 90 g/s mass flow. This unexpected increase unsteadiness of the H-housing at a supposedly more stable operating point makes it more sensitive to the N parameter than was the case at near-surge. This is evident in Table 4.4, when the time-averaged efficiency varies more from N=5 to N=10 for the H-housing than for the E-housing, which is the opposite case to the near-surge condition (Table 4.3). As for the effect of the throttle, a comparison of the N=10 case between mass flow and throttle exit boundary condition indicate only a negligible effect on time-averaged efficiency (about 0.05 points).

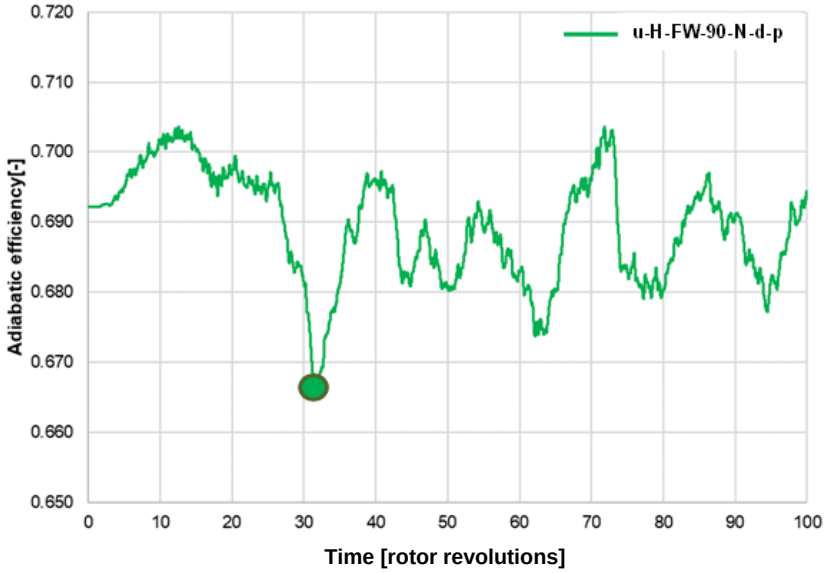

Figure 4.6 Unsteady convergence time history of adiabatic efficiency for **E-housing at 90 g/s**, short duct model with **exit mass flow b.c.** (u-E-FW-90-10-d)

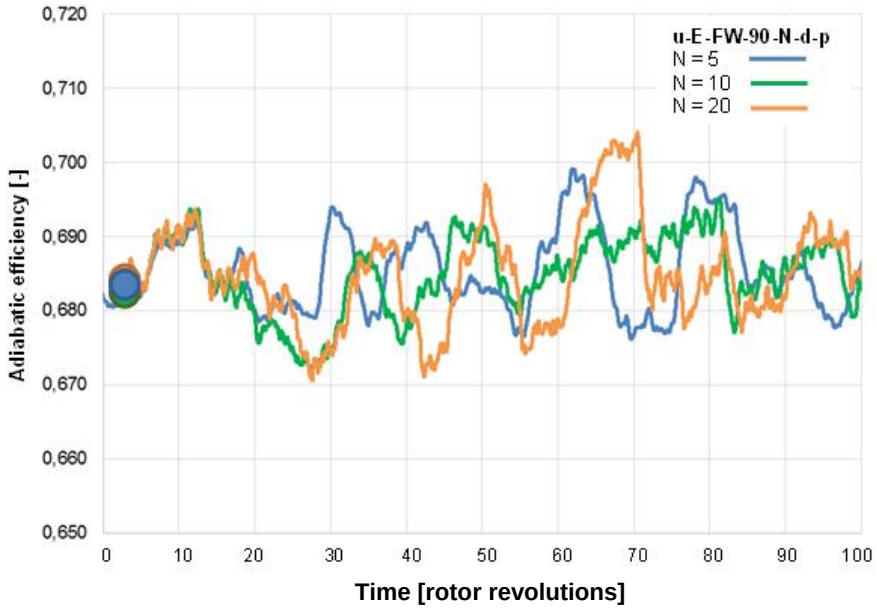

Figure 4.7 Unsteady convergence time history of adiabatic efficiency for **E-housing** at **90 g/s**, short duct model with **throttle b.c.** (u-E-FW-90-N-d)

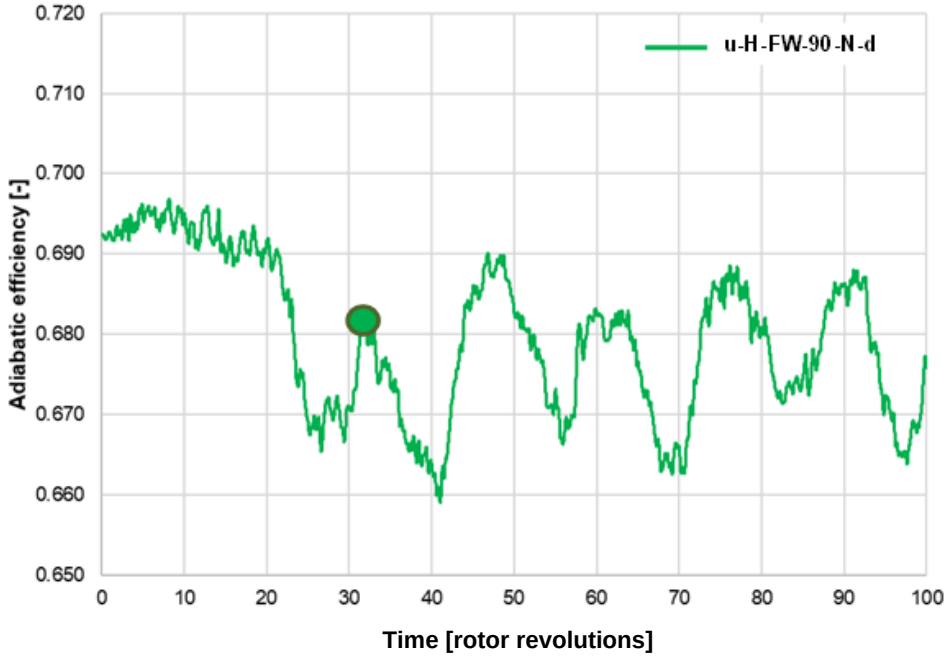

Figure 4.8 Unsteady convergence time history of adiabatic efficiency for **H-housing at 90 g/s**, short duct model with **exit mass flow b.c.** (u-H-FW-90-10-d)

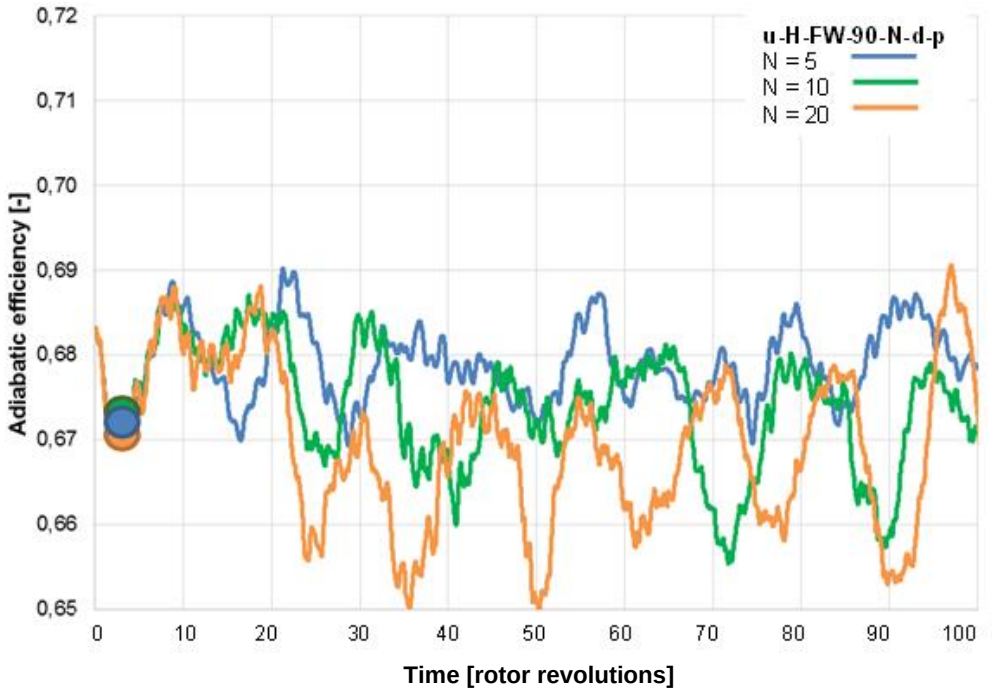

Figure 4.9 Unsteady convergence time history of adiabatic efficiency for **H-housing at 90 g/s**, short duct model with **throttle b.c.** (u-H-FW-90-N-d-p)

Table 4.4 Efficiency calculation & comparison for both housings at 90 g/s mass flow

		Average η [%] – m = 90 g/s		
		E-housing	**H-housing**	**Δ**
	η experimental data	67.40	65.40	**2.00**
Steady state	**η single blade model (s-SP-90-d)**	69.04	68.51	**0.53**
	η full wheel model (s-FW-90-d)	69.21	68.69	**0.52**
Unsteady	**η full wheel, cst. mass flow (u-FW-90-d)**	N=10: 68.7	N=10: 67.8	**N=10: 0.9**
	η full wheel model, throttle b.c. (u-FW-90-d-p)	N=5: 69.01 N=10: 68.81 **N=20: 68.83**	N=5: 68.35 N=10: 67.75 **N=20: 67.52**	N=5: 0.66 N=10: 1.06 **N=20: 1.31**
	η full wheel model, throttle b.c. (u-FW-90-d-p) (Alternative method)	N=5: 70.88 **N=20: 71.05**	N=5: 70.36 **N=20: 68.81**	N=5: 0.52 **N=20: 2.24**

As for comparison with test data, the results in Table 4.4 indicate that the unsteady simulation also predicts a lower adiabatic efficiency that the steady-state simulation, bring the prediction closer to the test value. However, the effect is less dramatic than it was the case near surge. As for the difference in efficiency between the two housings, the unsteady simulations help to

partially narrow the gap between the steady-state (0.52 point) simulations and the test data (2.00 points), especially for the higher N values, but the gap remains significant.

4.2.2 Effect of outlet duct length and plenum size

The time variation of adiabatic efficiency and mass flow for the E-housing simulations with the configurations shown in Figure 3.8 are plotted in Appendix G (Section G.1). Three observations can be reached from the results. First, the amplitude and time period of the main efficiency oscillation increase with a longer outlet duct (Figure 3.8 b and c). Second, while the use of a plenum model for the outlet duct (Figure 3.8 b) seems to capture similar amplitude of the main efficiency oscillation as that of the configuration that incorporated the outlet duct (Figure 3.8 c), it differs in main oscillation frequency and significantly overestimates the amplitude of the mass flow oscillations. Last but not least, the results for the configuration with an excessively large plenum (Figure 3.8 d) show that the throttle boundary condition can capture surge.

4.3 Summary

The main observations derived from the steady-state and unsteady simulations of the E and H-housings simulations can summarized in terms of the first objective of the project as follows:

1. Unsteady simulations bring the absolute efficiency values closer to what is experimentally observed on the compressor test stand and are thus better suited for predicting absolute efficiency values than steady-state simulations.
2. Unsteady simulations do not provide any improvement in capturing the measured difference in adiabatic efficiency between the two housings near surge over single blade passage steady-state simulations.
3. Unsteady simulations with a constant mass flow exit boundary condition is sufficient to capture the main efficiency oscillation frequency and amplitude and its time-average value, while a throttle exit boundary condition is better for capturing all of the oscillation frequencies.
4. A time step setting of 20 time steps per blade passing seems to be the optimum value for unsteady simulations, especially when using the throttle boundary conditions.

5. Experimental method of calculating adiabatic efficiency may overestimate its value by 1.5 to 2.0 percentage points.
6. The length of the outlet duct affects the frequency and amplitude of the oscillation in adiabatic efficiency and the modelling of this duct length affects the mass flow oscillation amplitude.

CHAPTER 5 RESULTS – FLOW FIELD ANALYSIS

This chapter investigates the flow unsteadiness observed from the unsteady simulations in Chapter 4 in order to find its source and possibly explain the unusual behaviour of the H-housing. The results in Chapter 4 showed that a smaller time step (larger N) and throttle boundary conditions allow for the capture of more unsteady frequencies. As a result, the analysis in this chapter is focused on the unsteady simulations near surge for both housings with N=20 and a throttle boundary condition.

5.1 Assessment of Unsteadiness

The first step of the analysis is to try to identify the location from which originates the high-amplitude unsteady component of efficiency variation. To this end, numerical static pressure probes are inserted at strategic locations in the housing and the unsteady simulations continued over a period of time that encompasses at least one period of the lowest frequency detected in the time convergence history of the efficiency to record the pressure signal at these locations. An FFT analysis is performed over the recording intervals of the time variation of adiabatic efficiency, as well as outlet mass flow, and the static pressure signals from numerical probes, as shown in Figure 5.2 and Figure 5.3. The signals were extracted by using MATLAB'S built-in FFT function with its default settings. The location(s) where the dominating (highest amplitude) frequency of the pressure signal is the same of as that of the adiabatic efficiency should be focused on to elucidate the source of the efficiency oscillations.

Figure 5.1 shows the location of the numerical probes for the E-housing (with probes at the same location in the H-housing). Probes are placed circumferentially at the diffuser inlet (impeller exit), volute inlet (diffuser outlet), near the tongue and in the outlet duct just downstream of the tongue. Figure 5.2 and Figure 5.3 show, respectively for the E and H-housings, the recorded efficiency, mass flow and static signals (of a set of representative probe labelled in Figure 5.1) on which the FFT analysis is performed. It is noted that due to the very low amplitude of the low-frequency oscillations and time constraints, the signals for the H-housing were not record over a long enough time interval to capture this frequency.

Table 5.1 lists the results from the FFT analysis. For the E-housing, the dominating (highest amplitude) frequency at each location is highlighted in larger bold characters. The results show

that for the E-housing, the dominant frequency (87.5 Hz) of the efficiency oscillation and outlet mass flow oscillation is also dominant in terms of pressure signal from the diffuser exit to the outlet duct. However, at the diffuser inlet (impeller exit), this frequency is no longer dominant. Instead, the amplitude of this frequency is sandwiched between the dominant frequency (262.5 Hz) is dominant and a frequency (1137-1575 Hz) associated with rotating stall as its period correspond to about three rotor revolutions (range of rotational speed of rotating stall cells). For the H-housing, since frequencies with a period higher than seven revolutions are not captured due to the recording intervals of the probe, the dominant frequency (1449 Hz) obtained from the FFT is that associated with rotating stall.

In summary, the results indicated that while rotating stall is present in both housings, the frequency associated with the large-amplitude efficiency oscillation in the E-housing seems to start at the diffuser outlet region and propagate downstream.

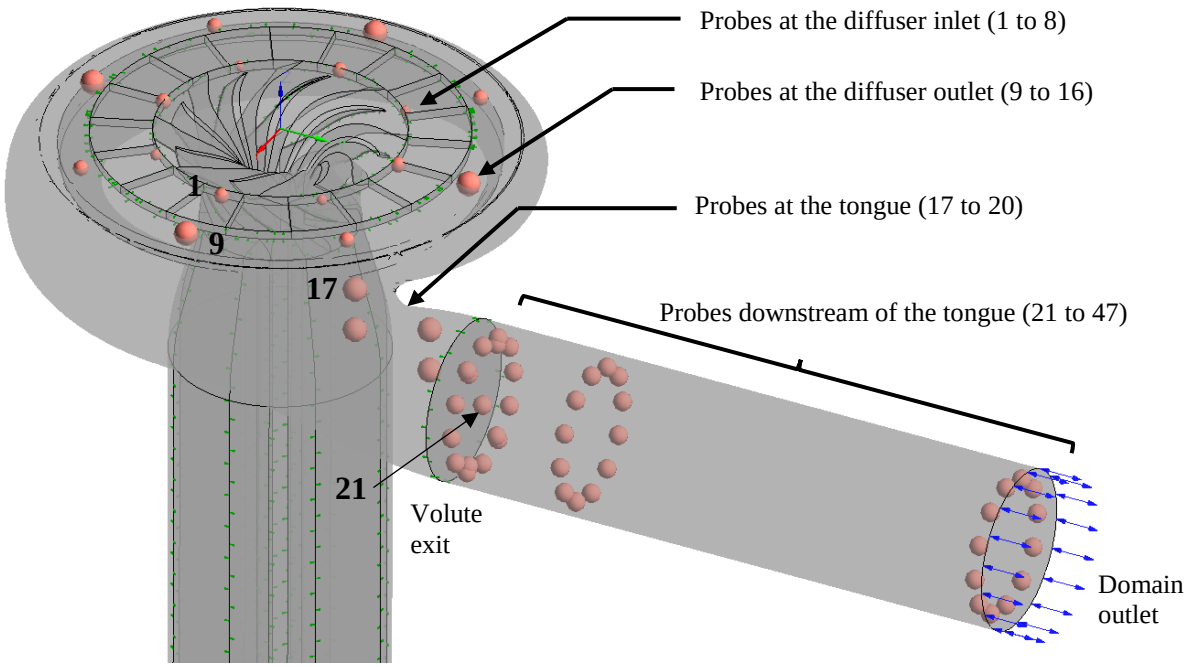

Figure 5.1 Static probes location in the E and H-housings for data analysis purposes

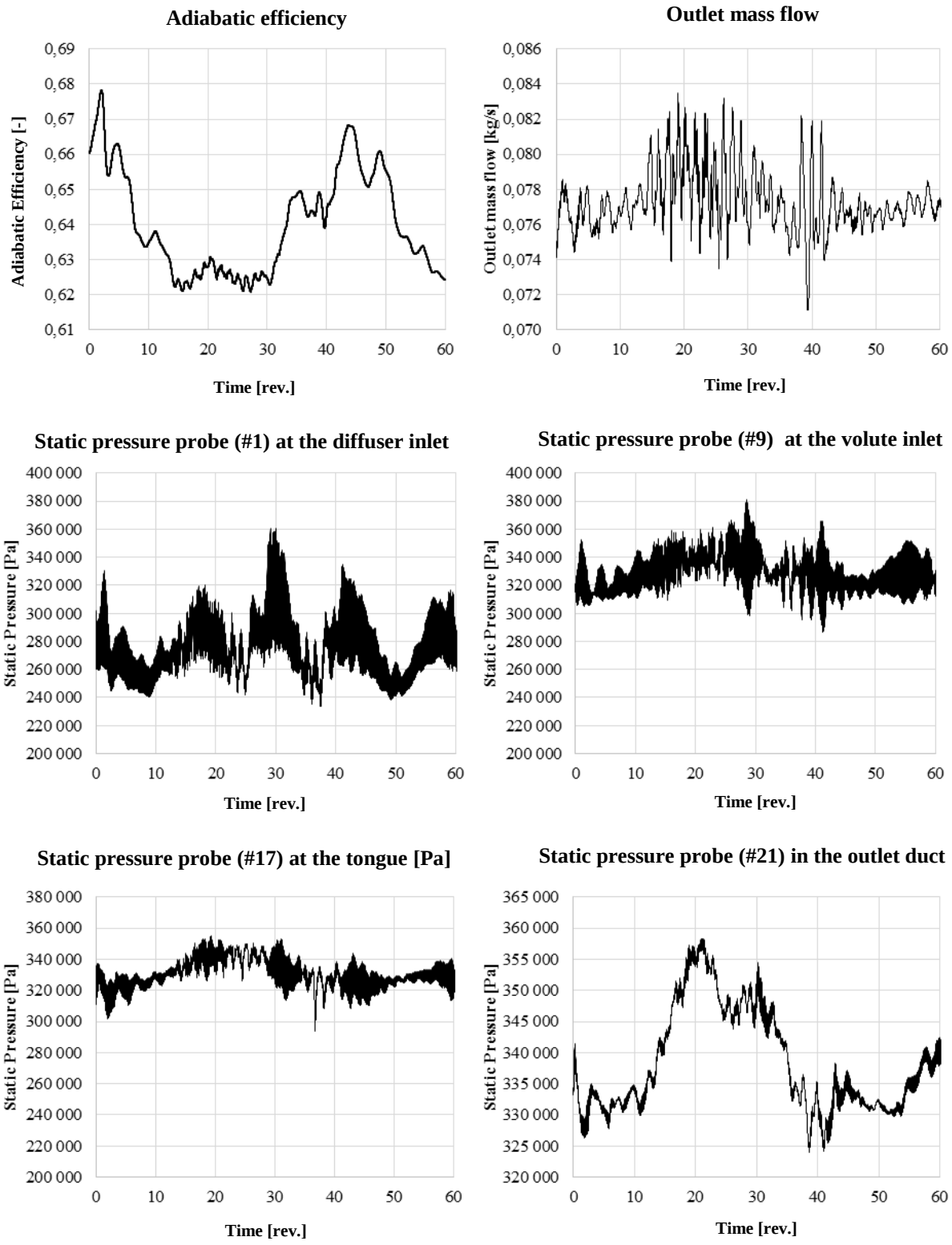

Figure 5.2 Time-varying signals of E-housing near surge (u-E-FW-78-20-d-p) for FFT analysis

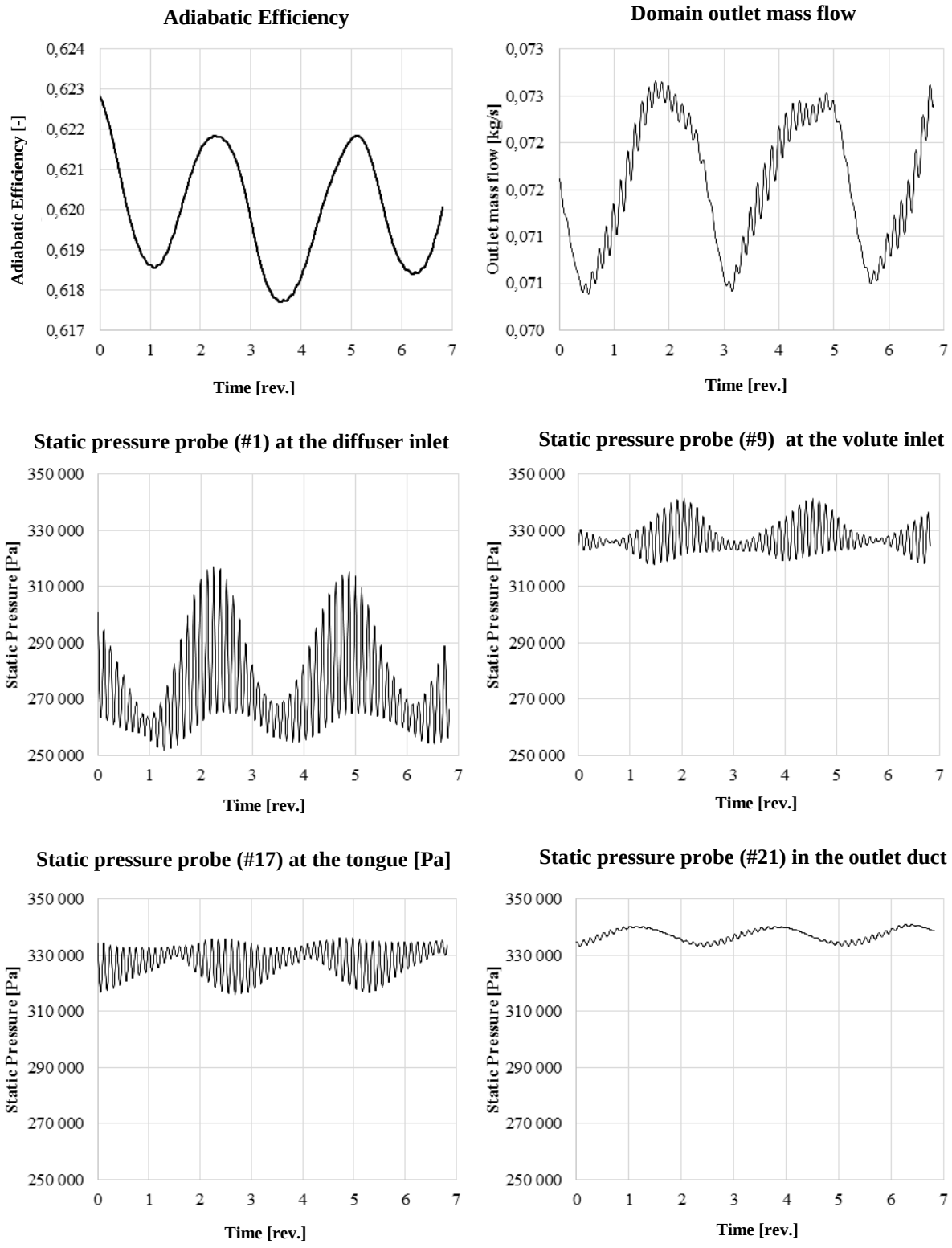

Figure 5.3 Time-varying signals of H-housing near surge (u-H-FW-78-20-d-p) for FFT analysis

Table 5.1 FFT results for the E-housing and H-housing near surge

E-housing, m = 78 g/s (u-E-FW-78-20-d-p)			**H-housing, m = 72 g/s (u-H-FW-72-20-d-p)**		
Adiabatic efficiency [-]					
Frequency [Hz]	**Period [rev.]**	**Amplitude**	**Frequency [Hz]**	**Period [rev.]**	**Amplitude**
87.5	**42**	**0.0170**	725	5.1	0.0005
175	21	0.0050	**1,449**	**2.5**	**0.0019**
350	10	0.0040			
787	4.7	0.0020			
1,400	2.6	0.0009			

Domain outlet mass flow [kg/s]					
Frequency [Hz]	**Period [rev.]**	**Amplitude**	**Frequency [Hz]**	**Period [rev.]**	**Amplitude**
87.5	**42**	**0.0013**	725	5.1	0.00009
262.5	14	0.0003	**1,449**	**2.5**	**0.00095**
1,225	3	0.0005	28,980	0.13	0.00008
2,450	1.5	0.0010			

Static pressure probe (#1) at the diffuser inlet [Pa]					
Frequency [Hz]	**Period [rev.]**	**Amplitude**	**Frequency [Hz]**	**Period [rev.]**	**Amplitude**
87.5	42	9,107	725	5.1	1,968
262.5	**14**	**15,590**	**1,449**	**2.5**	**12,440**
1,137	3.2	2,815	28,980	0.13	9,530
29,310	0.125	14,170			

Static pressure probe (#9) at the volute inlet					
Frequency [Hz]	**Period [rev.]**	**Amplitude**	**Frequency [Hz]**	**Period [rev.]**	**Amplitude**
87.5	**42**	**11,730**	725	5.1	392.1
262.5	14	3,520	**1,449**	**2.5**	**2,821**
1,575	2.4	964	28,980	0.13	3,361
29,050	0.125	449			

Static pressure probe (#17) at the tongue [Pa]					
Frequency [Hz]	**Period [rev.]**	**Amplitude**	**Frequency [Hz]**	**Period [rev.]**	**Amplitude**
87.5	**42**	**10,420**	725	5.1	370.3
175	21	1,443	1,449	2.5	2,943
1,225	3	1,355	**29,700**	**0.12**	**3,688**
2,625	1.4	2,071			
29,310	0.125	2,667			

Static pressure probe (#21) in the outlet duct [Pa]					
Frequency [Hz]	**Period [rev.]**	**Amplitude**	**Frequency [Hz]**	**Period [rev.]**	**Amplitude**
87.5	**42**	**10,640**	725	5.1	315.9
262.5	14	2,199	**1,449**	**2.5**	**3,027**
1,137	3.2	1,211	28,250	0.13	298.5
2,100	1.8	2,354			
29,310	0.125	8,607			

5.2 Source of Unsteadiness

Based on the FFT results in section 5.1, the search for the source of the unsteadiness starts with the flow structures in the diffuser at the exit of which the frequency associated with the large oscillation in the efficiency in the E-housing starts to become dominant. The flow structures in the volute can then be investigated.

5.2.1 Diffuser Flow Structures

Figure 5.4 plots the Mach number contours along with the flow vectors (coloured according to velocity magnitude) at the diffuser mid-span for the E-housing at different time instants, as marked in the corresponding time evolution of the adiabatic efficiency. Figure 5.5 shows the equivalent plots for the H-housing. For both housings, one can see that the there is a cell of circumferential flow non-uniformity rotating at part speed and which affects the flow uniformity at the exit of the diffuser. This is rotating stall and it is caused by flow reversal (radially inward flow) near the diffuser hub as illustrated in Figure 5.6 by the radial velocity profiles for the E-housing.

According to Figure 5.4, the rotating cell has two lobes and it takes approximately five to six rotor revolutions for the rotating cell to come back at its initial position (points 1 through 5), resulting in a period of about three rotor revolutions, which is consistent with the FFT result for rotating stall frequency. For the H-housing, Figure 5.5 indicates that the stall cell does not have a clear bi-lobed structure and takes 2.5 rotor revolutions to come back to the original state (points 1 through 5) giving the FFT predicted period of 2.5 rotor revolutions.

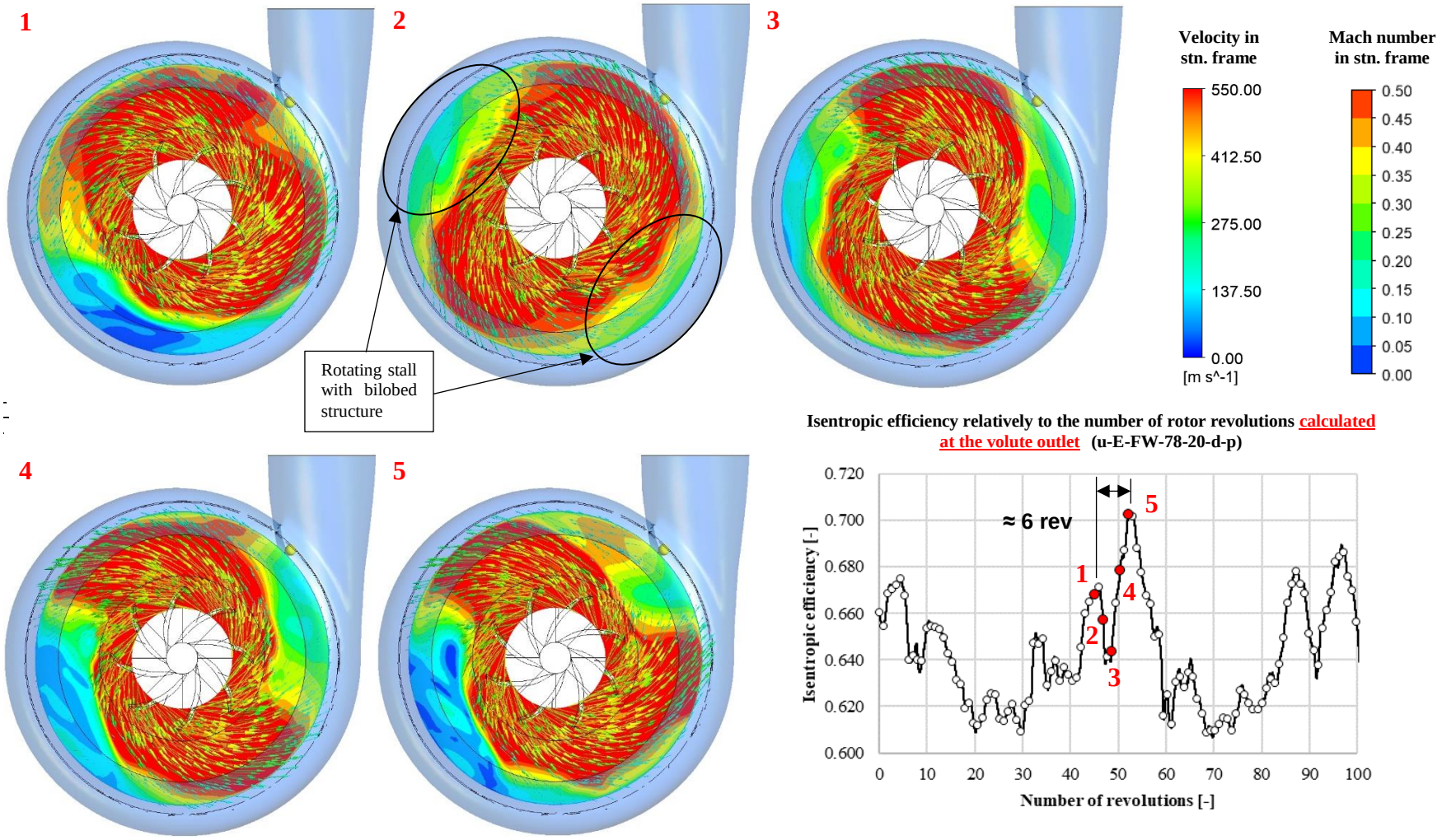

Figure 5.4 E-housing diffuser mid-span flow structures near surge (u-E-FW-78-20-d-p)

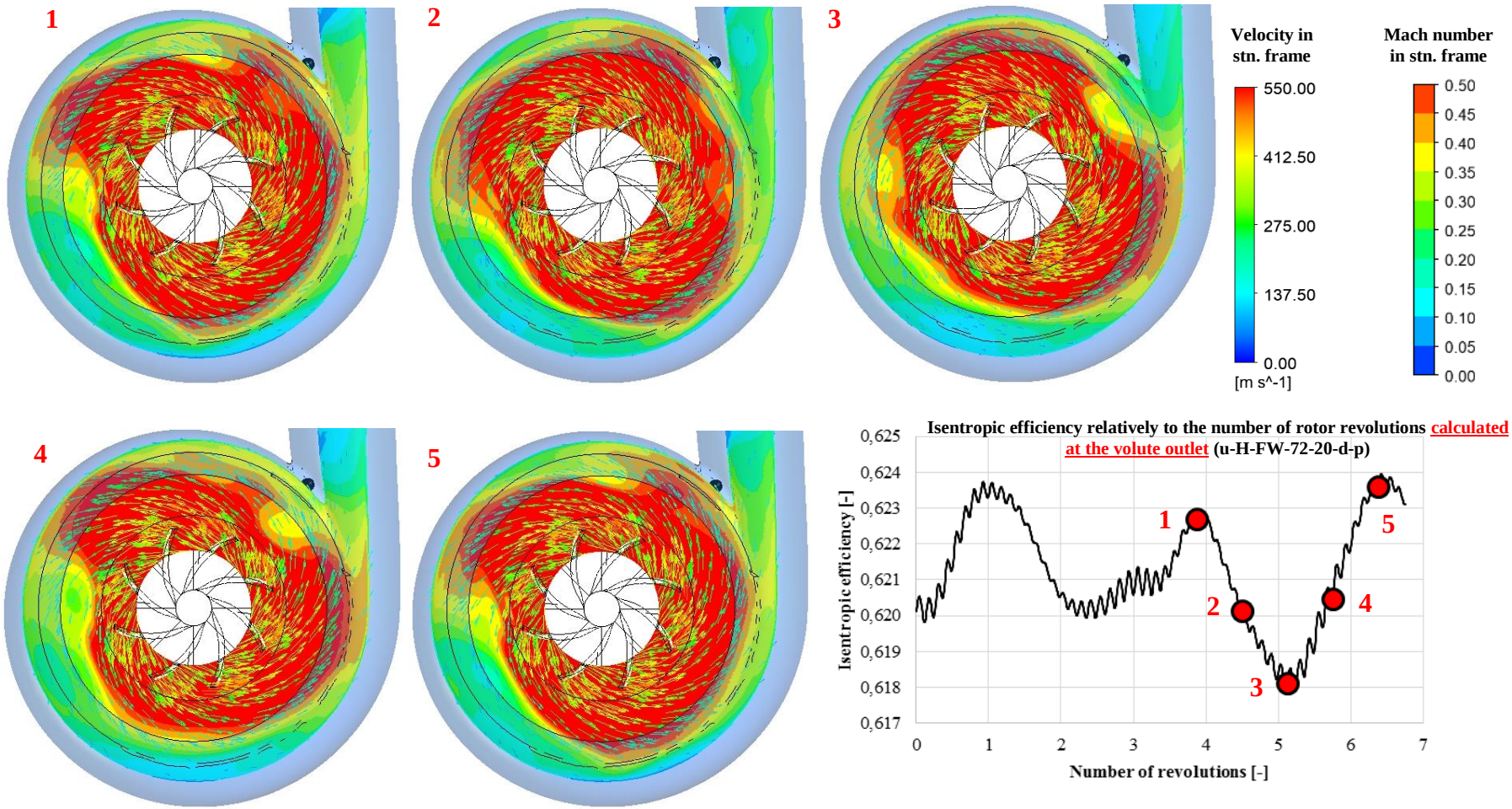

Figure 5.5 H-housing diffuser mid-span flow structures near surge (u-H-FW-72-20-d-p)

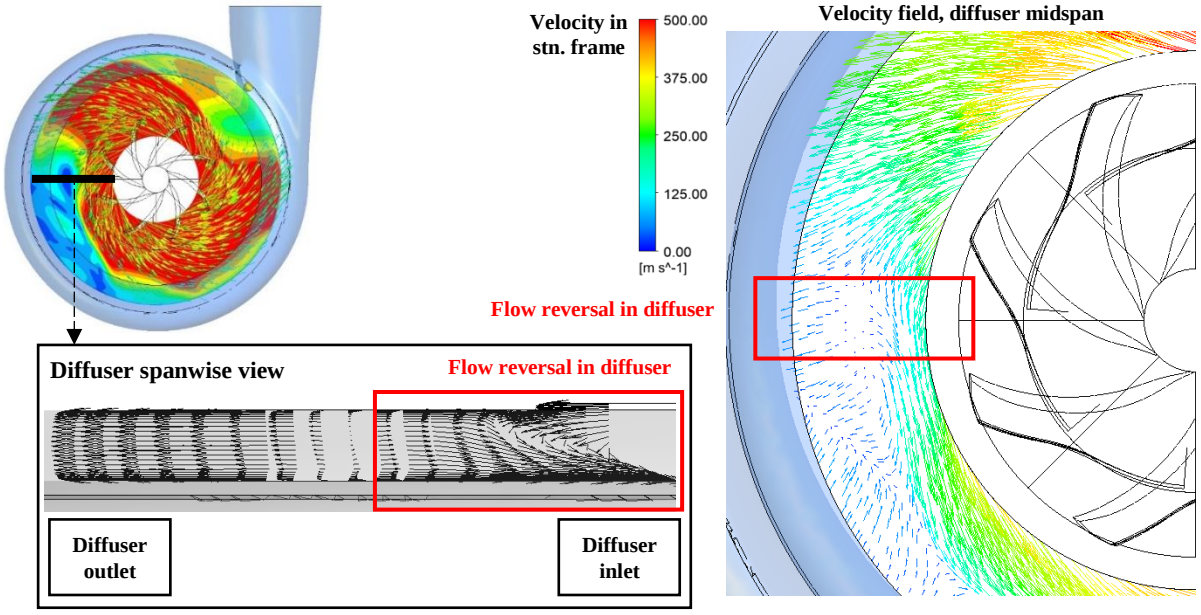

Figure 5.6 Flow cross-sections in E-housing diffuser near surge (u-E-FW-78-20-d-p)

5.2.2 Flow in the Volute

The results as observed in section 5.2.1 indicated that the presence of rotating stall near surge causes the flow exiting the diffuser and entering the volute to be circumferentially non-uniform. An investigation into the resulting effect on the flow in the volute shows two entirely different flow response between the E-housing and H-housing. Figure 5.7 plots the streamlines (coloured according to velocity magnitude) in the volute emanating from the diffuser exit plane at two time instants as indicated on the time variation of adiabatic efficiency. The flow exiting the diffuser just upstream of the tongue at time 1 flows normally around the volute before exiting the volute. However, at time 2, the higher radial velocity of this flow (due to the flow non-uniformity from the rotating stall cell) causes it to spill directly into the volute exit duct just upstream of the tongue. Figure 5.8 displays the Mach number distribution in the scroll and outlet duct. This intermittent spillage behaviour shown in Figure 5.7 results in a pulsating low-velocity flow structure just downstream of the tongue as illustrated by the time-varying size of the low-Mach number (blue) region in the volute exit. This fluctuating flow structure correlates with the oscillations in adiabatic efficiency and exit mass flow. Figure 5.7 also shows that the spillage behavior corresponds to a drop in adiabatic efficiency, which concurs with the findings of Dilin

et al. [20] who reported that the passage of the diffuser flow directly to the outlet duct harms compressor efficiency.

On the other hand, Figure 5.9 and Figure 5.10, which are the equivalent of Figure 5.7 and Figure 5.8 for the H-housing, show that the rotating flow non-uniformity at the exit of the H-housing diffuser does not cause any significant intermittent flow spillage upstream of the tongue into the outlet duct (Figure 5.9). As such, Figure 5.10 indicates that the low Mach number (blue) region in the volute exit remains small and does not oscillate in size to any significant extent.

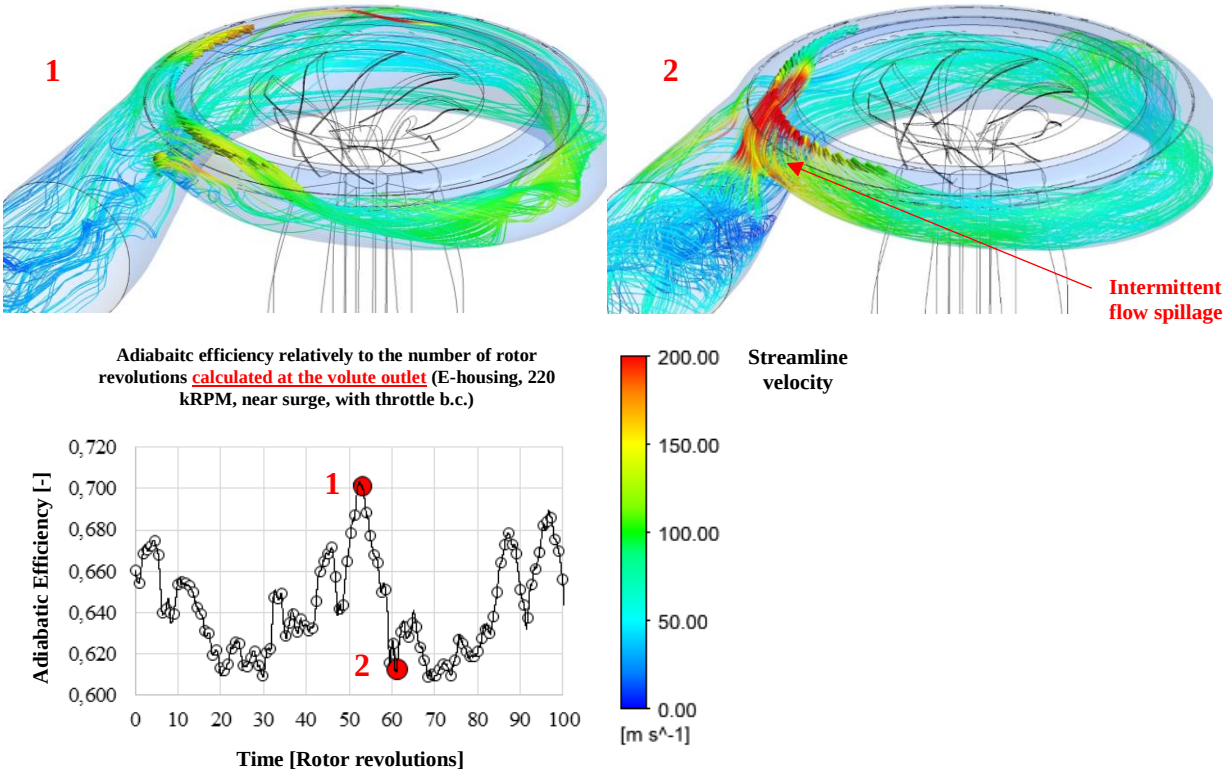

Figure 5.7 Streamlines out of a E-housing diffuser near surge (u-E-FW-78-20-d-p) at two time instants

From the above observations, it can be inferred that for the E-housing, the intermittent flow spillage in the volute exit is caused by the peak radial flow velocity (V_r) exiting the diffuser surpassing a critical value ($V_{r,cr}$) associated with the housing design, which does not occur for the H-housing near surge. This is illustrated in Figure 5.11 where the E-housing near surge would be represented by the green curve whereas the H-housing near surge would be represented by the

blue curve. For the H-housing, even though there is the rotating stall causing the radial velocity at the exit of the diffuser upstream of the tongue to fluctuate, the average radial velocity is low enough so that the peak velocity does not go above the threshold value.

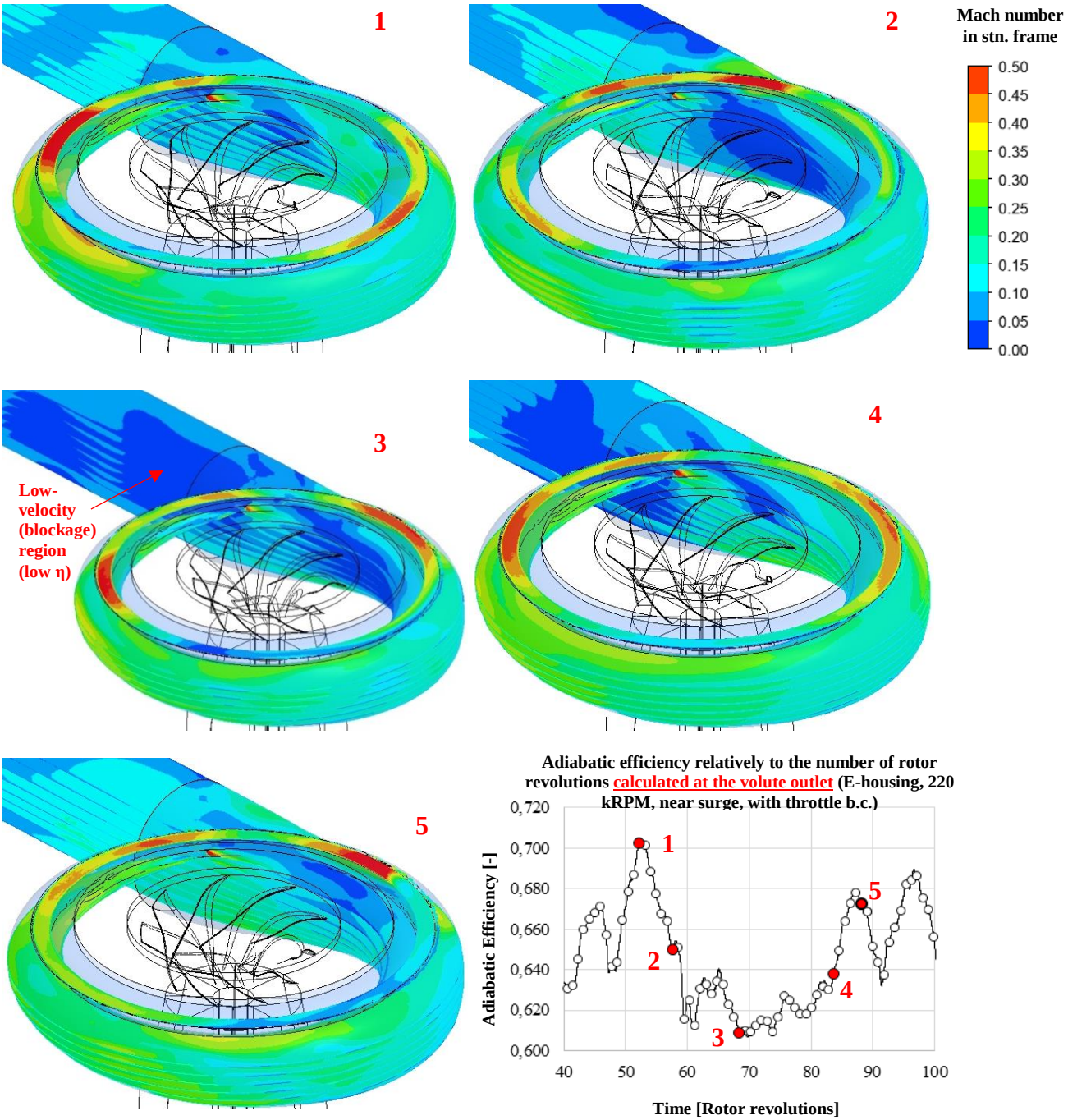

Figure 5.8 Mach number distribution in the volute and outlet duct for the E-housing near surge (u-E-FW-78-20-d-p) at different time instants

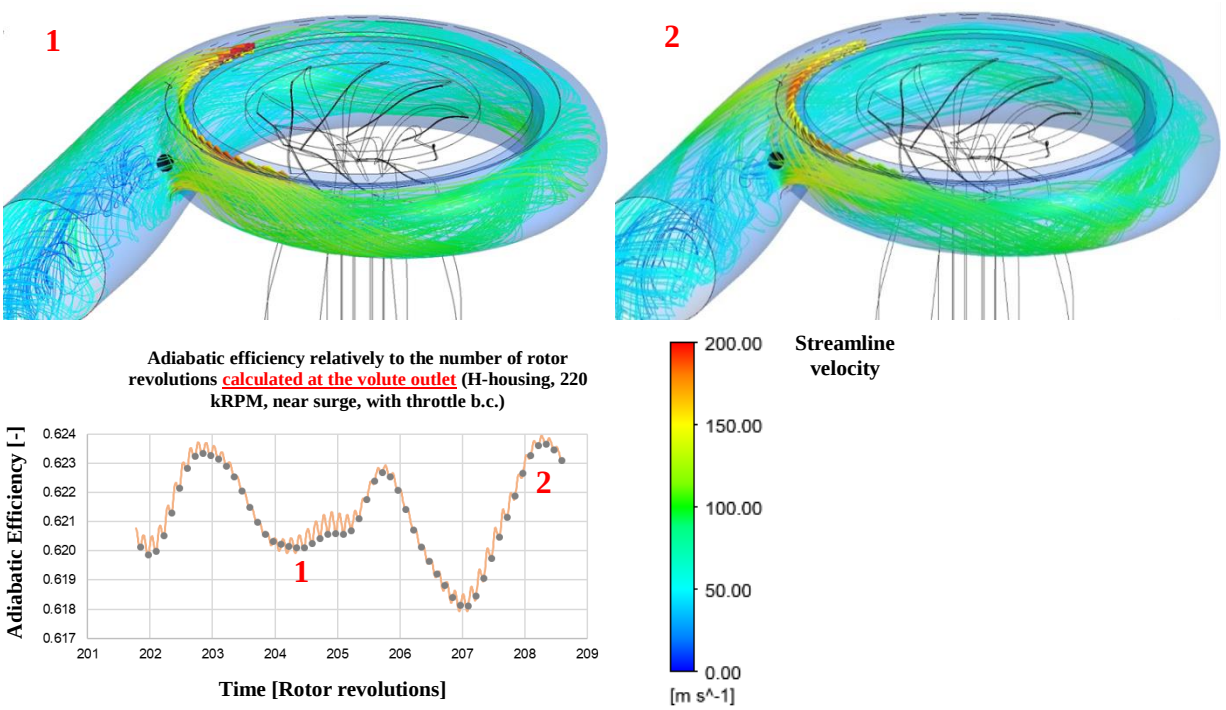

Figure 5.9 Streamlines out of a H-housing diffuser near surge (u-H-FW-72-20-d-p) at two time instants

However, if the mass flow increases and rotating stall remains, as is the case for the 90 g/s condition, the average radial velocity may increase to a point where the peak radial velocity goes beyond the threshold value and the situation represented by the red line in Figure 5.11 is reached resulting in intermittent flow spillage and fluctuation in the efficiency. This would explain why the H-housing experience significant adiabatic efficiency oscillation at 90 g/s but not at near surge (72 g/s). This intermittent flow spillage amplifies the effect of rotating stall on the oscillations of the adiabatic efficiency.

To verify this hypothesis, Figure 5.12 and Figure 5.13 plots the radial flow velocity at the diffuser exit upstream of the tongue (probe #9 on Figure 5.1) at different simulated mass flows for the E and H-housings, respectively. While the threshold radial velocity is unknown for each housing, we can estimate it to be the radial velocity value at the design mass flow.

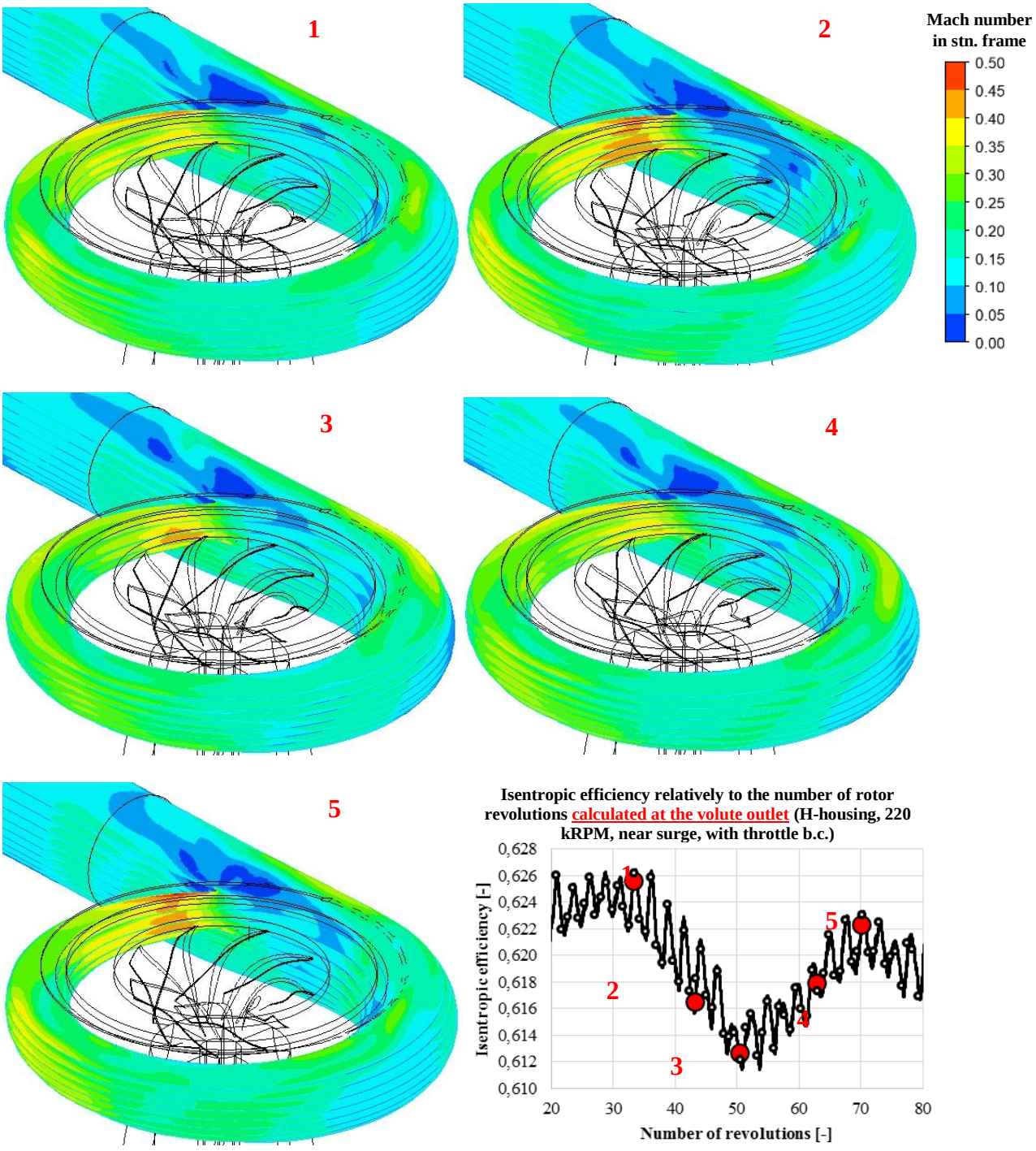

Figure 5.10 Mach number distribution in the volute and outlet duct for the H-housing near surge (u-H-FW-72-20-d-p) at different time instants

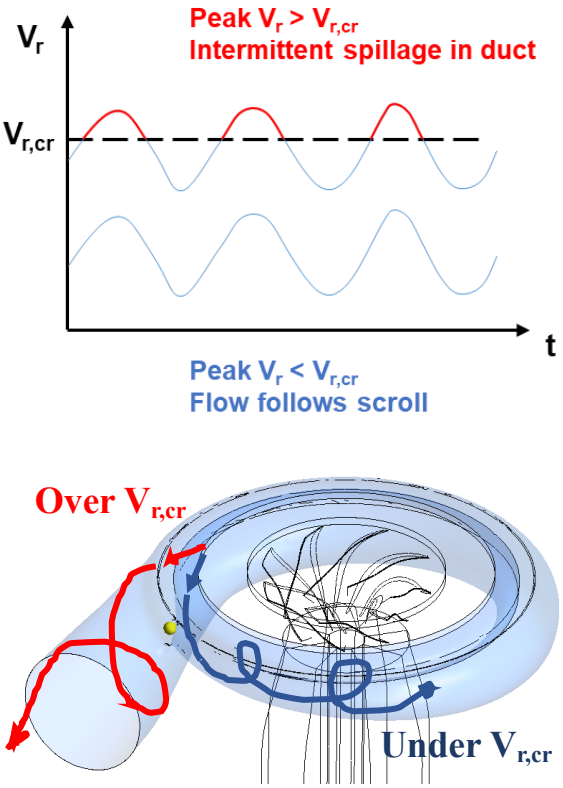

Figure 5.11 Critical radial velocity hypothesis

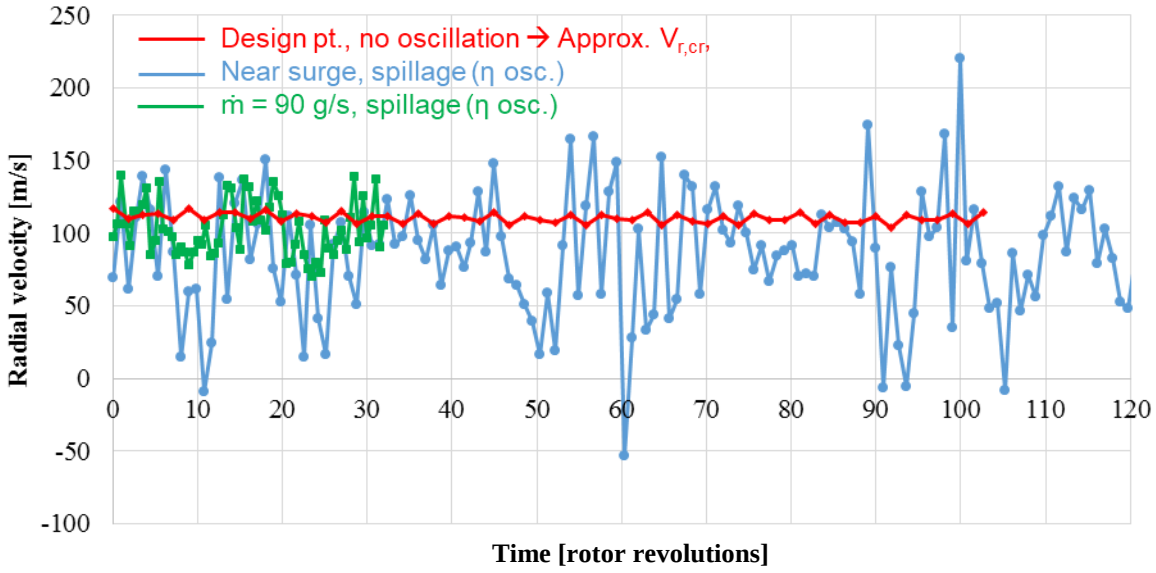

Figure 5.12 Radial velocities at diffuser exit upstream of tongue for E-housing

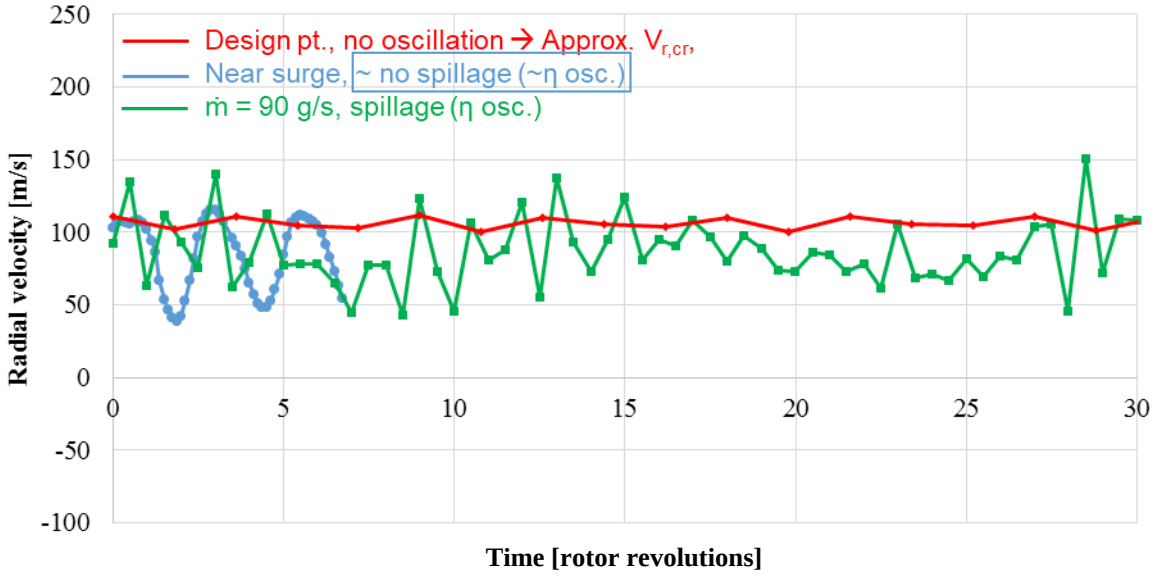

Figure 5.13 Radial velocities at diffuser exit upstream of tongue for H-housing

As such, this value represents the upper limit of the threshold radial velocity. In Figure 5.12, one can see that the radial flow velocity for the E-housing near surge does intermittently cross the estimated threshold (design point) value, surpassing it significantly at peak values. Furthermore, one can observe that the radial flow velocity amplitude is quite irregular due to the constantly varying shape of the stall cell as seen in Figure 5.4. As a result, the radial flow does not cross the threshold at the same frequency as rotating stall, which can explain the difference between the spillage frequency and the rotating stall frequency.

On the other hand, Figure 5.13 shows that it virtually does not cross the estimated threshold (design point) value at near surge but does cross it significantly at 90 g/s.

It must be noted that the design of the housing, especially the vaneless diffuser and its transition to the scroll (both of which differ between the E and H-housings), will affect the amplitude of the radial velocity fluctuation (due to its effect on the rotating stall pattern) at the diffuser exit, the average radial velocity at this location and the threshold radial velocity, all of which will change the unsteady flow behavior according to this model.

5.2.3 Effect of Rotating Stall

The model proposed in Section 5.2.2 seems to explain the observed presence or near-absence of large amplitude efficiency oscillations in the E and H housings at different mass flow values and point to rotating stall as playing a crucial role. To further solidify the hypothesis that rotating stall does play a crucial role in the efficiency oscillations, a comparison between the steady and unsteady simulations for the E-housing near surge is carried out.

Figure 5.14 plots the Mach number at the diffuser mid-span and Figure 5.15 the radial flow profile in the diffuser. Both show the absence of a rotating stall cell and radial flow reversal in the diffuser associated with such a cell. Figure 5.16 compares the time history of the adiabatic efficiency for the steady and unsteady simulations for the E-housing near surge. It shows that in the absence of rotating stall, there are no efficiency oscillations and the efficiency converges toward a stable value. This proves that the presence of rotating stall is a necessary (if not sufficient) condition for the observed flow unsteadiness.

An estimation of the effect of this unsteadiness on compressor efficiency is carried out in Appendix H.

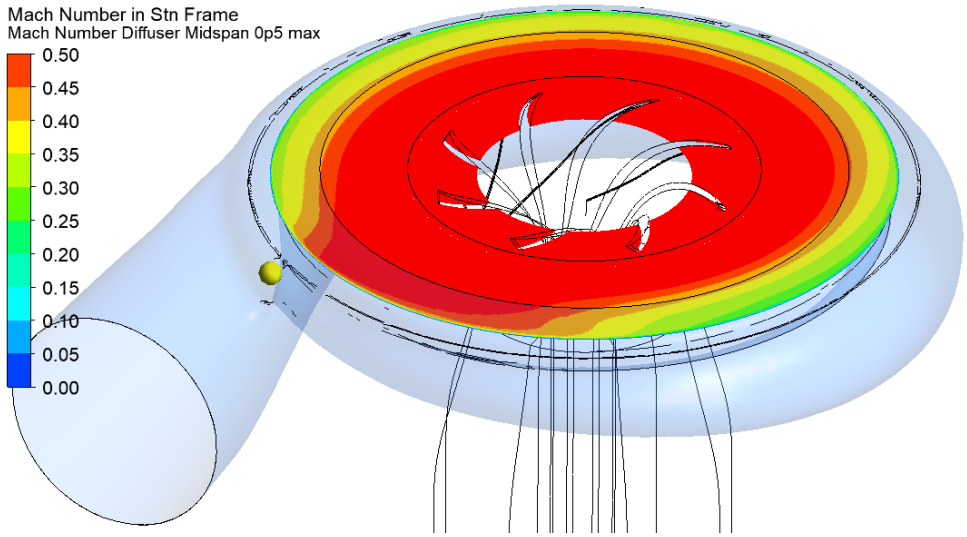

Figure 5.14 Mach number distribution at the diffuser mid-span for the E-housing near surge from steady-state simulations (s-E-FW-78-d)

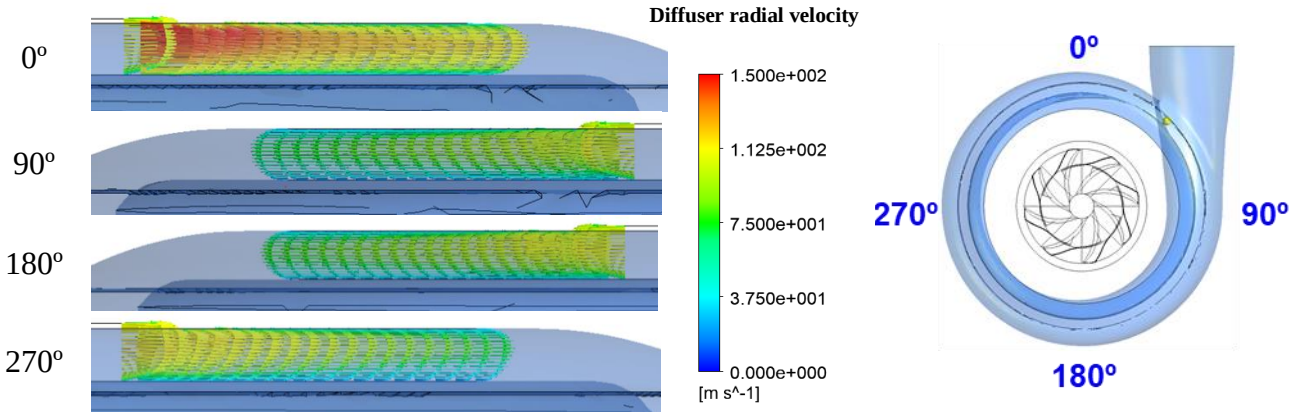

Figure 5.15 Flow cross-sections in E-housing diffuser near surge from steady-state simulations (s-E-FW-78-d)

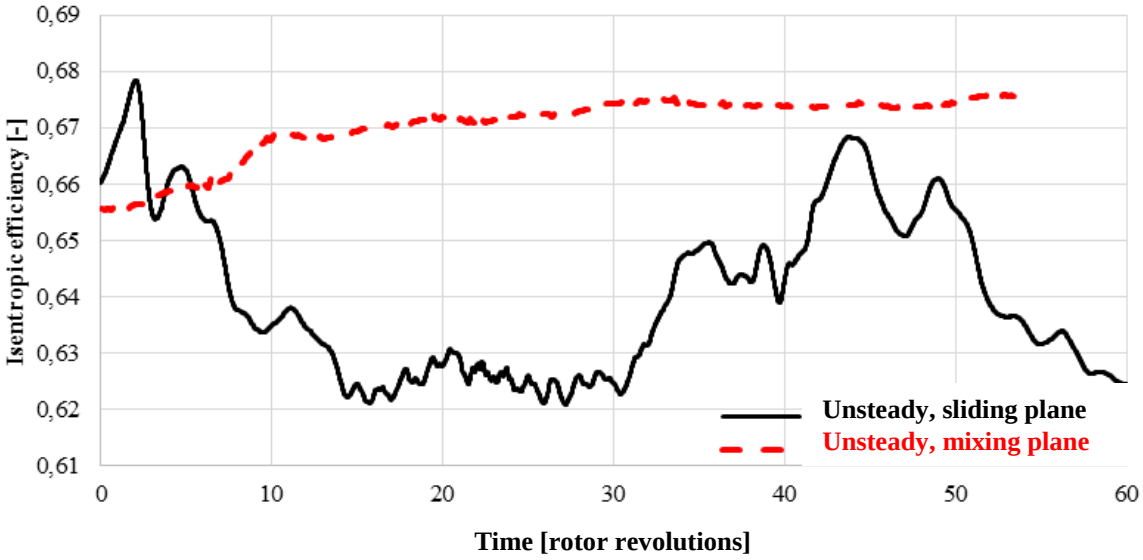

Figure 5.16 Time variation of adiabatic efficency for steady-state and unsteady simulations of E-housing near surge

5.3 Summary

The analysis of the unsteady flow simulations for the E and H-housing have led to a model to explain the source of the oscillations in adiabatic efficiency so prominent for the E-housing but almost absent for the H-housing near surge. This model states that:

- Rotating stall is a necessary but not sufficient condition for flow unsteadiness
- If the rotating circumferential flow uniformity at the exit of the diffuser due to rotating stall causes the radial flow velocity just upstream of the tongue to fluctuate and exceed intermittently a threshold value, the flow will spill intermittently into the outlet duct, resulting in a low-velocity flow structure of fluctuating size in the volute exit.

This fluctuating flow structure correlates with the oscillations in adiabatic efficiency and exit mass flow.

CHAPTER 6 CONCLUSION

6.1 Conclusions

The main conclusions from this study are:

1. Unsteady simulations give a better prediction of the absolute efficiency values relatively to the experimental results than steady-state simulations and give a good insight about the unsteady phenomena occurring in the compressor.
2. Single-passage steady simulations are sufficient to provide the efficiency difference between the two housings.
3. The recommended setup for unsteady simulations is the following:
    - Outlet constant mass flow boundary condition
    - Time steps equivalent to one twentieth ($1/20^{th}$) of a blade passing
4. The throttle boundary condition is useful for better capture of more unsteadiness frequencies.
5. The length of the outlet duct affects the frequency and amplitude of the oscillation in adiabatic efficiency and the modelling of this duct length affects the mass flow oscillation amplitude.
6. Rotating stall in the diffuser is at the source of the flow oscillations seen in the adiabatic efficiency. It is a necessary but not sufficient condition for high-amplitude oscillation in adiabatic efficiency.
7. High-amplitude oscillation in adiabatic efficiency occurs when the fluctuating radial flow velocity (due to rotating stall) exceed intermittently a threshold value to cause the diffuser exit flow just upstream of the tongue to spill intermittently into the outlet duct, resulting in a low-velocity flow structure of fluctuating size in the volute exit.

6.2 Recommendations for Future Work

Based on the findings of the current study, the following recommendations for future work can be formulated.

- Further investigate the effect of the duct length and the plenum volume on the predicted efficiency and mass flow oscillations amplitude and frequency.
- Validate experimentally the flow unsteadiness predicted by the CFD simulations. Dynamic pressure and temperature measurements should be performed on both housings at the simulated mass flows to see if the predicted oscillation frequencies and amplitudes are accurate and whether the peculiar behaviour of the H housing near surge is observed.
- Carry out more analysis to explain the difference in frequencies between rotating stall and the high-amplitude oscillation of the efficiency.
- Explore on ways to alter the housing design (to change the fluctuation and threshold value of radial velocity at the diffuser exit) to minimize the unsteady flow oscillations and perhaps improve performance.

REFERENCES

[1] H. W. Emmons, C. E. Pearson and H. P. Grant, "Compressor surge and stall propagation," *TRANS. ASME,* pp. 455-469, 1955.

[2] N. A. Cumpsty, Compressor aerodynamics, Krieger Publications, 2004.

[3] J. Sorokes, C. J. Borer and J. M. Koch, "Investigation of the circumferential static pressure non-uniformity caused by a centrifugal compressor discharge volute," in *International gas turbine and aeroengine congress and exhibition*, Stockholm, 1998.

[4] P. Frigne and R. Van den Braembussche, "Distinction between different types of impeller and diffuser rotating stall in a centrifgual compressor with vaneless diffuser," *Transactions of ASME,* pp. 468-474, April 1984.

[5] R. Dehner, A. Selamet, P. Keller and M. Becker, "Simulation of mild surge in a turbocharger compressor system," *SAE International,* pp. 197-212, October 2010.

[6] R. Dehner, A. Selamet, P. Keller and M. Becker, "Prediction of surge in a turbocharger compression system vs. measurements," *SAE International,* pp. 2181-2192, May 2011.

[7] A. X. Liu and X. Q. Zheng, "Methods of surge point judgment for compressor experiments," *Experimental Thermal and Fluid Science,* pp. 204-213, August 2013.

[8] D. Fink, N. A. Cumpsty and E. M. Greitzer, "Surge dynamics in a free-spool centrifugal compressor system," *Journal of Turbomachinery,* pp. 321-332, April 1992.

[9] X. Zheng and A. Liu, "Phenomenon and mechanism of two-regime-surge in a centrifugal compressor," *Journal of Turbomachinery,* pp. 1-7, August 2015.

[10] R. A. Van den Braembussche and B. M. Hände, "Experimental and theoretical study of the swirling flow in centrifugal compressor volutes," *Transactions of ASME,* pp. 38-43, 1990.

[11] E. Ayder, R. Van de Braembussche and J. J. Brasz, "Experimental and theoretical analysis of the flow in a centrifugal compressor volute," *Transactions of the ASME,* pp. 582-589, 1993.

[12] F. Gu and A. Engeda, "A numerical investigation on the volute/impeller steady-state interaction due to circumferential distortion," in *Proceedings of ASME Turbo Expo 2001*, New Orleans, 2001.

[13] S. Khalfallah and A. Ghenaiet, "Analyses of impeller-vaneless diffuser-scroll interactions in a radial compressor," *IMechE Power and Energy*, pp. 851-867, March 2010.

[14] S. Kim, J. Park, K. Ahn and J. Baek, "Improvement of the performance of a centrifugal compressor by modifying the volute inlet," *Journal of Fluids Engineering,* pp. 1-7, September 2010.

[15] L. Yu, W. Cousins, F. Shen, G. Kalitzin, V. Sishtla and O. Sharma, "Numerical investigation of the effect of diffuser and volute design parameters on the performance of a centrifugal compressor sstage," in *Proceedings of ASME Turbo Expo 2016*, Seoul, 2016.

[16] D. Hagelstein, R. Van den Braembussche, R. Keiper and M. Rautenberg, "Experimental investigation of the circumferential static pressure distortion in centrifugal compressor stages," in *International Gas Turbine and Aeroengine Congress and Exhibition*, Orlando, 1997.

[17] D. Hagelstein, K. Hillewaert, R. A. Van den Braembussche, A. Engeda, R. Keiper and M. Rautenberg, "Experimental and numerical investigation of the flow in a centrifugal compressor volute," *Transactions of ASME,* pp. 22-31, January 2000.

[18] S. Shaaban and J. Seume, "Aerodynamic performance of small turbocharger compressors," in *ASME Turbo Expo 2007*, Montréal, 2007.

[19] S. Chu, R. Dong and J. Katz, "Relationship between unsteady flow, pressure fluctuations, and noise in a centrifugal pump - Part B: Effects of blade-tongue interactions," *Transactions*

of ASME, pp. 30-35, March 1995.

[20] P. Dilin, T. Sakai, M. Wilson and A. Whitfield, "A computational and experimental evaluation of the performance of a centrifugal fan volute," *Proc Instn Mech Engrs,* pp. 235-246, 1998.

[21] D. Pan, A. Whitfield and M. Wilson, "Design considerations for the volutes of centrifugal fans and compressors," *Proc. Instn. Mech. Engrs.,* pp. 401-410, 1999.

[22] K. Wei, S. Zuo, H. He and Z. Wang, "Numerical study on the unsteady behavior of a centriugal compressor for the fuel-cell vehicle," in *Meetings on Acoustics*, Providence, 2015.

[23] C. Xu and M. Müller, "Development and design of a centrifugal compressor volute," *International Journal of Rotating Machinery,* pp. 190-196, 2005.

[24] F. Gu, A. Engeda, M. Cave and J.-L. Di Liberti, "A numerical investigation on the volute/diffuser interaction due to the axial distortion at the impeller exit," *Journal of Fluids Engineering,* pp. 475-483, September 2001.

[25] X. Zheng, A. Liu and Z. Sun, "Investigation of the instability mechanisms in a turbochrger centrifugal compressor with a vaneless diffuser by means of unsteady simulations," *Journal of Automobile Engineering,* pp. 1558-1567, 2017.

[26] Y. Bousquet, X. Carbonneau, G. Dufour, N. Binder and I. Trebinjac, "Analysis of the unsteady flow field in a centrifugal compressor from peak efficiency to near stall with full-annulus simulations," *International journal of rotating machinery,* pp. 1-11, 2014.

[27] Y. Bousquet, X. Carbonneau, I. Trebinjac, N. Binder and G. Dufour, "Numerical investigation of Kelvin-Helmholtz instability in a centrifugal compressor near stall," *Proceedings of ASME Turbo Expo 2015,* pp. 1-13, 2015.

[28] C. A. Amann, G. E. Nordenson and G. D. Skellenger, "Casing modification for increasing

the surge margin of a centrifugal compressor in an automotive turbine engine," *Journal of Engineering for Power,* pp. 329-335, 1975.

[29] J. Galindo, J. R. Serrano, H. Climent and A. Tiseira, "Experiments and modelling of surge in small centrifugal compressor for automotive engines," *Experimental Thermal and Fluid Science,* pp. 818-826, 2007.

[30] L. Dai, A. Engeda, M. Cave and J.-L. Di Liberti, "Numerical study and experimental validation of the performance of two different volutes with the same compressor impeller," *IMechE Power and Energy,* pp. 157-166, 2009.

[31] Z. Sun, X. Zheng, Z. Linghu, T. Kawakubo, H. Tamaki and B. Wang, "Influence of volute design on flow field distortion and flow stability of turbocharger centrifugal compressors," *Journal of Automotive Engineering,* pp. 1-11, 2018.

[32] Q. Guo, H. Chen, X. Zhu, Z.-H. Zhu and Y. Zhao, "Numerical simulations of stall inside a centrifugal compressor," *IMechE Power and Energy,* pp. 683-693, April 2007.

[33] S. H. Jeon, D. H. Hwang, J. H. Park, C. H. Kim, J. H. Baek and K. W. Him, "Numerical study on the effect of a volute on surge phenomena in a centrifugal compressor," in *ASME Turbo Expo 2016*, Seoul, 2016.

[34] A. Fatsis, S. Pierret and R. Van den Braembussche, "Three-dimensional unsteady flow and forces in centrifugal impellers with circumferential distortion of the outlet static pressure," *Transactions of ASME,* pp. 94-102, January 1997.

[35] M. Yang, X. Zheng, Y. Zhang, T. Bamba, H. Tamaki, J. Huenteler and Z. Li, "Stability improvement of high-pressure-ratio turbocharger centrifugal compressor by asymmetric flow control - Part 1: non-axisymmetrical flow in centrifugal compressor," *Journal of Turbomachinery,* pp. 1-9, March 2013.

[36] M. Dumas, H. D. Vo and H. Yu, "Post-surge load prediction for multi-stage compressors via

CFD simulations," in *Proceedings of ASME Turbo Expo 2015: Turbine Technical Conference and Exposition*, Montréal, 2015.

[37] E. M. Greitzer, "Surge and rotating stall in axial flow compressors," *Journal for Engineering for Power,* pp. 190-198, 1976.

APPENDIX A THROTTLE BOUNDARY CONDITION

This appendix provides more details on the throttle boundary condition used in the present work. This boundary condition was devised and implemented in ANSYS CFX by Dumas et al. [36] to simulate surge in multi-stage compressors. However, it had yet to be used on a turbocharger compressor with volute scroll. As illustrated in Figure A.1, the setup consists of coupling CFD simulation the compressor and analytical modelling of the downstream components, namely the exit plenum and throttle valve (which stand in for the combustor and turbine in an aero-engine), in the same manner as the modelling of these components by Greitzer [37]. This coupling takes the form a dynamic static pressure that is applied as a boundary condition to the compressor CFD domain outlet, with this pressure varying in time according to the analytical model of the plenum-valve assembly.

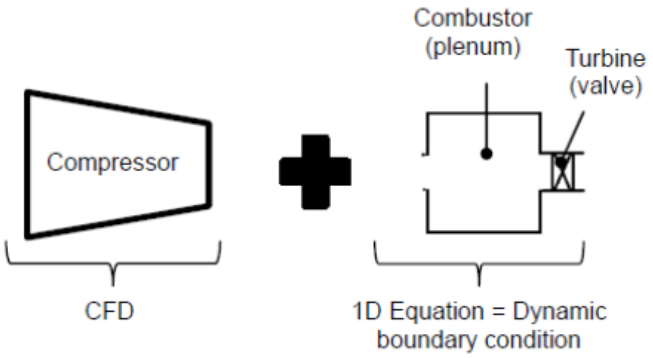

Figure A.1 Throttle boundary condition [36]

A.1 Explanation of the Model

The throttle boundary condition is based on modelling the air inside of the plenum as an ideal gas under isentropic compression and expansion, with its pressure (P) regulated the plenum inlet ($\dot{m}_{in}$) and outlet ($\dot{m}_{iout}$) mass flows as expressed by equations (A.1) where V_P is the plenum volume and a the speed of sound.

$$\frac{dP}{dt} = \frac{a^2}{V_P}\left(\dot{m}_{in} - \dot{m}_{out}\right) \tag{A.1}$$

Furthermore, the mass flow exiting the plenum to the atmosphere through the throttle valve is modeled to vary in a quadratic manner, with pressure drop across the valve, which translates to equation (A.2), where K_t is the throttle constant and v_m is the mean meridional velocity through the valve.

$$\Delta P_{valve} = 0.5\, K_t\, \rho\, v_m^2 \tag{A.2}$$

By supposing that the plenum pressure is the total pressure exiting the compressor and that the (atmospheric) pressure downstream of the valve is equal to the inlet total pressure to the compressor (which is a very close approximation for a turbojet as well as the current compressor test rig), equations (A.1) and (A.2) can be combined and discretized in time to give equation (A.3). It updates the static pressure at the CFD domain exit at every iteration according to the boundary conditions setup shown in Figure A.2 a when the mass flow is positive (forward flow). At the same time, the atmospheric pressure and temperatures are applied as total pressure and temperature at the CFD domain inlet. The *B* parameter in equation (A.3) is a similitude parameter defined by Greitzer [37] to predict the occurrence of surge and is defined by equation (A.4), where U is the mean rotor velocity, S_C is the compressor flow-through area and L_C is the compressor equivalent duct length. In the present case, the values of U and S_C are taken at the impeller rotor inlet and L_C is taken as the length from the domain inlet to exit.

$$\mathrm{P_{out}}(t+\delta t) = P_{out}(t) + \frac{\rho_{out} U^2 \delta t}{4B^2 L_c}\left(\frac{\dot{m}_{out}(t)}{\rho_{out} S_C} - \sqrt{2\left(\frac{P_{out}(t) - P_{in,compressor}}{\rho_{in} K_t}\right)}\right) \tag{A.3}$$

$$B = \frac{U}{2a}\sqrt{\frac{V_P}{S_C L_C}} \tag{A.4}$$

When flow reversal occurs (negative mass flow), as is the case during part of a deep surge cycle, the boundary setup shown is as Figure A.2 b, with the atmospheric pressure applied at the inlet of the CFD domain, while the total pressure and total temperature described by equations (A.5) and (A.6) are applied at the CFD outlet domain.

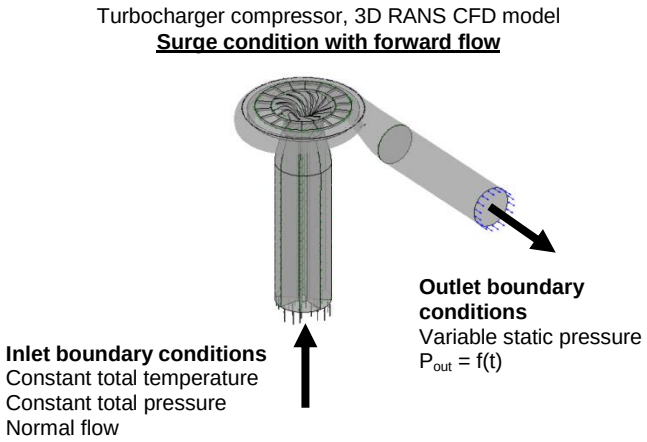

(a) Positive mass flow (forward mass flow)

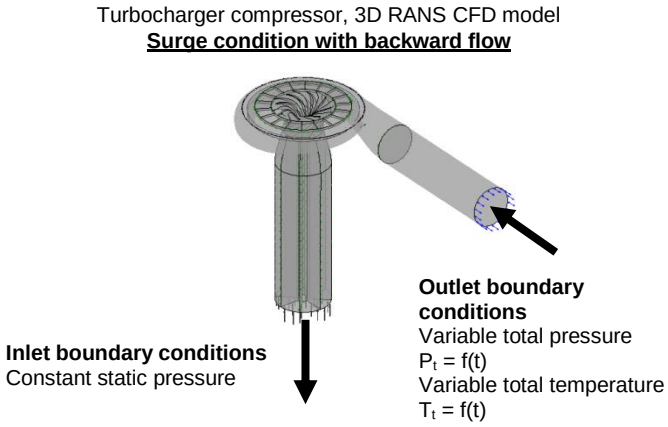

(b) Negative mass flow (flow reversal)

Figure A.2 CFD boundary conditions applied to the turbocharger compressor 3D model

$$\mathrm{P_t}(t+\delta t) = \mathrm{P_{out}}(t+\delta t)\left(\left(1+\frac{\gamma-1}{2}\,M(t)^2\right)^{\frac{\gamma}{\gamma-1}}\right) \quad \text{or} \quad \mathrm{P_{out}}(t+\delta t) \tag{A.5}$$

$$\mathrm{T_t}(t+\delta t) = T_t(t)\left(\frac{P_t(t+\delta t)}{P_t(t)}\right)^{\frac{\gamma-1}{\gamma}} \tag{A.6}$$

The switch in boundary condition setup is made possible in ANSYS CFX by using the *opening boundary condition* with the option of *opening pressure and direction*.

The details of the equation derivations and implementation of the throttle boundary conditions can be found in reference [37].

A.2 Choice of Throttle Constant

While a throttle constant is more representative of the physical setup, one of its disadvantages in the context of this project is to obtain the right value of the throttle constant K_t to get a desired mass flow. The method used in the present project is partly iterative. It consists for each housing of carrying simulations at several (at least four) values of K_t and curve fitting the resulting data to obtain a function linking K_t to mass flow, as shown in Figure A.3.

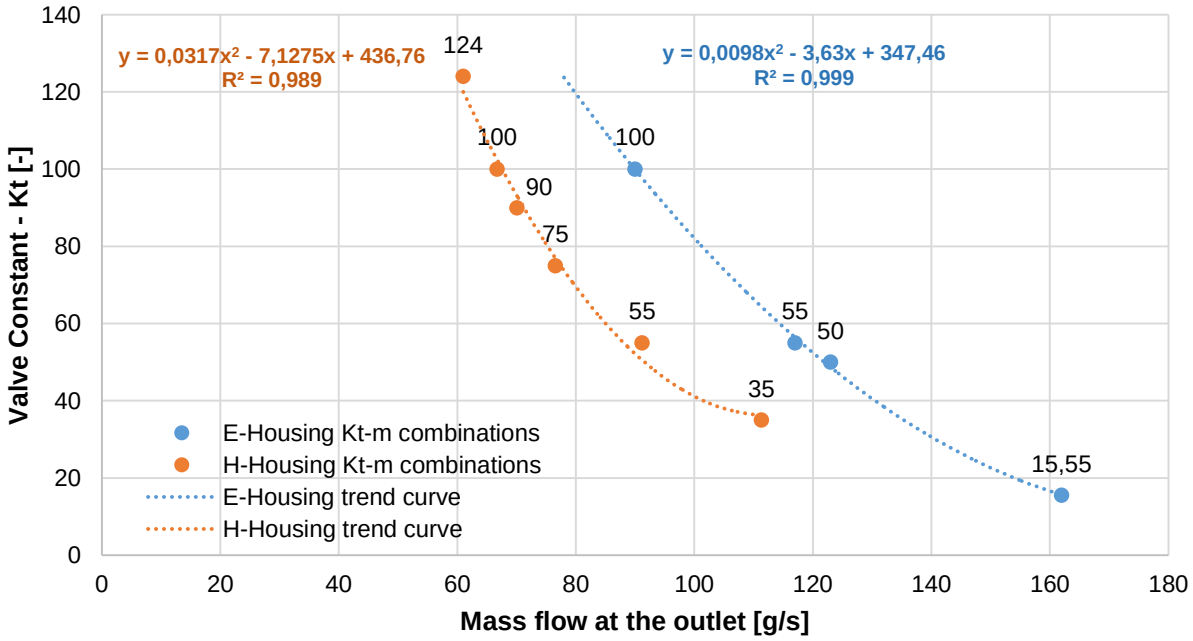

Figure A.3 Relation between the valve constant (Kt) and the resultant mass flow in E and H housings unsteady simulations

A.3 Efficiency Correction

While the process for selecting the value of the throttle constant described in section A.3 is effective, the resulting mass flow can still differ from the desired value by a few tenths of g/s, which explains the need for efficiency correction through the process illustrated in Figure A.4. It essentially consists of using the adiabatic efficiency versus mass flow slope between the nearest two data points obtained with full-wheel unsteady simulations with constant mass flow boundary condition to shift the efficiency value to the desired mass flow.

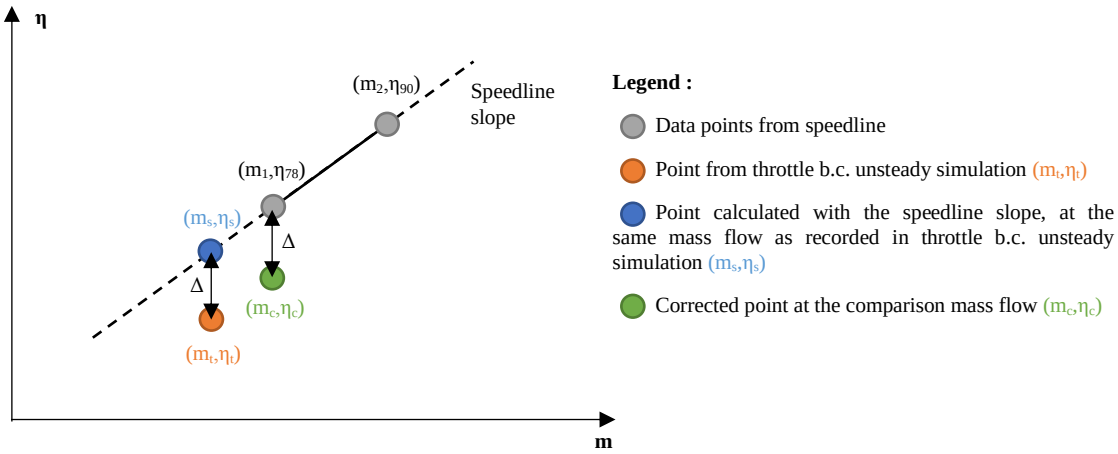

Figure A.4 Efficiency correction method

APPENDIX B ANSYS VERSION VERIFICATION

Due to a relatively recent hardware upgrade in the governmental computational cluster used for simulations in this project, the ANSYS CFX version 16.1 used for most of the simulations was no longer available and later simulations had to be run in part or in full with ANSYS CFX version 18.1 on the new cluster. This appendix presents a verification of equivalency between the two versions through comparisons of similar runs made in either version.

Figure B.1 compares the time history of the adiabatic efficiency for the unsteady simulations of the E-housing near surge with a throttle boundary condition and a short outlet duct (Model A in Figure 3.8 a) ran from the same initial guess on the old cluster with v16.1 (using 48 cores distributed four nodes) and on the new cluster with v18.1 (using 48 cores on a single node) 48. The results show that after the initial 30 rotor revolutions, the results start to differ even though the amplitude and oscillation amplitude is similar.

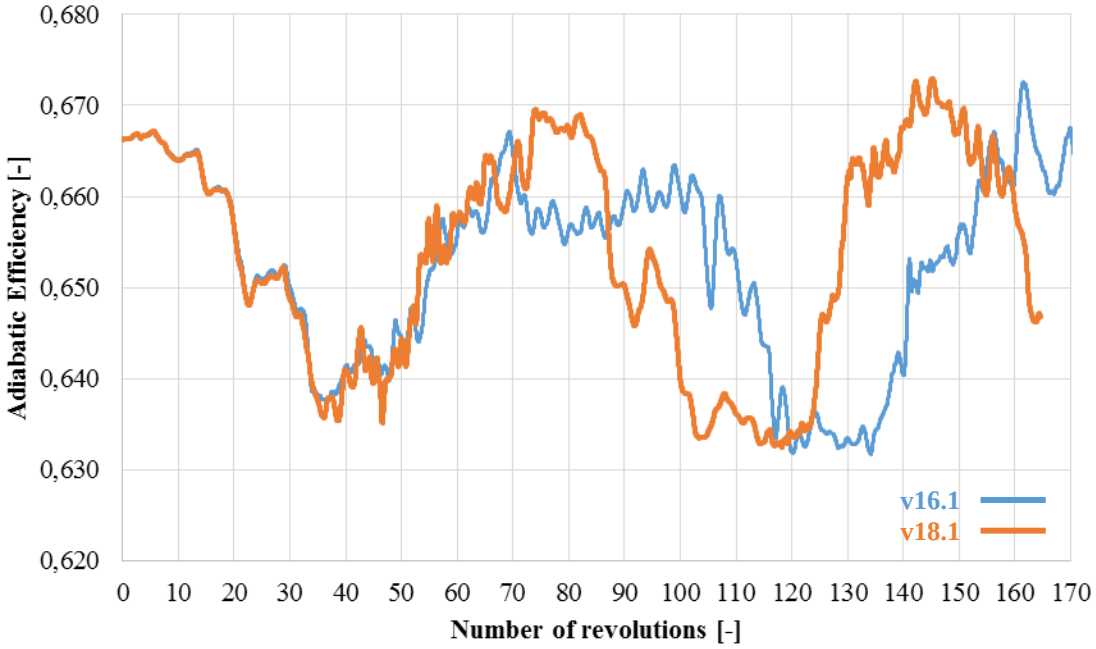

Figure B.1 Unsteady convergence time history of adiabatic efficiency for **E-housing at 78 g/s**, short duct model with **throttle b.c.** (u-E-FW-78-5-d-p) with different ANSYS CFX versions

To ensure that the difference is not purely related to version change, simulations of the E-housing at 90 g/s performed twice on the old cluster in v16.1 were retrieved and compared in Figure B.2. In this case, the ANSYS CFX version was the same but the core used (distributed over four nodes and assigned automatically by the cluster) were different for each simulations. The resulting Figure B.2 shows that the difference in hardware is enough to cause the two solutions to differ after a while as was seen in Figure B.1, while also exhibiting similar trends.

On the other hand, when the same comparison is made for two same simulations of the E-housing near surge were performed on exactly the same node in the new cluster both with v18.1, Figure B.3 shows that the results is exactly the same.

Based on the above, one can conclude the difference seen in Figure B.1 between the old and new cluster is likely due in large part to hardware change rather than version change.

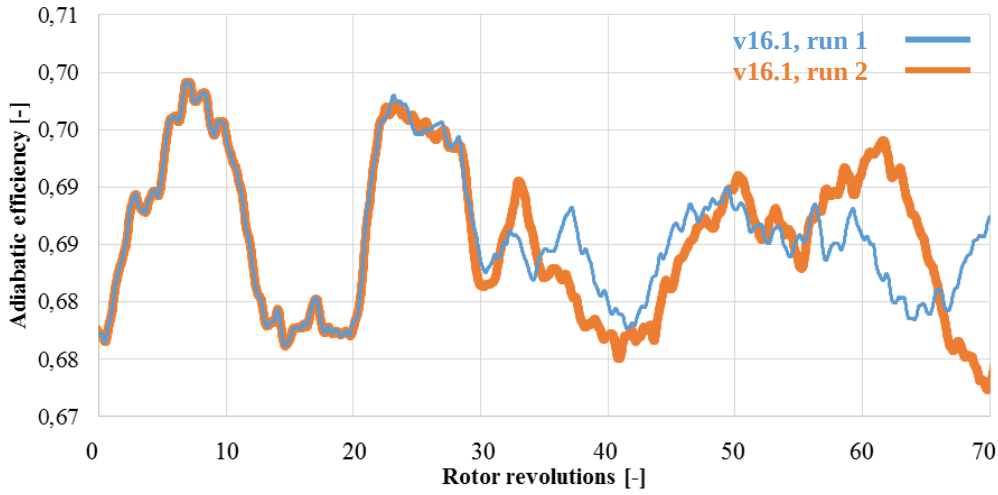

Figure B.2 Unsteady convergence time history of adiabatic efficiency for **E-housing at 90 g/s**, short duct model with **throttle b.c.** (u-E-FW-90-5-d-p) with v16.1 ANSYS CFX version

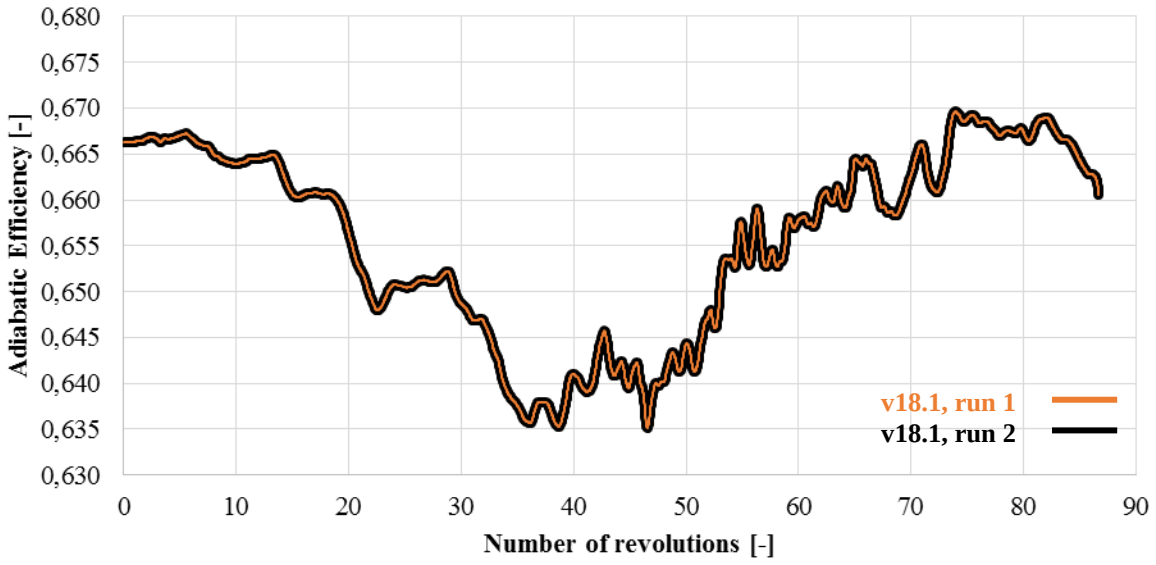

Figure B.3 Unsteady convergence time history of adiabatic efficiency for **E-housing at 78 g/s**, short duct model with **throttle b.c.** (u-E-FW-90-5-d-p) with v18.1 ANSYS CFX version

APPENDIX C H-HOUSING COMPUTATIONAL DOMAIN

This appendix shows the computational domains for the H-housing configuration along with the interfaces and boundary conditions used.

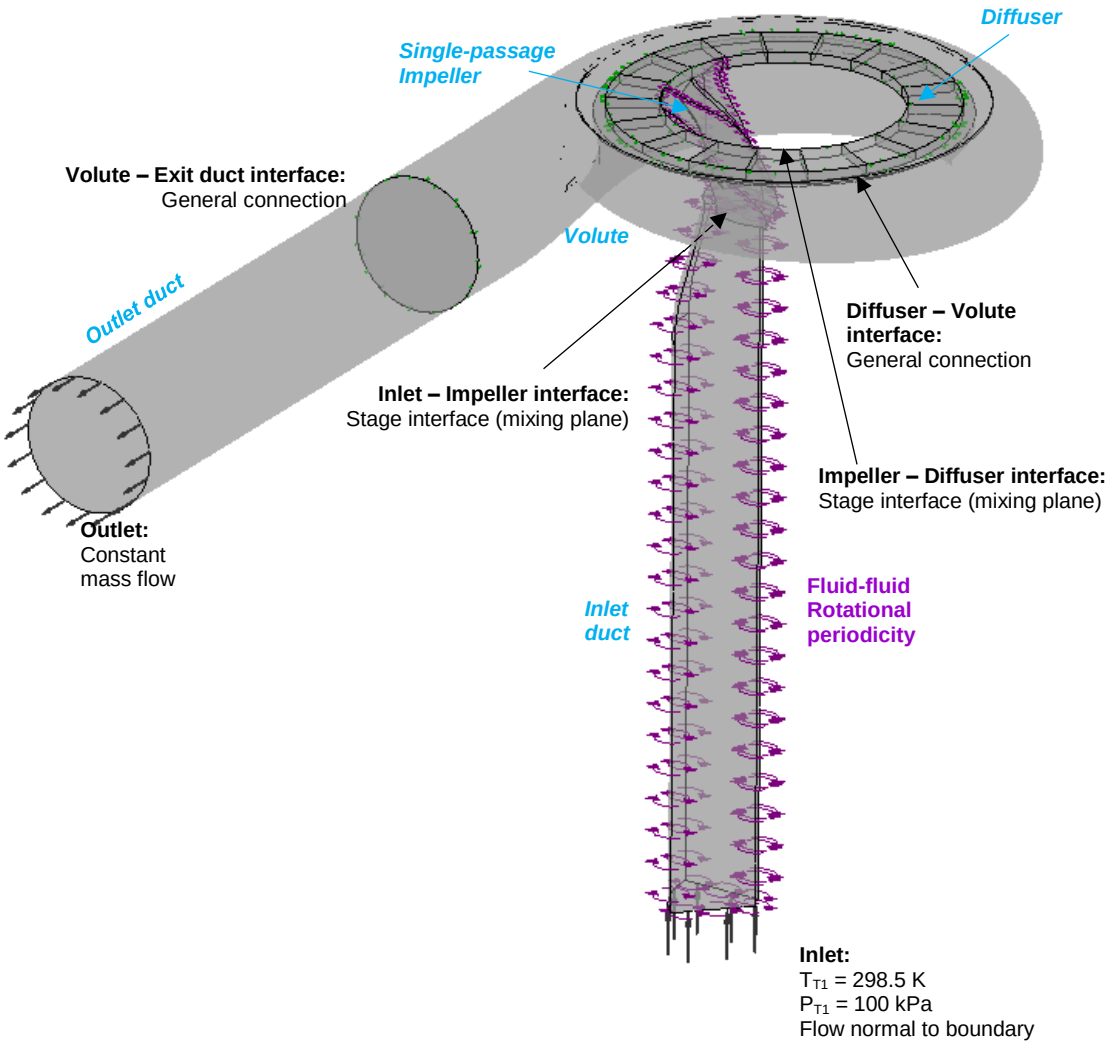

Figure C.1 Computational domain for single-blade passage model (H-housing)

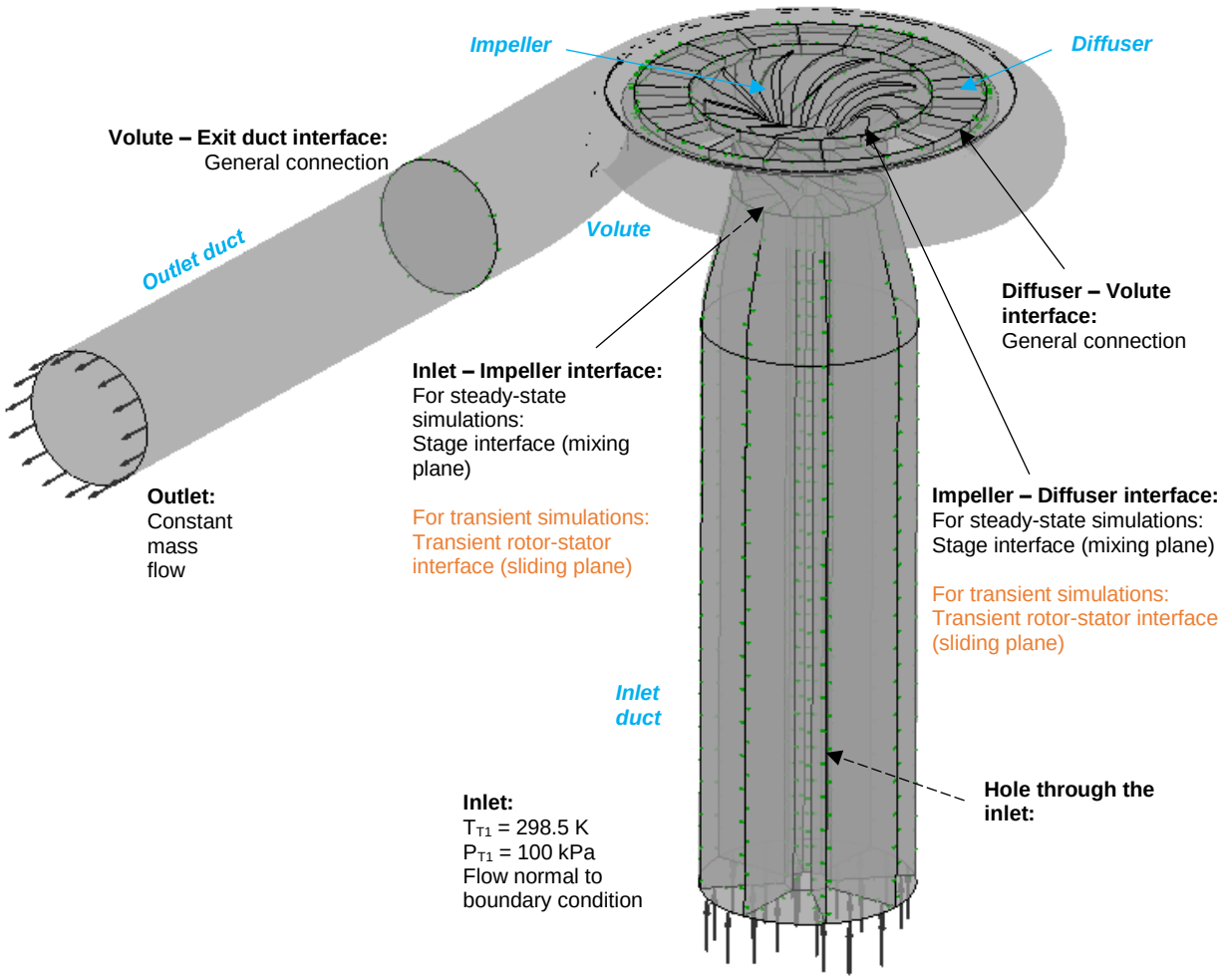

Figure C.2 Computational domain for full-wheel model (H-housing)

APPENDIX D STEADY-STATE SIMULATION VALIDATION

This appendix lists the results all steady-state (single passage and full-wheel) simulations performed for comparison with available test data (Section D.1). Section D.2 provides investigates the effect of the time-scale setting in steady-state simulations in ANSYS CFX.

D.1 Validation with Test Data

While section 4.1 focused on results from steady-state simulations of both housings with the short duct model at near surge and 90 g/s, steady-state simulations were also performed at two other mass flows, namely the design point and an intermediate mass flow (83 g/s), and also with the long duct configurations (similar to Figure 3.8 c) for comparison with measured speedline data. Table D.1 lists the mass flow values at which steady-state simulations were performed.

Table D.1 Steady-state runs done with each housing (Ω = 220 000 RPM)

E-Housing	**H-Housing**
Near surge: m = 78.09 g/s	Near surge: m = 72.42 g/s
m = 83 g/s	m = 83 g/s
m = 90 g/s	m = 90 g/s
Design point: m = 130.22 g/s	Design point: m = 128.42 g/s

Tables D.2 and D.3 list the measured values of pressure ratio and adiabatic efficiency and their CFD-predicted values for the E-housing and the H-housing, respectively, and the results are compared graphically in Figures D.1 and D.2. To make the comparison as fair as possible, the listed adiabatic efficiency from CFD simulations as with the alternative calculation method described in section 3.4.2 to emulate the method of deducing adiabatic efficiency from raw test data. All the listed steady-state simulations were run with a time scale setting of 5e-5 s, as suggested by Garrett Motion. These tables and figures indicate that the predicted pressure ratio and adiabatic efficiency do not vary much with duct length nor between single and full-wheel configurations. However, all of the steady-state simulations overestimate the adiabatic efficiency by 2-3 percentage points.

Table D.2 E-housing steady-state runs results (Ω = 220 000 RPM) – u-E-FW-78-20-d-p

		Experimental data		Full-wheel model				Single-blade passage model			
				Short outlet duct (s-E-FW-d)		Long outlet duct (s-E-FW-D)		Short outlet duct (s-E-SP-d)		Long outlet duct (s-E-SP-D)	
Ω (RPM)	**m (kg/s)**	**PR_{TT}**	**η_{TT} (%)**	**PR_{TT}**	**η_{TT} (%)**	**PR_{TT}**	**η_{TT} (%)**	**PR_{TT}**	**η_{TT} (%)**	**PR_{TT}**	**η_{TT} (%)**
220 000	0.0781	3.3986	65.50	3.482	66.80	3.467	66.53	3.469	66.75	3.464	66.40
220 000	0.0830	N/D	N/D	3.380	68.13	3.365	67.87	N/D	N/D	N/D	N/D
220 000	0.0900	N/D	67.40	3.298	69.21	3.288	69.03	3.292	69.04	3.283	68.85
220 000	0.0912	3.3346	67.60	N/D	N/D	N/D	N/D	N/D	N/D	N/D	N/D
220 000	0.1039	3.3141	70.14	N/D	N/D	N/D	N/D	N/D	N/D	N/D	N/D
220 000	0.1162	3.2920	72.45	N/D	N/D	N/D	N/D	N/D	N/D	N/D	N/D
220 000	0.1302	3.1259	73.38	3.272	77.34	N/D	N/D	3.288	76.93	N/D	N/D
220 000	0.1429	2.8097	70.99	N/D	N/D	N/D	N/D	N/D	N/D	N/D	N/D
220 000	0.1544	2.1658	57.30	N/D	N/D	N/D	N/D	N/D	N/D	N/D	N/D

Table D.3 H-housing steady-state runs results (Ω = 220 000 RPM)

		Experimental data		Full-wheel model				Single-blade passage model			
				Short outlet duct (s-H-FW-d)		Long outlet duct (s-H-FW-D)		Short outlet duct (s-H-SP-d)		Long outlet duct (s-H-SP-D)	
Ω (RPM)	**m (kg/s)**	**PR_{TT}**	**η_{TT} (%)**	**PR_{TT}**	**η_{TT} (%)**	**PR_{TT}**	**η_{TT} (%)**	**PR_{TT}**	**η_{TT} (%)**	**PR_{TT}**	**η_{TT} (%)**
220 000	0.0724	3.2863	62.02	3.463	64.40	3.413	64.16	3.416	64.13	3.411	64.04
220 000	0.0830	N/D	N/D	3.289	67.13	3.278	66.93	N/D	N/D	N/D	N/D
220 000	0.0861	3.2054	64.46	N/D	N/D	N/D	N/D	N/D	N/D	N/D	N/D
220 000	0.0900	N/D	65.40	3.367	69.23	3.211	68.43	3.219	68.51	3.207	68.26
220 000	0.1134	3.2491	71.07	N/D	N/D	N/D	N/D	N/D	N/D	N/D	N/D
220 000	0.1284	3.1076	72.90	3.273	77.13	N/D	N/D	3.242	77.50	N/D	N/D
220 000	0.1430	2.7970	70.95	N/D	N/D	N/D	N/D	N/D	N/D	N/D	N/D
220 000	0.1547	2.1361	58.17	N/D	N/D	N/D	N/D	N/D	N/D	N/D	N/D

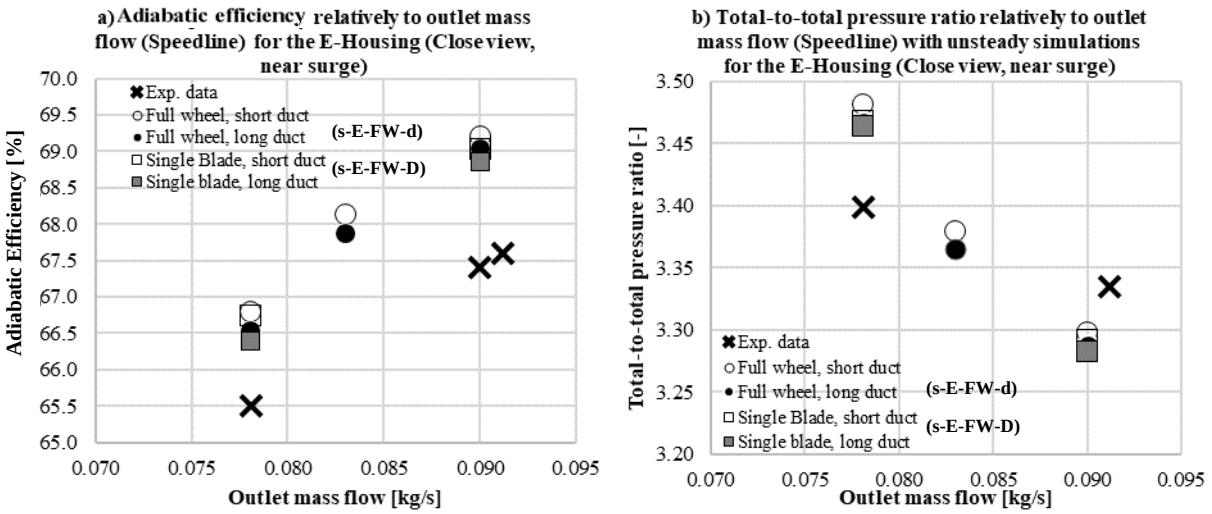

Figure D.1 Steady-state CFD speed lines for E-Housing

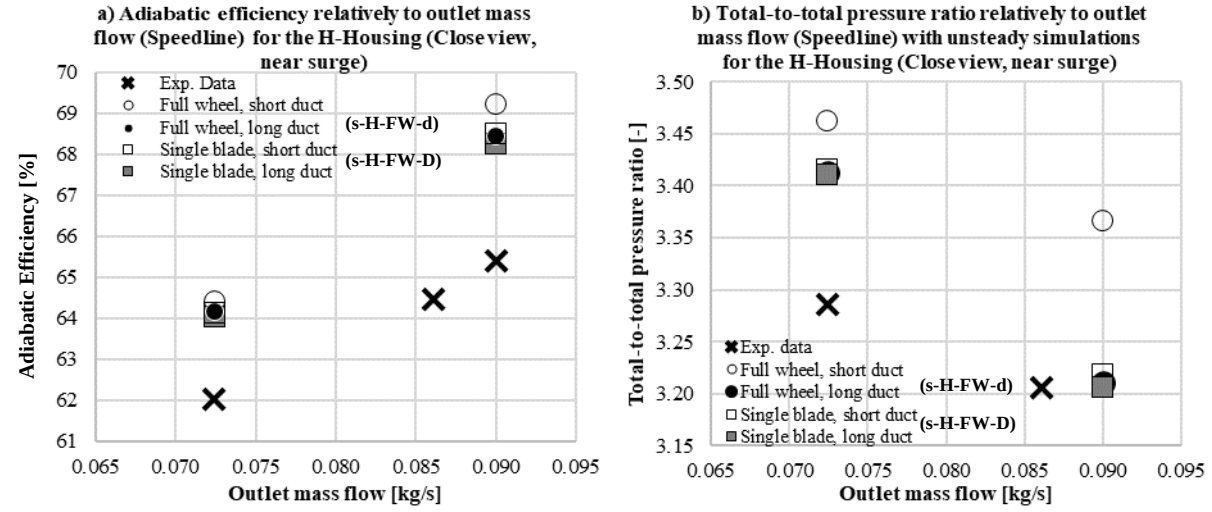

Figure D.2 Steady-state CFD speed lines for H-Housing

D.2 Effect of Time Scale

An important input parameter for steady-state simulations in ANSYS CFX is the time scale setting. According to the CFX help module, this setting acts as a mean for under-relaxation of the equations. An excessively large time scale setting can lead to oscillatory convergence behaviour. However, the failure to improve convergence with a lower time scale setting may indicate presence of flow separation and/or transonic flow in the computational domain.

A time scale study has been thus performed to assess the effect of this parameter on predicted adiabatic efficiency from steady-state simulations, and on the behaviour of the simulation to

validate the standard value proposed by Garrett Motion. Table D.4 lists the time scale values (also indicated in terms of number of time steps per blade passing) chosen for this study.

Table D.4 List of time scales used for the time scale study for both housings

Time scale [s]	Time scale, indicated in number of rotor revolutions (at 220 000 RPM)
5e-5	N = 0.7
3.409e-5	N = 1
6.818e-5	N = 2
3.409e-6	N = 10
5.114e-6	N = 15
6.818e-6	N = 20

Table D.5 Steady-state simulations results near surge for each housing, full-wheel model (s-FW-d), when using different time scales

	N=0.7	N=1	N=2	N=10	N=15	N=20
E-Housing (s-FW-78-d)	66.80%	66.80%	66.82%	66.80%	Did not converge in time	Did not converge in time
H-Housing (s-FW-72-d)	64.40%	64.26%	64.50%	64.30%	Did not converge in time	Did not converge in time

Among these time scales, two have been chosen for a more detailed comparison:

- 5e-5 s (N = 0.7), which is the time scale recommended by Garrett Motion;
- 3.409e-6 s (N = 10), which corresponds to one of the time step value used in some of the unsteady simulations.

The corresponding efficiency convergence curves and the average efficiency values for both housings at near surge and 90 g/s are shown in Figures D.3 and D.4 for the N=7 and N=10 times scales, respectively. The plotted curves are for simulations done on the standard (short) outlet duct configurations, with the “1/8” label in the legend indicating the single-passage model. These figures show that the lower the time scale setting by an order of magnitude time scales does not significantly alter the predicted average efficiency nor the convergence behaviour, thus validating the time scale value recommended by Garrett Motion. On the other hand, the fact that the oscillatory nature of the convergence is not educed by a much lower time scale setting is an

indication of unsteadiness in the computational domain, which has been verified with unsteady simulations.

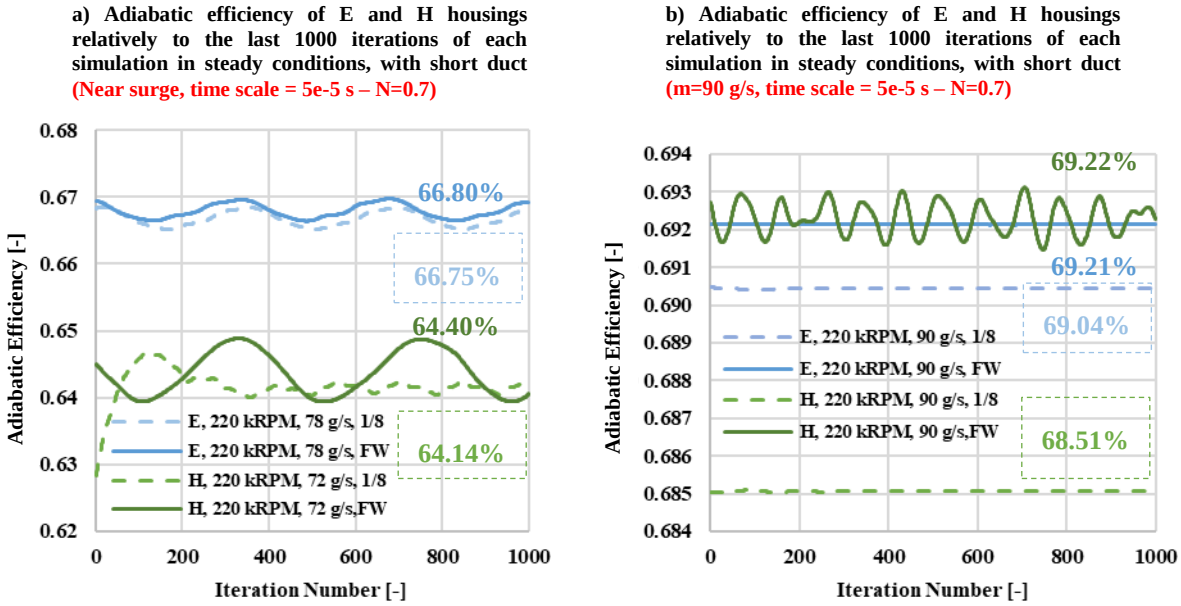

Figure D.3 Efficiency curves for both housings and both models with short ducts, using a 5e-5s time scale

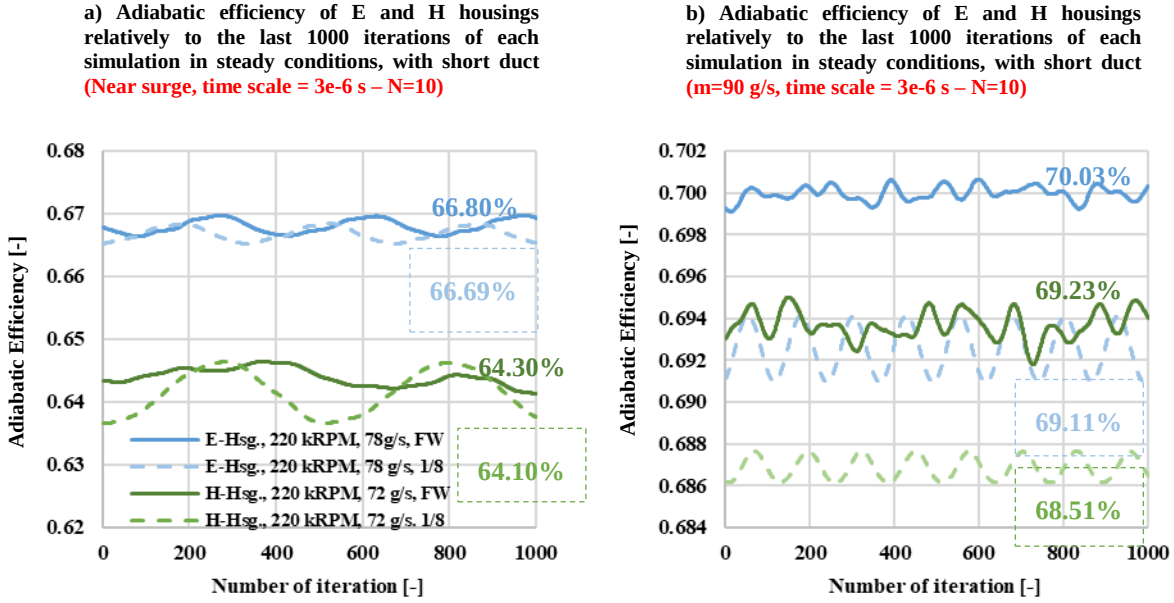

Figure D.4 Efficiency curves for both housings and both models with short ducts, using a 3e-6s time scale

Moreover, the efficiency convergence curves and the average efficiency have also been plotted for steady-state simulations with the long duct models at a time scale of 5e-5 s in Figure D.5 to study the effect of the duct length on convergence behaviour. A comparison between Figures D.3 (short duct and D.5 indicate that the additional exit duct length reduces oscillations in the convergence, perhaps by attenuating the flow unsteadiness in the domain.

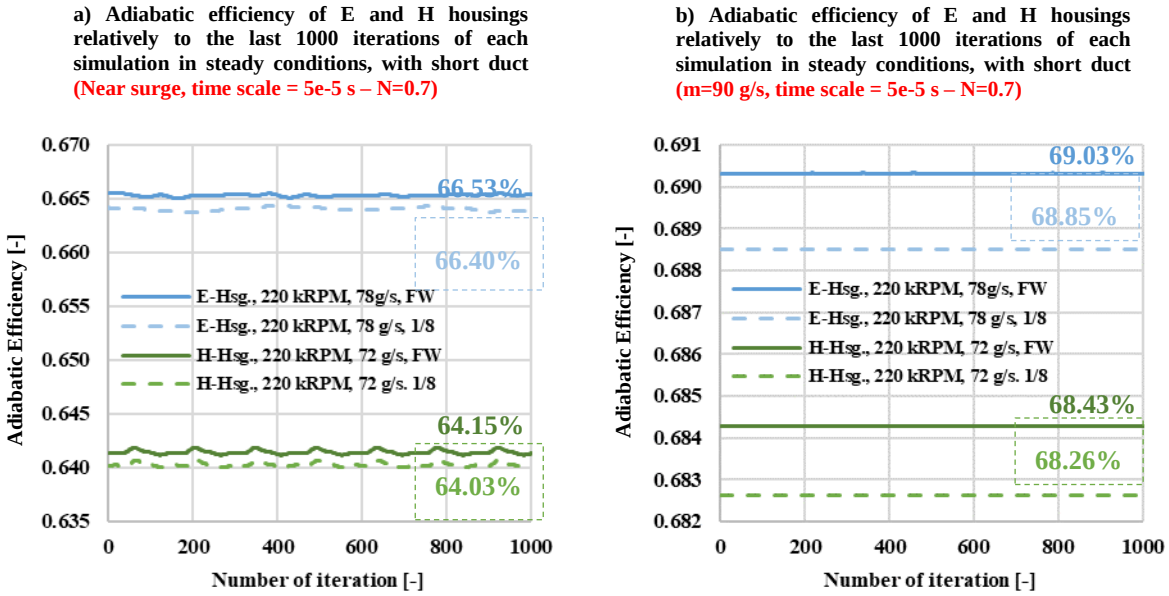

Figure D.5 Efficiency curves for both housings and both models with long ducts, using a 5e-5s time scale

When comparing the convergence of cases with the normal duct relatively to the ones with the longer outlet duct, it is possible to see that the additional length at the outlet attenuates the oscillations due to the unsteadiness in the domain and helps to reach convergence.

Table D.6 provides a review of the effect time scale, outlet duct length and single passage versus full wheel model selection on the convergence of a steady-state simulation in ANSYS CFX. This analysis is provided for the H-housing simulations at near surge (72 g/s) and 90 g/s.

Table D.6 Convergence analysis for the H-housing solver runs

	H-Housing, near surge (m=72 g/s)						H-Housing, (m=90 g/s)					
	Single Pass. Physical t.s.= 5e-5s	Full wheel Physical t.s.= 5e-5s	Single Pass. Physical t.s.= 3e-6s	Full wheel Physical t.s.= 3e-6s	Single Pass. Long duct Physical t.s.= 5e-5s	Full wheel Long duct Physical t.s.= 5e-5s	Single Pass. Physical t.s.= 5e-5s	Full wheel *Auto. t.s= 4.34e-6s*	Single Pass. Physical t.s.= 3e-6s	Full wheel Physical t.s.= 3e-6s	Single Pass. Long duct Physical t.s.= 5e-5s	Full wheel Long duct Physical t.s.= 5e-5s
RMS	Mass: 1.30e-6 Mom.: 1.21e-4	Mass: 2.0e-6 Mom.: 4.5e-4	Mass: 2.19e-6 Mom.: 7.15e-4	Mass: 2.63e-5 Mom.: 1.82e-3	Mass: 1.23e-6 Mom.: 7.40e-4	Mass: 6.49e-7 Mom.: 4.13e-4	Mass: 1e-7 Mom.: 2.4e-6	Mass: 3.60e-5 Mom.: 3.48e-3	Mass: 2.2e-5 Mom.: 3.9e-4	Mass: 7.6e-5 Mom.: 8.8e-3	Mass: 1e-7 Mom.: 1e-4	Mass: 3.24e-6 Mom.: 9.15e-5
MAX	Mass: 1.82e-4 Mom.: 7.46e-2	Mass: 2.0e-4 Mom.: 5.0e-2	Mass: 1.64e-4 Mom.: 4.67e-2	Mass: 3.19e-4 Mom.: 3.93e-2	Mass: 1.8e-4 Mom.: 4.6e-2	Mass: 1.79e-4 Mom.: 4.49e-2	Mass: 3e-5 Mom.: 1e-4	Mass: 4.60e-3 Mom.: 6.75e-2	Mass: 1.75e-3 Mom.: 2.13e-2	Mass: 6.4e-3 Mom.: 1.3e-1	Mass: 3.5e-5 Mom.: 3.6e-3	Mass: 3.28e-4 Mom.: 6.11e-3
η	**0.641 ± 0.001**	**0.644 ± 0.004**	**0.642 ± 0.004**	**0.644 ± 0.004**	**0.6404± .00035**	**0.641± 0.0003**	**0.6851 (flat)**	**0.6925± .0005**	**0.687 ± .0006**	**0.694± .00125**	**0.6826 (flat)**	**0.6843 (flat)**
Inlet imbalance	Energy & mass 0.02%	**Mass 3%**	Mass 0.03%	**V mom. 17%**	Energy & mass 0.03%	Mass 0.0125%	Energy & mass 0.0015%	**U & V mom. 7%**	Mass 0.3%	**U & V mom. 16% & 7.5%**	Mass 0.0001%	Mass 0.0125%
Wheel imbalance	Mass 0.004%	Energy & mass 0.3%	Mass 0.04%	Energy & mass 0.5%	Mass 0.006%	Mass 0.007%	V mom. 0.0002%	Mass 1%	Mass 0.4%	**Mass 2%**	Energy 0.0002%	Mass 0.0065%
Diffuser imbalance	Energy & mass 0.05%	Energy, mass 0.4%	Energy & mass 0.4%	Energy & mass 0.45%	Energy & mass 0.08%	Energy & mass 0.005%	Energy & mass 0.0003%	Energy & mass 0.4%	**En. & mass 2%**	Energy & mass 0.7%	Energy & mass 0.0002%	Energy & mass 0.005%
Volute imbalance	Energy & mass 0.7%	**En. & mass 5.5%**	**En. & mass 6%**	**En. & mass 2%**	Energy & mass 1.2%	Energy & mass 0.025%	Energy & mass 0.0015%	Energy & mass 1%	**En. & mass 3.5%**	**En. & mass 2%**	Energy & mass 0.0025%	Mass 0.02%
Outlet imbalance	Energy & mass 0.5%	**En. & mass 6%**	**En. & mass 6%**	**En. & mass 2.5%**	Energy & mass 0.9%	Energy & mass 0.025%	Energy & mass 0.0015%	Energy & mass 0.3%	Energy & mass 0.5%	Energy & mass 1%	Energy & mass 0.002%	Energy & mass 0.025%

a) MAX residuals are two magnitudes higher vs RMS residuals: Sign of local phenomenon causing convergence issues.

b) In all cases, the single passage model has less imbalance issues than the full wheel models.

c) The long duct model helps the residuals and imbalance values to remain low.

d) In all cases, when using the same model type, smaller time scales:
- **Cause more imbalance**
- **Increase residuals (MAX and RMS)**

e) Efficiency values remain in the same range no matter the chosen method

The following observations can be made from Table D.6:

a) The residual level is an indication of possible unstable flow presence in the domain. According to the ANSYS CFX help[3], if MAX residuals are 100 times bigger, or more, than the RMS residual, it shows that there is a punctual location in the housing where unsteadiness occurs.

b) The imbalance level from all subdomains is higher in full-wheel simulations than it is for single-blade passage runs. Imbalance levels over 1% are indicated in red in Table D.6 occurring mostly when the full-wheel model is used.

c) The model with the longer outlet duct results in lower subdomain imbalance. Near surge, for the same time scale (5e-5s), the difference in imbalance level is very high, especially when using the full-wheel model. Extending the outlet duct in steady-state improves convergence.

d) A smaller time scale increases imbalance levels and both MAX and RMS residuals. The higher oscillations, especially in the m = 90 g/s case, shown in Figure D.4 confirms the trend found.

e) The adiabatic efficiency is relatively insensitive to time scale in this case.

[3] Section 15.10.1.1.2 – MAX residual level. ANSYS CFX help, release 16.2.

APPENDIX E SIMULATIONS RUNNING TIMES

This appendix lists the simulation time in steady-state and unsteady mode for the E-housing. Simulation times for the H-housing are similar to those of the E-housing.

Table E.1 Required time for steady-state simulations

Steady-state simulations			
Run	**Number of iterations to reach convergence**	**Required time**	**CPU properties**
s-E-SP-78-d	2,000	5 hours	4 x 12 partitions Intel Xeon X5650 Westmere 2.67 GHz
s-E-SP-78-D	3,500	8 hours	
s-E-FW-78-d	2,000	8.5 hours	
s-E-FW-78-D	5,000	24 hours	

Table E.2 Required time for unsteady simulations

Unsteady simulations				
Run		**Number of time steps to reach convergence (3 oscillations periods)**	**Required time**	**CPU properties**
u-E-FW-5	Cst. m	6,312	200 hours (8.3 days)	1 x 40 part. Intel Gold 6148 Skylake 2.4 GHz
	Throttle short duct	9,720	284 hours (11.8 days)	4 x 12 part. Intel Xeon X5650 Westmere 2.67 GHz
	Throttle long duct	5,502 Not converged yet (Figure F.2)	334 hours (13.9 days)	1 x 48 part. Intel Platinum 8160F Skylake 2.1 GHz
u-E-FW-10	Cst. m	15,544	413 hours (17.2 days)	1 x 48 part. Intel Platinum 8160F Skylake 2.1 GHz
	Throttle short duct	16,938	486 hours (20.2 days)	4 x 12 part. Intel Xeon X5650 Westmere 2.67 GHz
u-E-FW-20	Cst. m	15,641 For 1.5 oscillation periods only	413 hours (17.2 days) For 1.5 periods only	1 x 48 part. Intel Platinum 8160F Skylake 2.1 GHz
	Throttle short duct	33,468	1 019 hours (42.4 days)	4 x 12 part. Intel Xeon X5650 Westmere 2.67 GHz
u-E-FW-45-d-p		25,753 For one oscillation period only	737 hours (30.7 days) For one oscillation period only	4 x 12 part. Intel Xeon X5650 Westmere 2.67 GHz

APPENDIX F COMPARISON BETWEEN SIMULATIONS WITH N=20 AND N=45

This appendix compares in more detail the unsteady simulations results for the E-housing at the two lower time step settings (N=20 and N=45) to assess whether they provide similar results, to confirm the selction of N=20 as adequate.

Figure F.1 plots the time variations of adiabatic efficiency for both N=20 and N=45 compares directly the results from E-housing simulations when using N= 20 and 45. The points on the curve indicate the start and end points of the time-averaging periods with the corresponding time-averaged adiabatic efficiency values indicated in the top-right legend. First, one can see that the change in time-averaged adiabatic efficiency is very small between N=20 and N=45 (especially relative to N=10 as shown in Figure 4.5). Second, the oscillation amplitude and perhaps even period are similar.

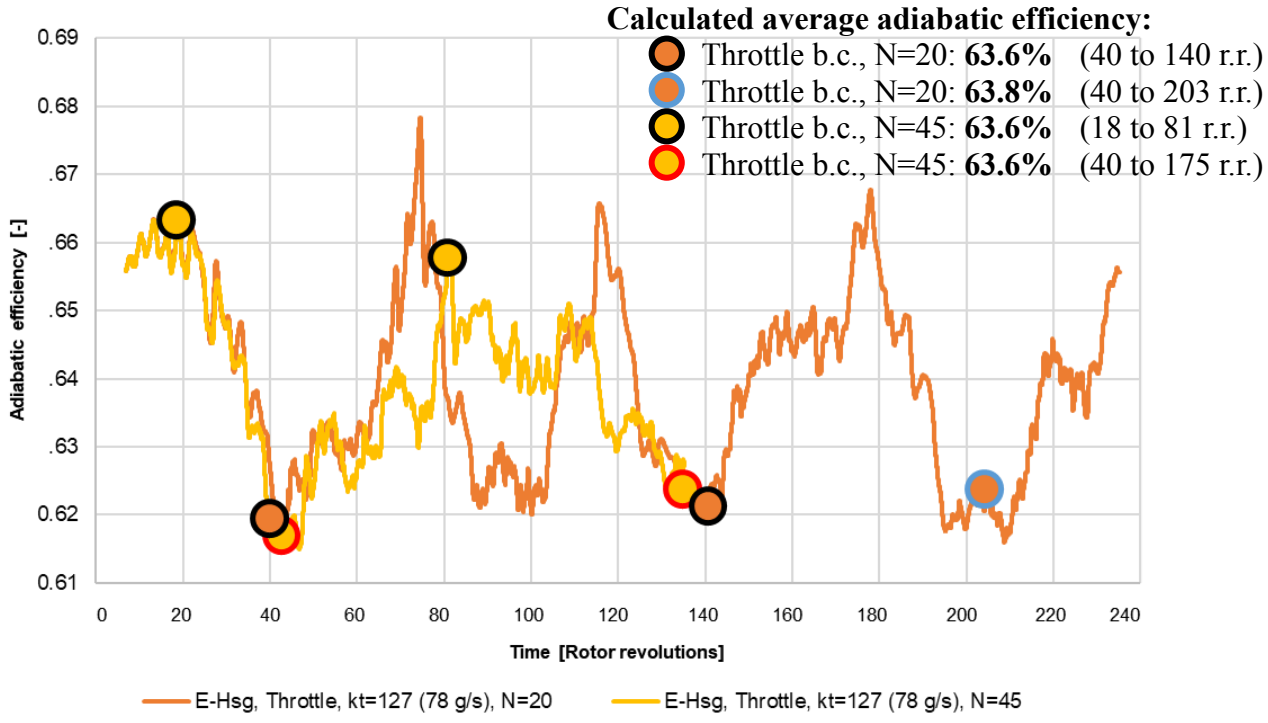

Figure F.1 Comparison between N=20 and N=45 simulations for the E-housing, Ω = 220 kRPM, near surge (throttle, m = 78.09 g/s), short duct model with small plenum – model A (u-E-FW-78-d-P)

Figure F.2 shows the instantaneous flow structures in the diffuser and volute for N=45 in a form similar to the plots of Figures 5.5 and 5.8 for N=20. A comparison shows that the solution at N=45 exhibits similar rotating stall flow structures (Figure F.2 a) and intermittent blockage in the outlet duct just downstream of the tongue as the N=20 solution.

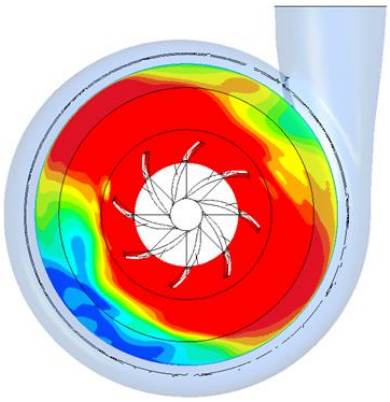

a) Mach number and velocity distribution at diffuser mid-span at one time instant

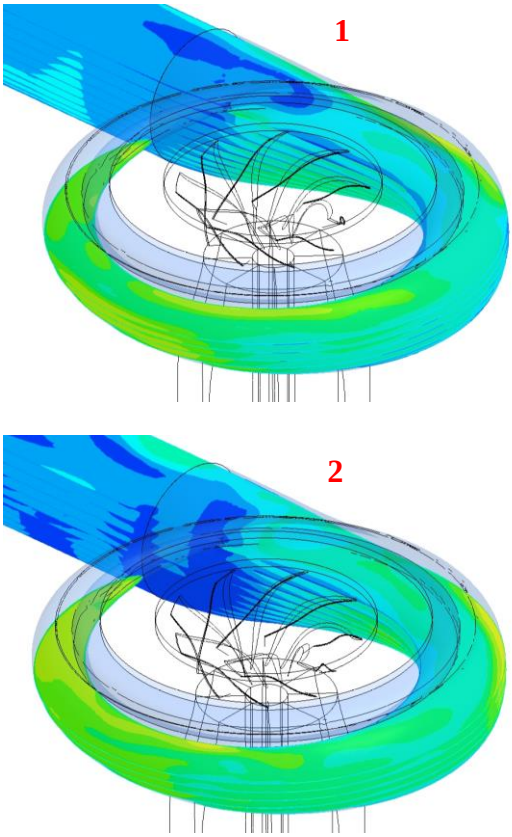

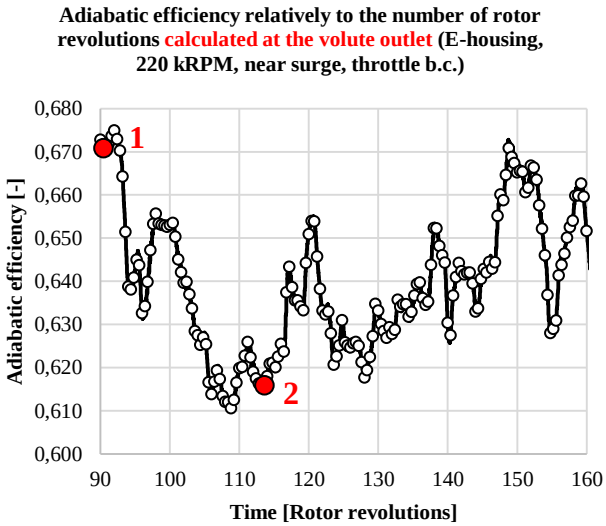

b) Mach number distribution in the volute and outlet duct at different time instants

Figure F.2 Instantaneous flow structures in E-housing near surge at N=45

APPENDIX G OTHER UNSTEADY SIMULATIONS

This appendix assesses the effect of outlet duct length and plenum size on the unsteady simulations with throttle boundary conditions of the E-housing near surge.

Figure G.1 plots the convergence history of adiabatic efficiency and outlet mass flow for models A, B and C as illustrated in Figure 3.8. As a recap, Model A (Figure 3.8 a) is the standard configuration with a short outlet duct and a modeled negligible plenum volume and throttle valve. Model B (Figure 3.8 b) has a short outlet duct with the volume of the remaining physical duct up to the physical throttle valve modelled as a plenum volume (i.e. the outlet duct air volume is modelled as a stagnant compressible volume) followed by a modelled valve. Model C (Figure 3.8 c) incorporates the entire outlet duct up to the physical throttle valve into the computational domain, leaving the throttle boundary condition to model negligible plenum volume and throttle valve. Configuration C can be considered the closest model to the actual test rig shown in Figure 3.2.

The results in Figure G.1 indicate that the amplitude and time period of the main efficiency oscillation increase in the presence a longer outlet duct either analytically modeled (model B) or simulated (model C). Moreover, while the use of a plenum model for the outlet duct (model B) seems to capture a similar amplitude of the main efficiency oscillation as that of the configuration that incorporated the outlet duct (model C), it differs in frequency and significantly overestimates the amplitude of the mass flow oscillations.

Last but not least, Figure G.2 plots the convergence history of adiabatic efficiency and outlet mass flow for model D (as illustrated in Figure 3.8 d) for which the entire duct length upstream and downstream of the physical throttle valve (see Figure 3.2) is modeled as a plenum volume in the throttle boundary condition. The simulation results show that this configuration goes into deep surge with flow reversal (negative mass flow), which is consistent with Greitzer [37] who has shown that a large plenum leads to surge. (While not shown, simulations of this configuration at a higher mass flow - 83 g/s – shows a stable oscillatory solution). This premature surge (since test data did not show surge at this mass flow) indicates that the throttle boundary condition can be used to simulate surge in the turbocharger compressor and also confirms the intuition that only the volume upstream of the valve should be modeled as the plenum.

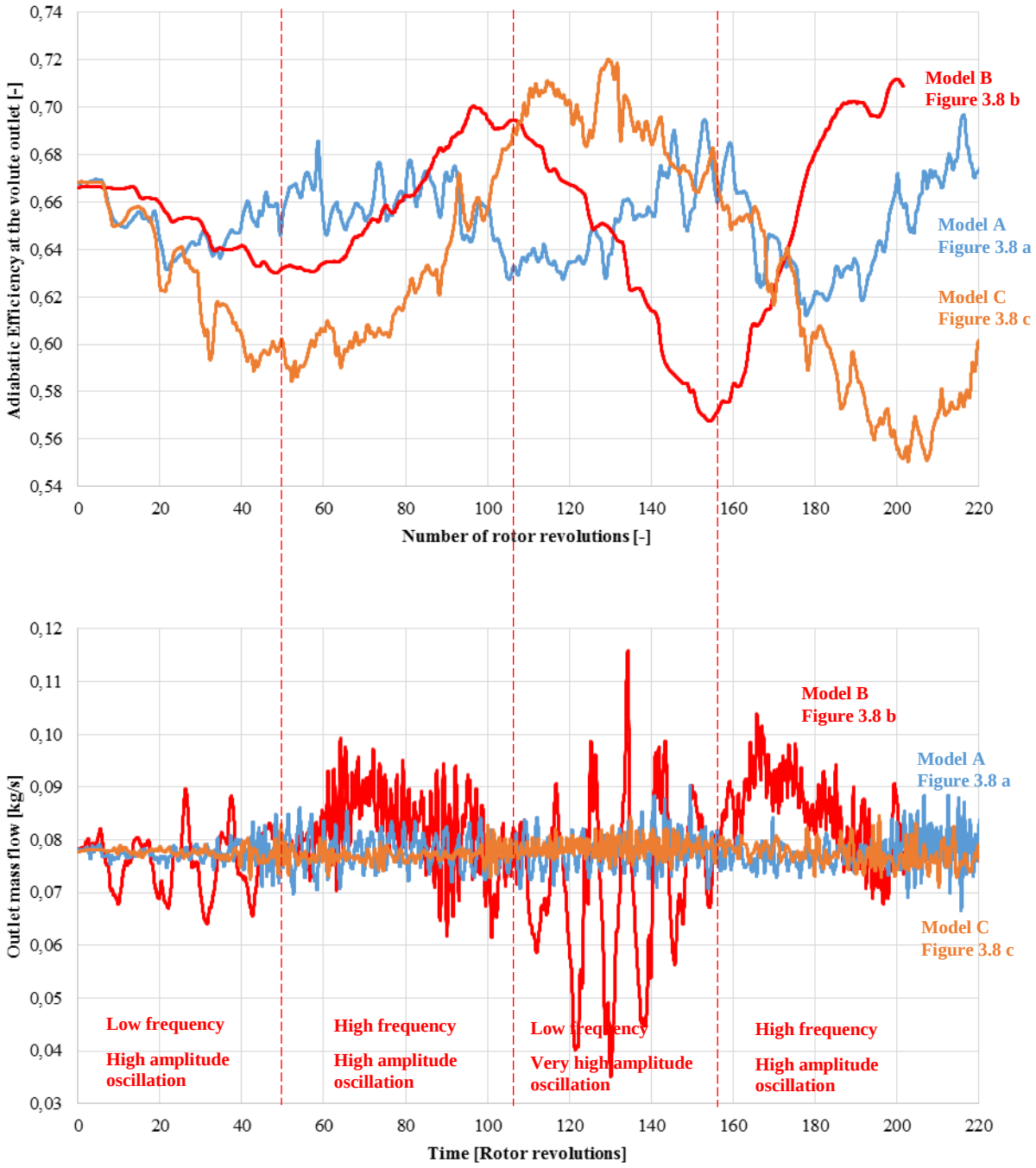

Figure G.1 Adiabatic efficiency at the volute outlet and mass flow at the computational domain exit for unsteady E-housing simulations at near surge (78.09 g/s) with throttle boundary conditions with different outlet duct and plenum volumes (model A: u-E-FW-78-5-d-p, model B: u-E-FW-78-5-d-P, and model C: u-E-FW-78-5-D-p)

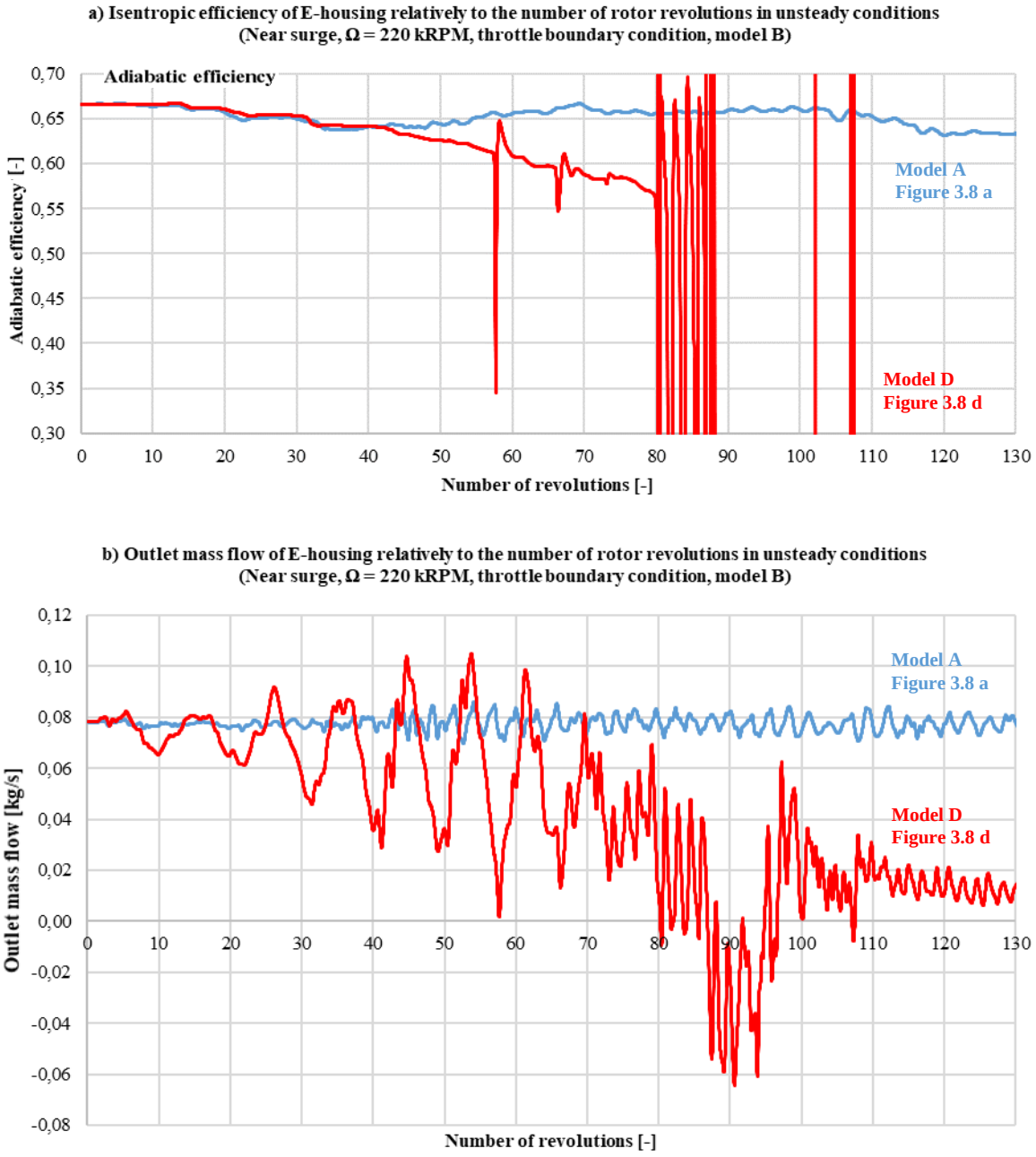

Figure G.2 Adiabatic efficiency at the volute outlet and mass flow at the computational domain exit for unsteady E-housing simulations at near surge (78.09 g/s) with throttle boundary conditions negligible (model A: u-E-FW-78-5-d-p) versus excessively large(model D: u-E-FW-78-5-D-P) plenum volume

APPENDIX H EFFECT OF FLOW UNSTEADINESS ON EFFICIENCY

This appendix presents a preliminary estimation of the penalty is adiabatic efficiency associated with the unsteadiness in the volute scroll triggered by rotating stall in the diffuser. From another point of view, the estimated value would be the efficiency gain if the unsteadiness in the volute scroll could be suppressed.

As illustrated in Figure H.1, the procedure essentially consists of calculating the total pressure loss across the volute (from the mass-average total pressure at the diffuser exit and CFD domain exit) for steady simulation and using this value to replace the total pressure loss across the volute in the unsteady simulation to obtain a revised domain exit outlet total pressure, with which the adiabatic efficiency is recalculated. The difference between the revised adiabatic efficiency value and the original value from the unsteady simulations is the efficiency penalty from volute flow unsteadiness.

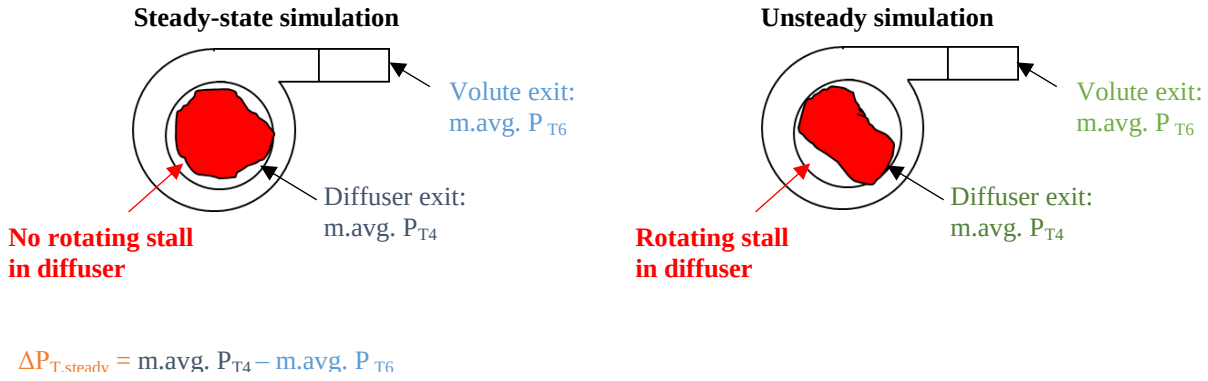

Figure H.1 Estimation of unsteady exit total pressure without volute oscillation

The procedure described above was applied to the unsteady simulations of E and H housings near surge with throttle boundary conditions and N=2 which were analyzed in chapter 5. The results are listed in Table H.1, which shows that the adiabatic efficiency increases by 1.83% an 1.13% for the E and H housings, respectively, when the exit total pressure is revised with the steady-state volute pressure loss. Given that the flow unsteadiness is relatively small for the H-housing near surge such that the difference is original and revised efficiency should be close to zero, the 1.13% value should represent the error offset associated with the proposed method. Applying this offset to the E-housing results in an efficiency penalty due to unsteadiness of 0.7% (or 0.7 percentage point).

Table H.1 Estimation of effects of volute flow oscillations on adiabatic efficiency

	E, m=78 g/s	**H, m=72 g/s**
$\eta_{unsteady}$	63.83%	62.07%
$\eta_{unsteady}$ **With Δ PT, steady**	65.66%	63.20%
η osc. amp.	± 4%	± 0.5%
Δη	**1.83%**	**1.13%**